HZG REPORT 2013-2 // ISSN 2191-7833

Macroscopic modeling of distortional hardening in polycrystals: application to magnesium alloys

(Vom Promotionsausschuss der Technischen Universität Dortmund im Jahr 2012 als Dissertation angenommene Arbeit)

B. Shi

wissen
schafft
nutzen

Helmholtz-Zentrum
Geesthacht
Zentrum für Material- und Küstenforschung

HZG REPORT 2013-2

Macroscopic modeling of distortional hardening in polycrystals: application to magnesium alloys

(Vom Promotionsausschuss der Technischen Universität Dortmund im Jahr 2012 als Dissertation angenommene Arbeit)

B. Shi

Helmholtz-Zentrum Geesthacht
Zentrum für Material- und Küstenforschung GmbH | Geesthacht | 2013

Die HZG Reporte werden kostenlos abgegeben.
HZG Reports are available free of charge.

Anforderungen/Requests:

Helmholtz-Zentrum Geesthacht
Zentrum für Material- und Küstenforschung GmbH
Bibliothek/Library
Max-Planck-Straße 1
21502 Geesthacht
Germany
Tel.: +49 4152 87-1690
Fax.: +49 4152 87-1717
E-Mail: bibliothek@hzg.de

Druck: HZG-Hausdruckerei

Als Manuskript vervielfältigt.
Für diesen Bericht behalten wir uns alle Rechte vor.

ISSN 2191-7833

Helmholtz-Zentrum Geesthacht
Zentrum für Material- und Küstenforschung GmbH
Max-Planck-Straße 1
21502 Geesthacht

www.hzg.de

HZG REPORT 2013-2

Macroscopic modeling of distortional hardening in polycrystals: application to magnesium alloys

(Vom Promotionsausschuss der Technischen Universität Dortmund im Jahr 2012 als Dissertation angenommene Arbeit)

Baodong Shi

98 pages with 31 figures and 6 tables

Abstract

Texture evolution in metals due to rotation of the atomic lattice results in a complex macroscopic mechanical behaviour which cannot in general be reasonably captured by only classical isotropic or kinematic hardening. Focusing on standard rate-independent plasticity, the evolution of microstructure leads to an evolving macroscopic anisotropy of the yield surface, also known as distortional or differential hardening. This effect is very important, particularly if non-radial loading paths such as those associated with forming processes are to be numerically analyzed.

In the present work, different existing distortional hardening models are critically reviewed. They are reformulated into the modern framework of hyperelastoplasticity and the same objective time derivative is applied to all evolution equations for a better comparison. Furthermore, since the original models are based on a yield function not accounting for the different mechanical responses between tension and compression as observed in metals showing a close-packed atomic structure, respective generalizations are also discussed. It is shown that only one of the extended models can fulfill the second law of thermodynamics. That model predicts a high curvature of the yield surface in the loading direction, while the opposite region of the yield surface is rather flat. Such a response can indeed be observed for some materials. In the case of magnesium alloys, however, that does not seem to be true. Therefore, a new constitutive model is presented. Its underlying structure is surprisingly simple and the model is not only thermodynamically consistent but also variationally consistent. Conceptually, distortional hardening is described by an Armstrong-Frederick-type evolution equation. The calibrated new model is implemented in a finite element framework and its predictive capabilities are demonstrated.

Makroskopische Modellierung der formativen Verfestigung in Polykristallen: Anwendung auf Magnesiumlegierungen

Zusammenfassung

Texturentwicklung in Metallen aufgrund der Rotation des atomaren Gitters führt zu einem komplexem mechanischen Verhalten, welches nicht hinreichend durch klassische Plastizitätsmodelle mit isotroper und/oder kinematischer Verfestigung beschrieben werden kann. Im Rahmen der ratenunabhängigen Plastizität führt die Entwicklung der Mikrostruktur zu einer Anisotropie der Fließfläche, auch bekannt unter dem Namen distortional hardening (Formänderungsverfestigung). Die Berücksichtigung dieses Effekts ist insbesondere bei nicht-radialen Lastpfaden bedeutend, welche z.B. bei Umformprozessen auftreten.

In der vorliegenden Arbeit werden zunächst verschiedene existierende Plastizitätsmodelle mit Formänderungsverfestigung untersucht. Diese Modelle werden in einen einheitlichen hyperelastisch-plastischen Rahmen überführt. Zum Beispiel wird für eine bessere Vergleichbarkeit die selbe Zeitableitung für alle Evolutionsgleichungen verwendet. Da die bereits existierenden Modelle keine Zug-Druck-Asymmetrie berücksichtigen, welche aber in Magnesium-Legierungen zu beobachten ist, werden auch Erweiterungen der zugrunde liegenden Fließfunktionen diskutiert. Es wird gezeigt, dass nur eines der erweiterten Modelle den Zweiten Hauptsatz der Thermodynamik erfüllt. Charakteristisches Merkmal dieses Modells ist eine starke Krümmung der Fließfläche in Belastungsrichtung. Solches Verhalten kann bei verschiedenen Materialien beobachtet werden; allerdings trifft dies nicht für Magnesium zu. Aus diesem Grund wird ein neues Materialmodell vorgestellt. Die resultierende physikalische Beschreibung ist nicht nur thermodynamisch sondern auch variationell konsistent. Die Formänderungsverfestigung wird auf der Grundlage einer Entwicklungsgleichung vom Armstrong-Frederick-Typ berücksichtigt. Das Materialmodell wird im Rahmen der Finite-Elemente-Methode implementiert, und die Materialparameter werden an Experimente mit einer Magnesium-Legierung angepasst.

Manuscript received / Manuskripteingang in Druckerei: 21. Februar 2013

Acknowledgements

The current thesis is a report of the research work carried out at Helmholtz Zentrum Geesthacht from March 2009 until May 2012. This could not have been accomplished without the smart supervision, constant support, encouragement and help of my supervisor, Professor Jörn Mosler. I would like to express my heartfelt gratitude to him.

I am deeply indebted to Dr. Dirk Steglich, who introduced me to the topic of the research work. I am grateful for his trust, support and all the fruitful discussions.

I would like to express my sincere gratitude to Dr. Ingo Scheider, Dr. Mintesnot Nebebe Mekonen and Dr. Yongjun Chen for their brilliant minds and great help.

I would like to thank all members of the department and appreciate their help, specially Dr. Olaf Kintzel, Dr. Shehzad Saleem Khan, Dr. Malek Homayonifar, Dr. Tao Xiao, M.Sc. Xiaowei Tian and Dr. Jonathan Paul. I would like to acknowledge Professor Norbert Huber for the opportunity I was given to be part of the research work.

I am also grateful to Mr. Peter Kummerow and all my friends in Geesthacht. It could not have been a colorful and impressive life without their help.

I would also like to express my gratitude to the Helmholtz Association and the China Scholarship Council for their funding of my study in Germany. I also thank my domestic supervisors Professor Fusheng Pan and Professor Aitao Tang for their support. I am grateful to my friends, Mr. Baohua Qian and Mr. Quan Shi, who made the guarantee for my study abroad.

Last but not least, I wish to thank my parents, Mr. Ming Shi and Mrs. Guomin Shang. They gave birth to me, guided me to understand the principle of life and the attitude for work. Without their unconditional support, love and encouragement, this work could not have been accomplished.

谨以此文，献给我的父母，石明先生和尚国民女士。

Contents

1. Introduction 1

2. Mechanical behaviour of magnesium alloys 5
- 2.1. Initial plastic anisotropy and strength differential effect 5
- 2.2. Evolving anisotropy: distortional hardening 5
- 2.3. Loading path dependent distortional hardening 7

3. Finite strain plasticity theory in a nutshell 9
- 3.1. Fundamentals 9
- 3.2. A prototype model for magnesium 12

4. Models suitable for the analysis of magnesium alloys 15
- 4.1. The Teodosiu model and its extensions 15
  - 4.1.1. Fundamentals 15
  - 4.1.2. Extensions of the Teodosiu model for magnesium alloys 18
  - 4.1.3. Thermodynamical consistency 19
- 4.2. The Levkovitch & Svendsen model and its extensions 21
  - 4.2.1. Fundamentals 21
  - 4.2.2. Extensions of the Levkovitch & Svendsen model for magnesium alloys 23
  - 4.2.3. Thermodynamical consistency 23
- 4.3. The Feigenbaum & Dafalias model and its extensions 24
  - 4.3.1. Fundamentals 24
  - 4.3.2. Extensions of the Feigenbaum & Dafalias model for magnesium alloys 26
  - 4.3.3. Thermodynamical consistency 27
- 4.4. Numerical implementation 28

5. Identification of model parameters 29
- 5.1. Experimental basis for parameter calibration 29
- 5.2. Procedure for calibration of model parameters 30
- 5.3. Numerical predictions for non-radial loading paths with the original and the extended models 31
  - 5.3.1. The original models of Teodosiu, Levkovitch & Svendsen and Feigenbaum & Dafalias 32

5.3.2. The extended models calibrated for the Mg alloy AZ31 . 37
5.4. Discussion 43

6. A new thermodynamically consistent constitutive model suitable for magnesium alloys 47
6.1. Fundamentals 47
6.2. Numerical predictions under non-radial loading paths 50
6.3. An alternative derivation of the novel constitutive model 54
6.4. Variational consistency of the new plasticity model 59
6.4.1. Fundamentals 59
6.4.2. Variational consistency of the novel model 61
6.5. Numerical implementation based on the return-mapping algorithm 63
6.5.1. Predictor / corrector algorithm - The return-mapping scheme 63
6.5.1.1. The predictor step 63
6.5.1.2. The corrector step 64
6.5.2. Tangent operator 69
6.5.3. The algorithm for model parameters identification . . . 70

7. Numerical example 73
7.1. Notched bar 73

8. Conclusions and outlook 77

A. Model parameters calibrated for AZ31 79

References 81

1. Introduction

Although much effort has already been spent to understand the macroscopic mechanical response of metallic polycrystals, this topic remains one of the most active research areas in constitutive modeling. Probably most difficult problem associated with a macroscopic description of deformation in polycrystals is to capture the evolution of the microstructure. This complex evolution at the microscale, in turn, leads to a complex mechanical response at the macroscale, cf. Miehe et al. (2002); Roters et al. (2010). Focusing on phenomenological rate-independent plasticity models, the evolution of the microstructure yields an evolving anisotropy of the material. This manifests in the so-called *cross hardening effect* under orthogonal loading-path changes, see Hiwatashi et al. (1998); Wang et al. (2006). Accordingly, whenever strain path changes occur, which is the case in almost every technologically relevant process such as deep-drawing, the distortion of the macroscopic yield function has to be accounted for and thus, classical macroscopic isotropic or kinematic hardening models are not sufficient anymore, cf. Noman et al. (2010); Boers et al. (2010).

Since the macroscopic mechanical response of metallic polycrystals is a direct consequence of the underlying microstructure, a multiscale description seems to be promising. Several researchers have proposed such a modeling approach in which crystal plasticity theory is usually employed at the microscale, cf. Miehe et al. (2002); Roters et al. (2010); Homayonifar & Mosler (2012). By considering a representative volume element (RVE), the transition to the macroscale is realized by a homogenization method, see Miehe et al. (2002). Although such methods are indeed promising, they result in high computational complexity. This is even true, if some approximations such as those known from the mean-field-theory-based self-consistent approaches Lebensohn et al. (2004) or the Taylor model Miehe & Rosato (2007) are made.

A direct phenomenological description provides an alternative to the aforementioned multiscale approaches. Such a description is computationally more efficient and thus, it can be directly applied to the analysis of large-scale engineering problems. However, the improved numerical efficiency comes along without considering the evolution of the underlying microstructure. For instance, the plastic deformation within a certain grain cannot be predicted by a purely macroscopic model. Clearly, this is not surprising, since the macroscopic approach can be interpreted as a projection (homogenization) of some microscopic model. Since the final goal pursued by the author is the modeling of forming processes of magnesium sheets, a direct macroscopic phenomenological description is considered here. The framework of rate-independent finite strain plasticity is adopted.

A macroscopic phenomenological description of magnesium has to capture the most relevant mechanical behaviour encompassing the strength differential effect (different yield stress in tension and compression; abbreviated as SD-effect in the following), the material's initial anisotropy resulting from the underlying atomic lattice (HCP in case of magnesium), and its texture as well as the evolving material's anisotropy due to evolution of the microstructure, cf. Christian & Mahajan (1995). Concerning the SD-effect, Drucker-type yield surfaces (cf. Drucker (1949)) can be employed, see also Cazacu & Barlat (2001, 2004). In contrast to the classical von Mises yield function, they also include the third invariant of the deviatoric stress tensor. Such yield function can be extended for anisotropic materials, e.g. by introducing structural tensors, cf. Johansson et al. (2005); Vladimirov et al. (2010), or by applying a linear transformation to the stress tensor, see Cazacu & Barlat (2004); Barlat et al. (2005, 2007). In summary, the SD-effect as well as the initial anisotropy can be captured in a relatively straightforward manner by existing models.

In contrast to the SD-effect and the initial anisotropy, modeling the effect of the microstructure evolution from a macroscopic point of view is comparably difficult. Only a few approaches have been published in this connection, see e.g. Hiwatashi et al. (1998); Haddadi et al. (2006); Feigenbaum & Dafalias (2007, 2008); Boers et al. (2010); Noman et al. (2010); Pietryga et al. (2012). Concerning the effect of microstructural evolution, two significantly different evolution mechanisms have to be distinguished: grain refinement and coarsening on the one hand and dislocation structures on the other hand. As discussed in Wang et al. (2008), the latter is the major driving source in sheet forming processes. Since the modeling of such processes for magnesium is the overriding goal of the present work, focus is placed on plasticity modeling of the macroscopic mechanical response with distortional hardening.

In order to get an insight into the origin of the topic, Chapter 2 is devoted to a brief introduction on the mechanical behaviour of the commercial Mg alloy AZ31. The fundamentals of continuum mechanics are given in Chapter 3. Based on this, three existing constitutive models are discussed, and extended for the modeling of magnesium in Chapter 4. The first model was published in a series of papers by Teodosiu and co-workers, cf. Hiwatashi et al. (1998); Li et al. (2003); Haddadi et al. (2006), and is referred to as the *Teodosiu model.* The second one was advocated by Levkovitch & Svendsen, cf. Barthel et al. (2008); Noman et al. (2010), and is referred to as the *Levkovitch & Svendsen model.* The third one was proposed in Feigenbaum & Dafalias (2007, 2008); Plesek et al. (2010), and is referred to as the *Feigenbaum & Dafalias model.*

Thermodynamical consistency of the extended models is critically analyzed. The model parameters are identified in Chapter 5. As the only thermodynamically consistent extended model cannot fully capture the mechanical response of Mg alloys, a new constitutive model is developed in Chapter 6. It is found that the new model is thermodynamically and variationally consistent, independent of loading path changes and material parameters. The latter property means that the state variables predicted by the model can be interpreted as stable energy minimization. The applicability of the novel model is finally demonstrated in Chapter 7.

2. Mechanical behaviour of magnesium alloys

Magnesium alloys are the lightest metallic structural materials and are therefore very attractive for applications in the automobile, railway and aerospace industries where mass reduction is an important issue. However, owing to their HCP structure and a limited number of slip systems, Mg alloys exhibit only limited ductility. This limits the range of possible engineering applications of Mg alloys, cf. Roberts (1960); Kelley & Hosford (1968a); Yoo (1981); Avedesian & Baker (1999). Furthermore, magnesium and its alloys show a pronounced strength differential effect as well as strong deformation anisotropy cf. Agnew & Duygulu (2005). The aforementioned mechanical behaviour of magnesium alloys is analyzed in the present chapter.

2.1. Initial plastic anisotropy and strength differential effect

Strongly textured polycrystalline magnesium alloys show differences under tension and compression, i.e., an asymmetry in tension and compression of yield behaviour, also known as strength differential effect (SD effect), see Fig. 2.1. Up to 40 years ago, it was believed that the SD effect of Mg alloys was due to the $\{1\,0\,\bar{1}\,2\}$ twinning that occurs in compression, cf. Hill (1973). Recently, according to Lou et al. (2007); Christian & Mahajan (1995); Wang et al. (2009), the SD effect was shown to originate from the differences in the active modes of deformation twinning. The activation of deformation twinning relies on the availability of a critical dislocation density level in the sample produced by initial dislocation generation and motion. In order to model the SD effect as well as the initial anisotropic yield surface at the macroscale, the so called CB2004 yield function represents a suitable choice, cf. Cazacu & Barlat (2004). In this model, the SD effect is captured by the introduction of the third invariant of deviatoric stress tensor.

2.2. Evolving anisotropy: distortional hardening

After first yielding, an evolution of the anisotropic mechanical behaviour of Mg alloys is observed, see Fig. 2.1 and Fig. 2.2 (right figure). That can be seen

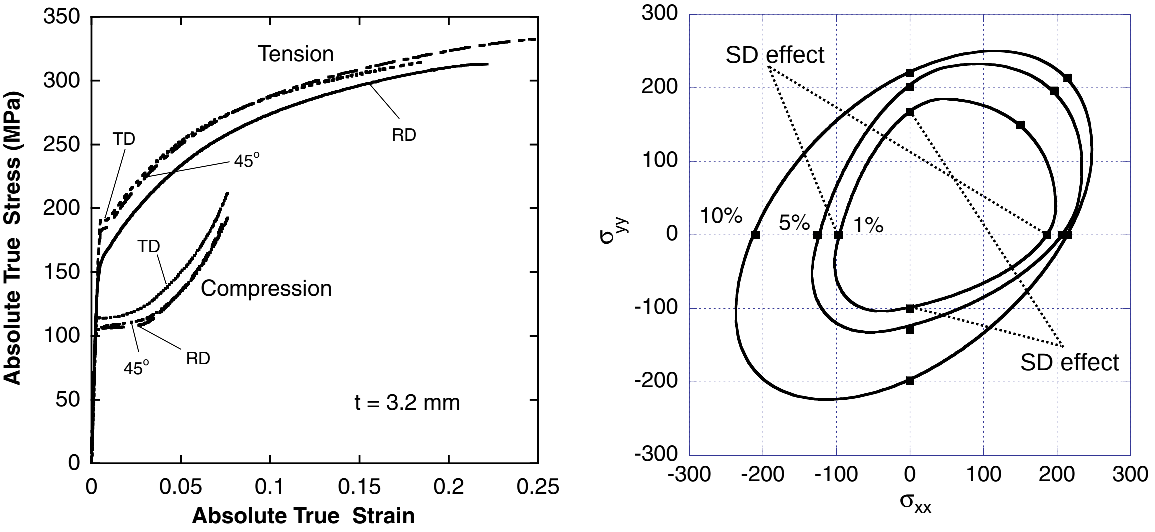

Figure 2.1.: Plastic anisotropy and SD effect of magnesium alloys, left: uniaxial hardening in tension and compression in three directions of 3.2 mm thick AZ31B sheet, cf. Lou et al. (2007); right: comparison between yield loci for a Mg-Th sheet predicted by Cazacu and Barlat model (solid lines, cf. Cazacu et al. (2006)) and experiments (symbols, cf. Kelley & Hosford (1968b))

by the equivalent plastic work contour (or equivalent plastic strain contour), cf. Banabic et al. (2004); Kuwabara et al. (2005); Graff et al. (2007); Steglich et al. (2011); or by the evolution of the yield surface according to continuum plasticity theory, cf. Feigenbaum & Dafalias (2007); Feigenbaum (2008). For isotropic materials under radial loading (loading in which the biaxial stress ratio is maintained constant, cf. Marin & Sauer (1953)), the equivalent plastic contour plot and the evolution of the yield function are almost equivalent. However, that is not the case for non-radial loading cf. Marin & Sauer (1953); Rees (1987).

Although there are differences between the plastic work/strain contour and the yield surfaces, the evolving anisotropy of sheets made of Mg alloys can be shown by both of the aforementioned plots. Commonly it is described by means of the plastic work contour, cf. Kelley & Hosford (1968b); Graff et al. (2007); Steglich et al. (2011). By way of contrast, experimental data for the yield surfaces of metals are limited compared to equivalent plastic work contours, e.g., cf. Bui (1966); Phillips & Juh-Ling (1972); Hecker (1973); D.E. Helling (1986); Xu (1994); M. Boucher (1995); Kurtyka & Zyczkowski (1996); Han-Chin & Wu (2003), for Al alloys. Since the macroscopic modeling of magnesium based on plasticity theory is the focus of the present thesis, the concept of a yield surface represents the more natural choice.

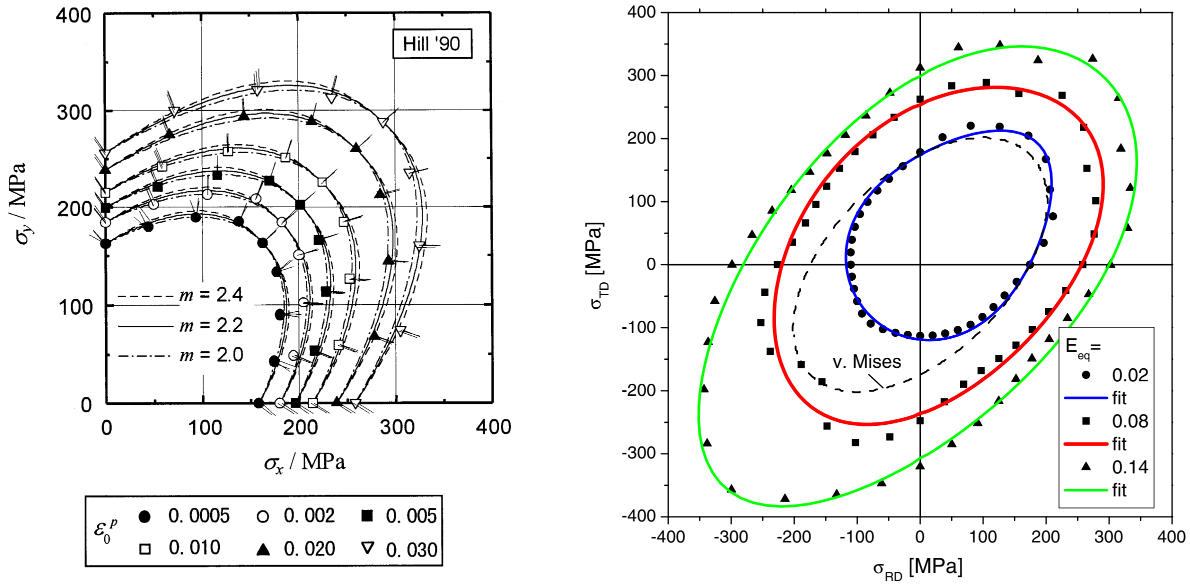

Figure 2.2.: Equivalent plastic work contour, left: comparison of experimental data with Hill's '90 yield loci for cold-rolled low-carbon steel sheet, cf. Kuwabara et al. (1998); right: fit of contours of constant plastic work by means of crystal plasticity model for magnesium alloy (ZM21) sheet, cf. Steglich et al. (2011)

2.3. Loading path dependent distortional hardening

For non-radial loading or loading path changes, the distortional hardening of a metal is better demonstrated by the yield surface compared to an equivalent plastic work contour, see Fig. 2.3. This is due to the fact, that a yield surface corresponds to one state (the internal variables are constant for a certain yield surface). By way of contrast, different (loading) states are combined within an iso-contour plot of the equivalent plastic work. Concerning the anisotropic mechanical behaviour of Mg alloys with loading path changes, an investigation on the hardening behaviour of AZ31B sheet has been carried out, cf. Lou et al. (2007); Proust et al. (2009); Lee et al. (2008, 2009). However, the related constitutive models in Li et al. (2010) are not thermodynamically consistent, i.e., they do not fulfill the second law of thermodynamics.

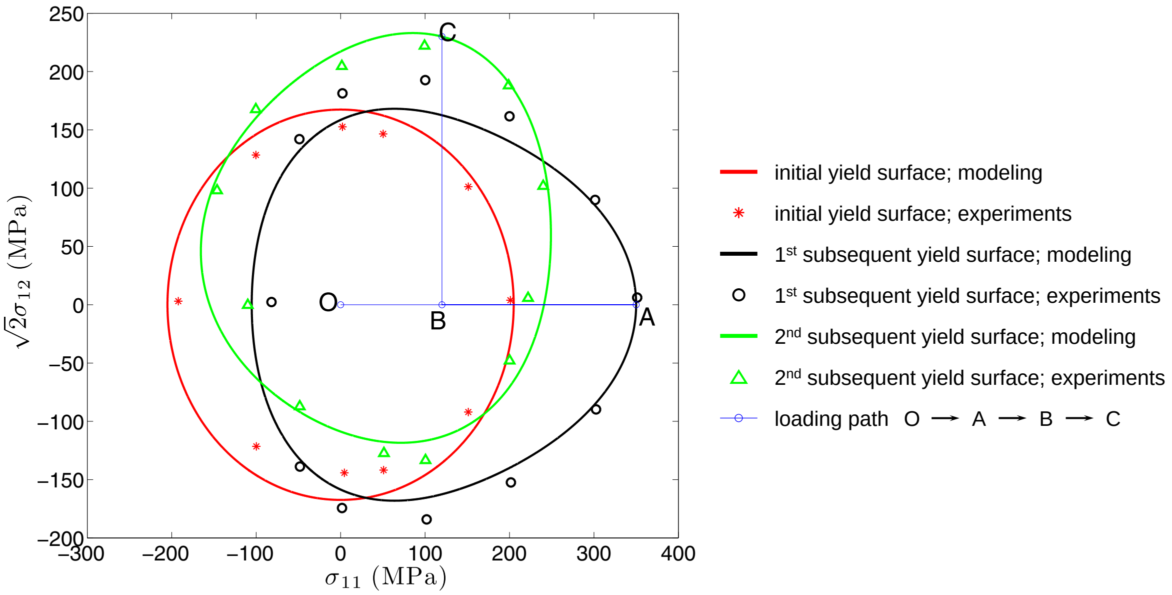

Figure 2.3.: Evolution of yield surfaces under orthogonal loading path change for Al, model by Feigenbaum & Dafalias (solid lines, cf. Feigenbaum & Dafalias (2007); Plesek et al. (2010)); experiments (symbols, cf. M. Boucher (1995))

3. Finite strain plasticity theory in a nutshell

The present chapter is concerned with the fundamentals of finite strain plasticity theory. Most parts of this chapter have been taken from Shi & Mosler (2012).

3.1. Fundamentals

Following standard notations in continuum mechanics, material points P are identified by their position vectors. While such vectors are denoted as $\boldsymbol{X}$ within the undeformed configuration Ω, the lowercase letter $\boldsymbol{x}$ signals the spatial counterpart in the deformed configuration $\boldsymbol{\varphi}(\Omega)$. With these vectors, the deformation mapping $\boldsymbol{\varphi}$ is introduced in standard manner, i.e., $\boldsymbol{\varphi} : \Omega \ni \boldsymbol{X} \to \boldsymbol{x} \in \boldsymbol{\varphi}(\Omega)$. It is locally approximated by the deformation gradient $\boldsymbol{F} := \mathrm{GRAD}\boldsymbol{\varphi} = \partial\boldsymbol{\varphi}/\partial\boldsymbol{X}$.

Since elastoplastic deformation processes are considered within the present work, it is convenient to decompose $\boldsymbol{F}$ into an elastic part $\boldsymbol{F}^{\mathrm{e}}$ and a plastic part $\boldsymbol{F}^{\mathrm{p}}$. More explicitly and in line with Lee (1969), the multiplicative decomposition

$$\boldsymbol{F} = \boldsymbol{F}^{\mathrm{e}} \cdot \boldsymbol{F}^{\mathrm{p}}, \qquad \text{with} \qquad \det\boldsymbol{F}^{\mathrm{e}} > 0,\ \det\boldsymbol{F}^{\mathrm{p}} > 0 \tag{3.1}$$

is adopted for that purpose, cf. Fig. 3.1. Since constitutive models suitable for analyzing plastic deformation are usually based on evolution equations for the inelastic strains $\boldsymbol{F}^{\mathrm{p}}$, deformation rates are also required. Analogously to the standard spatial velocity gradient

$$\boldsymbol{l} := \dot{\boldsymbol{F}} \cdot \boldsymbol{F}^{-1} \tag{3.2}$$

the two additional velocity gradients

$$\boldsymbol{L}^{\mathrm{p}} := \dot{\boldsymbol{F}}^{\mathrm{p}} \cdot [\boldsymbol{F}^{\mathrm{p}}]^{-1}, \qquad \boldsymbol{l}^{\mathrm{e}} := \dot{\boldsymbol{F}}^{\mathrm{e}} \cdot [\boldsymbol{F}^{\mathrm{e}}]^{-1} \tag{3.3}$$

are thus defined. Here, the superposed dot represents the material time derivative.

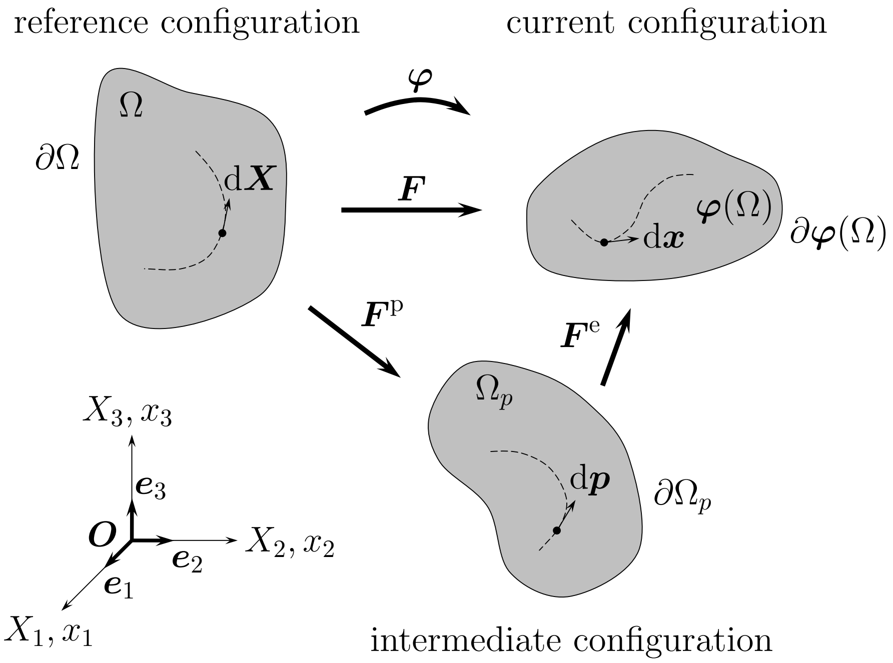
reference configuration
current configuration
Ω
$\partial\Omega$
$\mathrm{d}\boldsymbol{X}$
$\boldsymbol{\varphi}$
$\boldsymbol{F}$
$\boldsymbol{\varphi}(\Omega)$
$\partial\boldsymbol{\varphi}(\Omega)$
$\mathrm{d}\boldsymbol{x}$
$\boldsymbol{F}^{\mathrm{p}}$
$\boldsymbol{F}^{\mathrm{e}}$
Ω_p
$\mathrm{d}\boldsymbol{p}$
$\partial\Omega_p$
X_3, x_3
$\boldsymbol{e}_3$
$\boldsymbol{O}$
$\boldsymbol{e}_2$
X_2, x_2
$\boldsymbol{e}_1$
X_1, x_1
intermediate configuration

Figure 3.1.: Reference, intermediate and current configuration of a material body. It bears emphasize that the intermediate configuration is fictitious, i.e., the decomposition of $\boldsymbol{F}$ is local in nature.

Similarly to the kinematics (3.1), the constitutive response is also decomposed into an elastic part Ψ^{e} and a plastic part Ψ^{p}. To be more precise, the Helmholtz energy Ψ is additively split according to

$$\Psi = \Psi^{\mathrm{e}}(\boldsymbol{F}^{\mathrm{e}}) + \Psi^{\mathrm{p}}(\boldsymbol{\alpha}). \tag{3.4}$$

Here, the energy Ψ^{e} is due to elastic distortion of the underlying atomic lattice, whereas Ψ^{p} depending on the suitable set of internal strain-like variables $\boldsymbol{\alpha}$ is related to plastic hardening. Ψ^{p} will cover classical isotropic and kinematic hardening as well as distortional hardening (distortion of the yield function). Application of the meanwhile standard Coleman & Noll procedure (see Coleman & Gurtin (1967)) yields the stress response

$$\boldsymbol{P} = \partial_{\boldsymbol{F}}\Psi \tag{3.5}$$

together with the reduced dissipation inequality

$$\mathcal{D} = \boldsymbol{\Sigma} : \boldsymbol{L}^{\mathrm{p}} + \boldsymbol{Q} \cdot \dot{\boldsymbol{\alpha}} \geq 0, \qquad \boldsymbol{Q} := -\partial_{\boldsymbol{\alpha}}\Psi. \tag{3.6}$$

Here, $\boldsymbol{P}$ is the first Piola-Kirchhoff stress tensor, $\boldsymbol{\Sigma} = 2\,\boldsymbol{C}^{\mathrm{e}} \cdot \partial_{\boldsymbol{C}^{\mathrm{e}}}\Psi$ is the Mandel stress tensor (with respect to the intermediate configuration) and $\boldsymbol{Q}$ is the stress-like internal variable energetically conjugate to $\boldsymbol{\alpha}$. In addition to the numerical advantages of hyperelastoplastic formulations such as the one defined by Eq. (3.4) (see Simo & Hughes (1998); Simo (1998)), the introduction of a stored energy is also required for proving thermodynamical consistency (e.g. the second law of thermodynamics). An equally important fact is that models not consistently derived from an energy potential such as hypoelastoplasticity approaches do usually not obey the second law of thermodynamics for elastic unloading, cf. Xiao et al. (2000); Bruhns et al. (1999). In summary, the choice of a framework for finite strain plasticity theory is not always only a matter of taste.

While for elastic unloading ($\boldsymbol{L}^{\mathrm{p}} = \boldsymbol{0}$ and $\dot{\boldsymbol{\alpha}} = \boldsymbol{0}$), the dissipation inequality (3.6) is evidently fulfilled, that is not automatically the case for elastoplastic processes. A thermodynamically consistent framework a priori guaranteeing Ineq. (3.6) is that of *generalized standard materials*, cf. Mandel (1971); Lemaitre (1985). This framework requires an additional response function: the so-called *plastic potential* Ω. With this potential Ω, the flow rule and the hardening rules are assumed to be

$$\boldsymbol{L}^{\mathrm{p}} = \lambda\, \partial_{\boldsymbol{\Sigma}}\Omega \qquad \dot{\boldsymbol{\alpha}} = \lambda\, \partial_{\boldsymbol{Q}}\Omega. \tag{3.7}$$

In Eq. (3.7), $\lambda \geq 0$ is the non-negative plastic multiplier. It can be seen in a straightforward manner that Ineq. (3.6) is always fulfilled, provided the plastic potential is convex (and non-negative for plastic loading).

To complete the model, the plastic multiplier $\lambda \geq 0$ has to be determined for elastoplastic loading. Usually, the space of admissible stresses $\mathbb{E}_{\boldsymbol{\Sigma}}$ is introduced for this reason. In line with the reduced dissipation inequality (3.6), this space is formulated in terms of $\boldsymbol{\Sigma}$ and $\boldsymbol{Q}$, i.e.,

$$\mathbb{E}_{\boldsymbol{\Sigma}} = \left\{ (\boldsymbol{\Sigma}, \boldsymbol{Q}) \in \mathbb{R}^{9+n} \;\middle|\; \phi\,(\boldsymbol{\Sigma}, \boldsymbol{Q}) \leq 0 \right\}. \tag{3.8}$$

Here, ϕ is the yield function which has to fulfill certain regularity conditions such as convexity. With the help of space (3.8), the loading and unloading conditions can be written in the classical Karush-Kuhn-Tucker form

$$\lambda\,\phi = 0, \qquad \lambda\,\dot{\phi} = 0. \tag{3.9}$$

and the plastic multiplier λ is computed from the consistency condition $\dot{\phi} = 0$. The constitutive equations defining the finite strain plasticity models are summarized in Tab. 3.1.

Remark 1 *According to Eqs. (3.8) and (3.7), a description with respect to the intermediate configuration is chosen. Such a description is well known to automatically fulfill the principle of material frame indifference. Hence, arbitrary material symmetries can be modeled in a straightforward manner. That is certainly of utmost importance in the case of texture evolution. Although frequently seen in the literature, anisotropic yield functions in terms of Cauchy* *stresses do not automatically fulfill the principle of material frame indifference (except if evolving structural tensors are also introduced, cf. Xiao et al. (2000); Bruhns et al. (1999)).*

3.2. A prototype model for magnesium

A yield function suitable for the modeling of magnesium alloys (polycrystals) has to capture the strength differential effect, the material's symmetry (anisotropy) and, in line with the underlying atomic lattice structure of the material, it should only depend on the stress deviator. Such a function was presented in a series of papers by Barlat and co-workers, cf. Cazacu & Barlat (2004). In line with Mekonen et al. (2012), this model is rewritten in tensor notation here and re-formulated in terms of Mandel stress automatically fulfilling the principle of material frame indifference. Considering isotropic hardening (the related stress-like internal variable is denoted as Q_{iso}) and in contrast to Cazacu & Barlat (2004); Mekonen et al. (2012) also kinematic hardening (the related stress-like internal variable is denoted as $\boldsymbol{Q}_{\text{kin}}$), the yield function reads

$$\phi = J_2^{\frac{3}{2}} - J_3 - Q_0^3 - Q_{\text{iso}}^3. \tag{3.10}$$

Here, Q_0 is the yield stress associated with the initial yield surface and J_2 and J_3 are modified second and third invariants of the effective stresses $\boldsymbol{\Sigma} - \boldsymbol{Q}_{\text{kin}}$. They are defined as

$$J_2 := \frac{1}{2}\,\text{tr}\left[\boldsymbol{\xi}_1 \cdot \boldsymbol{\xi}_1\right], \quad J_3 := \frac{1}{3}\text{tr}\,\left[\boldsymbol{\xi}_2 \cdot \boldsymbol{\xi}_2 \cdot \boldsymbol{\xi}_2\right], \qquad \text{tr}(\bullet) := (\bullet) : \mathbf{1} \tag{3.11}$$

with the linear transformations

$$\boldsymbol{\xi}_i := \mathbb{H}_i : (\boldsymbol{\Sigma} - \boldsymbol{Q}_{\text{kin}}), \qquad i \in \{1; 2\}. \tag{3.12}$$

According to Eq. (3.12), the material's anisotropy is captured by the fourth-order tensors $\mathbb{H}_i$. Consequently, a distortion of the yield surface can be captured by suitable evolution equations of the type $\dot{\mathbb{H}}_i = \mathbb{F}(\lambda)$. Speaking from a physics point of view, such equations are related to the evolution of the underlying microstructure. In the present work, this effect is however not yet considered.

The model is completed by defining evolution equations and the Helmholtz energy. Concerning the latter, the isotropic neo-Hooke-type energy

$$\Psi^{\text{e}}(\boldsymbol{C}^{\text{e}}) = \frac{\Lambda}{4}\left(J^{\text{e}2} - 1\right) - \left(\frac{\Lambda}{2} + \mu\right)\,\ln J^{\text{e}} + \frac{\mu}{2}\,(\text{tr}\boldsymbol{C}^{\text{e}} - 3) \tag{3.13}$$

- Multiplicative decomposition of the deformation gradient $\boldsymbol{F}$

$$\boldsymbol{F} = \boldsymbol{F}^{\mathrm{e}} \cdot \boldsymbol{F}^{\mathrm{p}}, \qquad \text{with} \qquad \det\boldsymbol{F}^{\mathrm{e}} > 0,\ \det\boldsymbol{F}^{\mathrm{p}} > 0.$$

Here, $\boldsymbol{F}^{\mathrm{e}}$ is associated with elastic and $\boldsymbol{F}^{\mathrm{p}}$ with plastic deformations, cf. Lee (1969).

- Additive decomposition of the Helmholtz energy Ψ

$$\Psi = \Psi^{\mathrm{e}}(\boldsymbol{C}^{\mathrm{e}}) + \Psi^{\mathrm{p}}(\boldsymbol{\alpha}), \quad \boldsymbol{C}^{\mathrm{e}} := \boldsymbol{F}^{\mathrm{e}T} \cdot \boldsymbol{F}^{\mathrm{e}}.$$

Ψ^{e} defines the mechanical response to fully reversible deformations, while Ψ^{p} is related to plastic work. $\boldsymbol{\alpha}$ denotes strain-like internal variables governing isotropic, kinematic and distortional hardening. $\boldsymbol{C}^{\mathrm{e}}$ is elastic right Cauchy-Green tensor.

- Definition of the space of admissible stresses $\mathbb{E}_{\boldsymbol{\Sigma}}$

$$\mathbb{E}_{\boldsymbol{\Sigma}} = \left\{(\boldsymbol{\Sigma}, \boldsymbol{Q}) \in \mathbb{R}^{9+n} \;\middle|\; \phi\,(\boldsymbol{\Sigma}, \boldsymbol{Q}) \leq 0\right\}.$$

Here, ϕ is the yield function, $\boldsymbol{\Sigma}$ is the Mandel stress, $\boldsymbol{Q}$ are the stress like internal variables work conjugate to $\boldsymbol{\alpha}$ governing isotropic, kinematic and distortional hardening.

- Non-associative flow rule and hardening law

$$\boldsymbol{L}^{\mathrm{p}} = \lambda\, \partial_{\boldsymbol{\Sigma}}\Omega, \qquad \dot{\boldsymbol{\alpha}} = \lambda\, \partial_{\boldsymbol{Q}}\Omega.$$

Here, Ω is the plastic potential, $\boldsymbol{L}^{\mathrm{p}} := \dot{\boldsymbol{F}}^{\mathrm{p}} \cdot [\boldsymbol{F}^{\mathrm{p}}]^{-1}$ is the plastic velocity gradient and λ is the plastic multiplier.

- Karush-Kuhn-Tucker conditions

$$\lambda\, \phi = 0, \qquad \lambda\, \dot{\phi} = 0.$$

- Reduced dissipation inequality

$$\mathcal{D} = \boldsymbol{\Sigma} : \boldsymbol{L}^{\mathrm{p}} + \boldsymbol{Q} \cdot \dot{\boldsymbol{\alpha}} \geq 0, \qquad \boldsymbol{Q} := -\partial_{\boldsymbol{\alpha}}\Psi.$$

Table 3.1.: Summary of the constitutive equations defining the finite strain plasticity framework used within the present thesis, cf. Lemaitre & Chaboche (1990); Simo & Hughes (1998); Holzapfel (2000)

is adopted, since the elastic response of magnesium is not strongly anisotropic. In Eq. (3.13), Λ and μ represent the Lamé parameters and $J^{\mathrm{e}} := \det \boldsymbol{F}^{\mathrm{e}}$, cf. Ogden (1997). Regarding the part Ψ^{p} of the Helmholtz energy due to cold work, a decoupling of isotropic and kinematic hardening resulting in the additive split

$$\Psi^{\mathrm{p}}(\alpha_{\mathrm{iso}}, \boldsymbol{\alpha}_{\mathrm{kin}}) = \Psi^{\mathrm{p}}_{\mathrm{iso}}(\alpha_{\mathrm{iso}}) + \Psi^{\mathrm{p}}_{\mathrm{kin}}(\boldsymbol{\alpha}_{\mathrm{kin}}) \tag{3.14}$$

is assumed. Here, α_{iso} and $\boldsymbol{\alpha}_{\mathrm{kin}}$ are strain-like internal variables conjugate to $Q_{\mathrm{iso}} := -\partial_{\alpha_{\mathrm{iso}}}\Psi$ and $\boldsymbol{Q}_{\mathrm{kin}} := -\partial_{\boldsymbol{\alpha}_{\mathrm{kin}}}\Psi$, respectively. Furthermore and with focus on non-linear kinematic hardening of Armstrong-Frederick-type, $\Psi^{\mathrm{p}}_{\mathrm{kin}}$ is specified to

$$\Psi^{\mathrm{p}}_{\mathrm{kin}}(\boldsymbol{\alpha}_{\mathrm{kin}}) = \frac{1}{2}\, c_{\mathrm{kin}}\, \boldsymbol{\alpha}_{\mathrm{kin}} : \boldsymbol{\alpha}_{\mathrm{kin}} \tag{3.15}$$

where c_{kin} is the kinematic hardening modulus. Finally, the plastic potential

$$\Omega = \phi + \frac{1}{2}\,\frac{b_{\mathrm{kin}}}{c_{\mathrm{kin}}}\, \boldsymbol{Q}_{\mathrm{kin}} : \boldsymbol{Q}_{\mathrm{kin}} \tag{3.16}$$

defining the flow rule and the evolution equations is adopted, see Eq. (3.7). The model parameter b_{kin} defines the saturation value of the back strain $\boldsymbol{\alpha}_{\mathrm{kin}}$. According to Eq. (3.16), an associative flow rule and an associative evolution equation for isotropic hardening are chosen, whereas kinematic hardening is governed by the differential equation

$$\dot{\boldsymbol{\alpha}}_{\mathrm{kin}} = \lambda\, \partial_{\boldsymbol{Q}_{\mathrm{kin}}}\Omega = -\lambda\, \partial_{\boldsymbol{\Sigma}}\phi - \lambda\, b_{\mathrm{kin}}\, \boldsymbol{\alpha}_{\mathrm{kin}}. \tag{3.17}$$

Neglecting kinematic hardening, model parameters calibrated for the magnesium alloys AZ31 and ZE10 can be found in Mekonen et al. (2012).

Remark 2 *Since usually* $||\partial_{\boldsymbol{\Sigma}}\phi|| \neq 1$*, the flow direction* $\partial_{\boldsymbol{\Sigma}}\phi$ *in Eq. (3.17) is often replaced by its normalized counterpart* $\boldsymbol{N} := \partial_{\boldsymbol{\Sigma}}\phi / ||\partial_{\boldsymbol{\Sigma}}\phi||$*. Combining this with* $\boldsymbol{Q}_{\mathrm{kin}} = -c_{\mathrm{kin}}\, \boldsymbol{\alpha}_{\mathrm{kin}}$ *yields*

$$\dot{\boldsymbol{Q}}_{\mathrm{kin}} = c_{\mathrm{kin}} \left(\boldsymbol{N} - \frac{b_{\mathrm{kin}}}{c_{\mathrm{kin}}}\, \boldsymbol{Q}_{\mathrm{kin}} \right) \lambda. \tag{3.18}$$

This representation of kinematic hardening will frequently be used in the present work.

4. Models suitable for the analysis of magnesium alloys

The present chapter is concerned with a critical review of existing distortional hardening models. To be more precise, the Teodosiu model (see Hiwatashi et al. (1998); Haddadi et al. (2006)), the Levkovitch & Svendsen model (see Barthel et al. (2008); Noman et al. (2010)) and the Feigenbaum & Dafalias model (see Feigenbaum & Dafalias (2007, 2008)) are analyzed and compared. For a better comparison, they are reformulated into the modern framework of hyperelastoplasticity and the same consistent notation is used for the description of every model. In addition to the review, the extensions necessary for the modeling of texture evolution in magnesium alloys are also discussed. Finally, the fulfillment of fundamental principles of material modeling such as thermodynamical consistency is checked for the resulting novel models.

Most parts of this chapter have been taken from Shi & Mosler (2012).

4.1. The Teodosiu model and its extensions

4.1.1. Fundamentals

The fundamentals of the Teodosiu model are briefly given here. However and in contrast to the original works Hiwatashi et al. (1998); Peeters et al. (2002); Li et al. (2003); Haddadi et al. (2006), the notations as introduced within the previous chapter are used here.

The Teodosiu model is based on the modified Hill-type yield function

$$\phi = \bar{\Sigma}_{\mathrm{e}} - Q_0 - Q_{\mathrm{iso}} - f||\mathbb{S}|| \tag{4.1}$$

with the equivalent relative stress

$$\bar{\Sigma}_{\mathrm{e}} = \sqrt{(\mathrm{dev}\boldsymbol{\Sigma} - \boldsymbol{Q}_{\mathrm{kin}}) : \mathbb{H} : (\mathrm{dev}\boldsymbol{\Sigma} - \boldsymbol{Q}_{\mathrm{kin}})}. \tag{4.2}$$

where $\mathrm{dev}\boldsymbol{\Sigma}$ is the deviator of $\boldsymbol{\Sigma}$, f is a model parameter and $\mathbb{H}$ and $\mathbb{S}$ are two fourth-order tensors. It bears emphasis that, in contrast to the original model, Mandel stresses are considered here. The principle of material frame indifference is thereby fulfilled. The fourth-order tensor $\mathbb{H}$ in Eq. (4.2) defines the symmetry of the material which is kept constant in the original Teodosiu model ($\dot{\mathbb{H}} = \mathbf{0}$). The only non-standard term in the yield function (4.1) is the fourth-order tensor $\mathbb{S}$. As will be shown, this tensor captures, among others, the cross hardening effect (see Haddadi et al. (2006)).

Isotropic and kinematic hardening are governed by the classical Armstrong-Frederick evolution equations (compare to Eq. (3.18))

$$\dot{Q}_{\mathrm{iso}} = c_{\mathrm{iso}}\ (Q^{\infty}_{\mathrm{iso}} - Q_{\mathrm{iso}})\ \lambda \tag{4.3}$$

and

$$\dot{\boldsymbol{Q}}_{\mathrm{kin}} = c_{\mathrm{kin}}\ (Q^{\infty}_{\mathrm{kin}}\ \boldsymbol{N} - \boldsymbol{Q}_{\mathrm{kin}})\ \lambda, \qquad \boldsymbol{N} := \frac{\partial_{\boldsymbol{\Sigma}}\phi}{\|\partial_{\boldsymbol{\Sigma}}\phi\|}. \tag{4.4}$$

In line with the notation introduced in the previous chapter, c_{iso} and c_{kin} are the isotropic and the kinematic hardening moduli and $Q^{\infty}_{\mathrm{iso}}$ and $Q^{\infty}_{\mathrm{kin}}$ are the saturation limits associated with isotropic and kinematic hardening. The only, but nevertheless crucial, difference compared to standard non-linear kinematic hardening is that the saturation limit $Q^{\infty}_{\mathrm{kin}}$ is not a constant model parameter, but depends on the fourth-order tensor $\mathbb{S}$. Before giving the explicit expression, the physical interpretation of $\mathbb{S}$ is briefly discussed.

Within the Teodosiu model, the strength due to dislocation structures is decomposed into a part associated with the currently active slip systems (denoted as $\mathbb{S}_{\mathrm{D}}$) and the one related to latent slip systems (denoted as $\mathbb{S}_{\mathrm{L}}$). For such parts, Teodosiu postulated the evolution equations

$$\dot{\mathbb{S}}_{\mathrm{L}} = -c_{\mathrm{SL}}\ \left(\frac{\|\mathbb{S}_{\mathrm{L}}\|}{S^{\infty}}\right)^{n_{\mathrm{L}}}\ \mathbb{S}_{\mathrm{L}}\ \lambda \tag{4.5}$$

and

$$\dot{S}_{\mathrm{D}} = c_{\mathrm{SD}}\ [g\ \ (S^{\infty} - S_{\mathrm{D}}) - h\ S_{\mathrm{D}}]\ \lambda. \tag{4.6}$$

According to Eqs. (4.5) and (4.6), no evolution equation for the total tensor $\mathbb{S}$ is assumed. As stated in Wang et al. (2008), that leads to mathematical problems. To be more precise, the Teodosiu model is overdetermined from a mathematical point of view. However, this deficiency is not crucial, since it can be eliminated in a straightforward manner, cf. Wang et al. (2008). The respective modification has been considered in the final implementation. While c_{SL}, c_{SD}, n_{L} and S^{∞} are constant model parameters, g and h are deformation-dependent. Without going into too much detail, such functions are related to the effects of work hardening stagnation and resumption, cf. Haddadi et al.

(2006). These effects, although important for some applications, are not the focus of the present thesis. Therefore, they are not discussed here. The interested reader is referred to Remark 3.

Having defined the evolution of the fourth-order tensor $\mathbb{S}$, the saturation value Q_{kin}^{∞} is postulated to be

$$Q_{\text{kin}}^{\infty} = Q_{\text{kin}}^{(0)} + (1-f)\sqrt{r_{\text{t}}\;||\mathbb{S}||^2 + (1-r_{\text{t}})\;S_{\text{D}}^2} \tag{4.7}$$

where r_{t} is a weighting factor and $Q_{\text{kin}}^{(0)}$ is another model parameter. Accordingly and in sharp contrast to a conventional Armstrong-Frederick-type law, the saturation value is non-constant and implicitly depends on the loading path. Furthermore, Eq. (4.7) implies a strong coupling between kinematic and distortional hardening.

To understand the fundamentals of the model, a monotonic uniaxial loading test followed by orthogonal loading is considered. Assuming a well-annealed material ($\mathbb{S} = \mathbf{0}$), $\mathbb{S} = S_{\text{D}}\boldsymbol{N}_1 \otimes \boldsymbol{N}_1$ during the first loading stage with $\boldsymbol{N}_1$ denoting the respective (constant) flow direction. Furthermore, $\mathbb{S}_{\text{L}} = \mathbf{0}$. Altogether, that leads to a standard coupled isotropic/kinematic hardening response within a kinematic saturation limit of $Q_{\text{kin}}^{\infty} = Q_{\text{kin}}^{(0)} + (1-f)\;||\mathbb{S}||$ (since $||\mathbb{S}|| = S_{\text{D}}$ during the first loading stage). When the loading path is subsequently changed, indicated by $\boldsymbol{N}_2$, the new initial conditions are $S_{\text{D}} = \boldsymbol{N}_2 : \mathbb{S} : \boldsymbol{N}_2$ and $\mathbb{S}_{\text{L}} = \mathbb{S} - S_{\text{D}}\boldsymbol{N}_2 \otimes \boldsymbol{N}_2$. Consequently, the part of $\mathbb{S}$ which was related to the currently active dislocations during the first loading stage, now corresponds to latent slip systems. While isotropic hardening is not affected by this flip, since it depends only on the equivalent plastic strain α_{iso} and the norm of $\mathbb{S}$, it leads to the different saturation value $Q_{\text{kin}}^{\infty} = Q_{\text{kin}}^{(0)} + (1-f)\;\sqrt{r_{\text{t}}}\;||\mathbb{S}||$ for kinematic hardening. Thus, if $r_{\text{t}} > 1$, the new saturation value is higher, resulting in a cross hardening effect.

A careful analysis reveals that isotropic, kinematic and distortional hardening are strongly coupled within the Teodosiu model. For this reason, a precise interpretation of the model and its interactions is not straightforward, although the underlying idea can be relatively well understood by considering the aforementioned mechanical experiment (orthogonal loading). Furthermore and equally important, the cross hardening effect is only taken into account through kinematic hardening. That can be seen as follows: Isotropic hardening cannot contribute to cross hardening. Furthermore, $||\mathbb{S}||$ is also constant, if the loading path changes. Therefore, the only possibility to describe cross hardening is through the back stress, see Eq. (4.1). This is indeed the case, since the saturation value Q_{kin}^{∞} is sensitive with respect to a change of the loading path as discussed in the previous paragraph. However, that is the only consideration of cross hardening within the model. In particular, a distortion of the yield function is not accounted for. In summary, the main motivation for the Teodosiu model seems to be the precise description of work hardening stagnation, softening and resumption.

Remark 3 *For the sake of completeness, the functions g and h governing the evolution of $\mathbb{S}$ due to currently active dislocations are briefly discussed, cf. Eq. (4.6). The latter is given by*

$$h = \frac{1}{2}\left(1 - \frac{\boldsymbol{Q}_{\text{kin}} : \boldsymbol{N}}{Q^{\infty}_{\text{kin}}\,(\text{dev}\boldsymbol{\Sigma} - \boldsymbol{Q}_{\text{kin}}) : \boldsymbol{N}}\,\bar{\Sigma}_{\text{e}}\right). \tag{4.8}$$

Accordingly, Eq. (4.8) defines an interaction between kinematic hardening and the fourth-order tensor $\mathbb{S}$ and leads to a small decrease in S_{D} (the rate) at the beginning of a reversed deformation path, cf. Haddadi et al. (2006).

In contrast to h, the function g depends on the so-called polarity tensor $\mathcal{P}$ *introduced by the Armstrong-Frederick-rule*

$$\dot{\mathcal{P}} = c_P\,(\boldsymbol{N} - \mathcal{P})\;\lambda \tag{4.9}$$

Here, c_P is a model parameter. In the sense of physics, $\mathcal{P}$ grows into the direction of the current plastic flow direction. However, $\mathcal{P}$ does not change its direction spontaneously which is implemented by the memory term $\mathcal{P}\;\lambda$ in Eq. (4.9). Loading path changes can be identified by the projection

$$P_{\text{D}} = \mathcal{P} : \boldsymbol{N}. \tag{4.10}$$

With this projection, the function g in Eq. (4.6) is defined as

$$g = \begin{cases} 1 - \frac{c_P}{c_{\text{SD}}+c_P}\left|\frac{S_{\text{D}}}{S^{\infty}} - P_{\text{D}}\right| & \textit{if } P_{\text{D}} \geq 0 \\ (1 + P_{\text{D}})^{n_P}\left(1 - \frac{c_P}{c_{\text{SD}}+c_P}\frac{S_{\text{D}}}{S^{\infty}}\right) & \textit{otherwise} \end{cases} \tag{4.11}$$

where n_P is another model parameter. As explained in Haddadi et al. (2006), the continuous function g has been designed to capture work hardening stagnation and resumption.

4.1.2. Extensions of the Teodosiu model for magnesium alloys

By combining Eqs. (3.10) and (4.1), the Teodosiu model can be incorporated into the CB2004 yield function, cf. Cazacu & Barlat (2004), i.e.

$$\phi = J_2^{\frac{3}{2}} - J_3 - Q_0^3 - Q_{\text{iso}}^3 - f\,\|\mathbb{S}\|, \tag{4.12}$$

Certainly, two different fourth-order tensors $\mathbb{S}_1$ and $\mathbb{S}_2$ could also have been introduced resulting in

$$\phi = J_2^{\frac{3}{2}} - J_3 - Q_0^3 - Q_{\text{iso}}^3 - f_1 \, \|\mathbb{S}_1\| - f_2 \, \|\mathbb{S}_2\|. \tag{4.13}$$

However, since $\mathbb{S}$ affects only isotropic and kinematic hardening, both formulations are essentially equivalent. Due to computational efficiency, only one tensor $\mathbb{S}$ is thus chosen here. In line with Wang et al. (2008), this tensor is assumed to be governed by the evolution equation

$$\dot{\mathbb{S}} = \underbrace{\lambda \, g \, c_{\text{SD}} \, S^{\infty} \, \boldsymbol{N} \otimes \boldsymbol{N} - \lambda \, (g+h) \, c_{\text{SD}} \, S_{\text{D}} \, \boldsymbol{N} \otimes \boldsymbol{N}}_{= \dot{S}_{\text{D}} \, \boldsymbol{N} \otimes \boldsymbol{N}, \text{ see Eq. (4.6)}} \underbrace{- \lambda \, c_{\text{SL}} \left\{ \frac{\|\mathbb{S}_{\text{L}}\|}{S^{\infty}} \right\}^{n_{\text{L}}} \mathbb{S}_{\text{L}}}_{= \dot{\mathbb{S}}_{\text{L}}, \text{ see Eq. (4.5)}} . \tag{4.14}$$

Although formally identical to Eq. (4.6) and Eq. (4.5), the modified Teodosiu-type evolution equation (4.14) solves the mathematical inconsistencies of the original model, cf. Wang et al. (2008). While the function g in Eq. (4.14) has not to be changed, that is not the case for h. This function reads

$$h = \frac{1}{2} \left(1 - \frac{\boldsymbol{Q}_{\text{kin}} : \boldsymbol{N}}{Q_{\text{kin}}^{\infty} \, (\text{dev}\boldsymbol{\Sigma} - \boldsymbol{Q}_{\text{kin}}) : \boldsymbol{N}} \bar{\Sigma}_{\text{e}} \right), \tag{4.15}$$

and hence, it depends through $\bar{\Sigma}_{\text{e}}$ on the shape of the yield function, see Eqs. (4.1) and (4.2). Inspired by Eq. (4.12), the equivalent stress measure $\bar{\Sigma}_{\text{e}}$ is chosen as

$$\bar{\Sigma}_{\text{e}} = \left| \left(J_2^{\frac{3}{2}} - J_3 \right)^{\frac{1}{3}} \right|. \tag{4.16}$$

The remaining equations do not have to be modified, i.e., isotropic and kinematic hardening are still governed by Eqs. (4.3) and (4.4) and an associative flow rule is adopted.

4.1.3. Thermodynamical consistency

In the present section, thermodynamical consistency of the resulting model is analyzed. Since thermodynamical aspects have not been considered in the original Teodosiu model, some additional assumptions are required. Strictly speaking, without specifying an energy, one can neither prove nor disprove thermodynamical consistency.

To analyze thermodynamical consistency, the additional assumption

$$\Psi^{\mathrm{p}} = \Psi^{\mathrm{p}}_{\mathrm{iso}}(\alpha_{\mathrm{iso}}) + \Psi^{\mathrm{p}}_{\mathrm{kin}}(\boldsymbol{\alpha}_{\mathrm{kin}}) + \Psi^{\mathrm{p}}_{\mathrm{dis}}(\mathbb{E}), \qquad \mathbb{S} := -\partial_{\mathbb{E}}\Psi \tag{4.17}$$

is made, i.e., the energy due to cold work is decomposed into isotropic, kinematic and distortional hardening (or cross hardening). While the exponential function

$$\Psi^{\mathrm{p}}_{\mathrm{iso}}(\alpha_{\mathrm{iso}}) = Q^{\infty}_{\mathrm{iso}}\ \left(\alpha_{\mathrm{iso}} + \exp\left[-c_{\mathrm{iso}}\ \alpha_{\mathrm{iso}}\right]\right) \tag{4.18}$$

is assumed for isotropic hardening, quadratic functions are chosen for kinematic and cross hardening, i.e.

$$\Psi^{\mathrm{p}}_{\mathrm{kin}} := \frac{\tilde{c}_{\mathrm{kin}}}{2}\boldsymbol{\alpha}_{\mathrm{kin}} : \boldsymbol{\alpha}_{\mathrm{kin}}, \quad \Psi^{\mathrm{p}}_{\mathrm{dis}} := \frac{c_{\mathrm{dist}}}{2}\mathbb{E} :: \mathbb{E}. \tag{4.19}$$

Here $\mathbb{E}$ is an internal variable conjugate to $\mathbb{S}$. Since the closed-form solution of Eq. (4.3) yields an exponential hardening response $Q(\alpha_{\mathrm{iso}})$, Eq. (4.18) is equivalent to the assumption within the original Teodosiu model. The quadratic functions (4.19) are motivated from the analogy between Eq. (4.4) and the classical Armstrong-Frederick model (compare Eq. (4.19) to Eq. (3.15) and Eq. (4.4) to Eq. (3.17)).

With such assumptions, the reduced dissipation inequality (3.6) is obtained as

$$\mathcal{D} = \lambda\boldsymbol{\Sigma} : \frac{\partial\phi}{\partial\boldsymbol{\Sigma}} + \Big(Q_{\mathrm{iso}}\dot{\alpha}_{\mathrm{iso}} + \boldsymbol{Q}_{\mathrm{kin}} : \dot{\boldsymbol{\alpha}}_{\mathrm{kin}} + \mathbb{S} :: \dot{\mathbb{E}}\Big) \geq 0. \tag{4.20}$$

Implicitly, the existence of a hyperelastic response has been assumed in Ineq. (4.20), see Eq. (3.4). Inserting the evolution equations (4.14, 4.4), together with the associative flow rule $\boldsymbol{L}^{\mathrm{p}} = \lambda\ \partial_{\boldsymbol{\Sigma}}\phi$ and the associative hardening rule

$$\dot{\alpha}_{\mathrm{iso}} = \lambda\frac{\partial\phi}{\partial Q_{\mathrm{iso}}} = -3\,\lambda\,Q^2_{\mathrm{iso}}. \tag{4.21}$$

into the reduced dissipation inequality (4.20) yields, after a lengthy but nevertheless straightforward transformation:

$$\begin{aligned}
\mathcal{D} \quad = \quad & 3\,\lambda\,Q_0^3 + 3\,\lambda\,f\,\|\mathbb{S}\| \\
& +\lambda\left(\left\|\frac{\partial\phi}{\partial\boldsymbol{\Sigma}}\right\| - \frac{c_{\mathrm{kin}}}{\tilde{c}_{\mathrm{kin}}}Q^{\infty}_{\mathrm{kin}}\right)\boldsymbol{Q}_{\mathrm{kin}} : \boldsymbol{N} + \lambda\,\frac{c_{\mathrm{kin}}}{\tilde{c}_{\mathrm{kin}}}\boldsymbol{Q}_{\mathrm{kin}} : \boldsymbol{Q}_{\mathrm{kin}} \\
& +\lambda\,\left(\frac{c_{\mathrm{SD}}}{c_{\mathrm{dist}}}\,(g+h)\,\boldsymbol{N} : \mathbb{S} : \boldsymbol{N} - \frac{\lambda\,c_{\mathrm{SD}}\,S^{\infty}}{c_{\mathrm{dist}}}\,g\right)\mathbb{S} :: (\boldsymbol{N}\otimes\boldsymbol{N}) \\
& +\lambda\,\frac{c_{\mathrm{SL}}}{c_{\mathrm{dist}}}\,\left\{\frac{\|\mathbb{S} - (\boldsymbol{N} : \mathbb{S} : \boldsymbol{N})\ \boldsymbol{N}\otimes\boldsymbol{N}\|}{S^{\infty}}\right\}^{n_{\mathrm{L}}}\,\mathbb{S} \\
& :: \left[\mathbb{S} - (\boldsymbol{N} : \mathbb{S} : \boldsymbol{N})\ \boldsymbol{N}\otimes\boldsymbol{N}\right] \geq 0.
\end{aligned} \tag{4.22}$$

Here, the positive homogeneity of degree three of the yield function with respect to isotropic, distortional hardening and the relative stresses has been used (for each of the aforementioned variables independently, see Remark 10). The terms $3\ \lambda\ Q_0^3$, $3\ \lambda\ f\,\|\mathbb{S}\|$ and $\lambda\ c_{\text{kin}}/\tilde{c}_{\text{kin}}\ \boldsymbol{Q}_{\text{kin}} : \boldsymbol{Q}_{\text{kin}}$ are clearly non-negative. Accordingly, sufficient conditions for thermodynamical consistency are given by

$$\lambda\left(\left\|\frac{\partial\phi}{\partial\boldsymbol{\Sigma}}\right\| - \frac{c_{\text{kin}}}{\tilde{c}_{\text{kin}}}Q_{\text{kin}}^{\infty}\right)\boldsymbol{Q}_{\text{kin}} : \boldsymbol{N} \geq 0 \tag{4.23}$$

and

$$\begin{aligned}\lambda\ &\left(\frac{c_{\text{SD}}}{c_{\text{dist}}}\,(g+h)\,\boldsymbol{N} : \mathbb{S} : \boldsymbol{N} - \frac{\lambda\, c_{\text{SD}}\, S^{\infty}}{c_{\text{dist}}}\, g\right)\mathbb{S} :: (\boldsymbol{N}\otimes\boldsymbol{N})\\ &+\lambda\ \frac{c_{\text{SL}}}{c_{\text{dist}}}\left\{\frac{\|\mathbb{S} - (\boldsymbol{N} : \mathbb{S} : \boldsymbol{N})\ \boldsymbol{N}\otimes\boldsymbol{N}\|}{S^{\infty}}\right\}^{n_{\text{L}}}\ \mathbb{S}\\ &:: [\mathbb{S} - (\boldsymbol{N} : \mathbb{S} : \boldsymbol{N})\ \boldsymbol{N}\otimes\boldsymbol{N}] \geq 0.\end{aligned} \tag{4.24}$$

Such inequalities are evidently highly non-linear and thus, cannot be enforced in a straightforward manner. Unfortunately, without enforcing them, the dissipation inequality is usually not fulfilled. That could be confirmed by several numerical simulations.

4.2. The Levkovitch & Svendsen model and its extensions

4.2.1. Fundamentals

The fundamentals of the Levkovitch & Svendsen model are concisely reviewed here. Further details can be found in Noman et al. (2010).

Neglecting distortional hardening, the Levkovitch & Svendsen model represents a special case of the Teodosiu model presented in the previous section. For instance, the yield function is obtained by setting the model parameter f in Eq. (4.1) to zero resulting in

$$\phi = \bar{\Sigma}_{\text{e}} - Q_0 - Q_{\text{iso}} \tag{4.25}$$

with

$$\bar{\Sigma}_{\text{e}} = \sqrt{(\text{dev}\boldsymbol{\Sigma} - \boldsymbol{Q}_{\text{kin}}) : \mathbb{H} : (\text{dev}\boldsymbol{\Sigma} - \boldsymbol{Q}_{\text{kin}})}. \tag{4.26}$$

Furthermore, isotropic hardening is again defined by

$$\dot{Q}_{\text{iso}} = c_{\text{iso}}(Q_{\text{iso}}^{\infty} - Q_{\text{iso}})\ \lambda \tag{4.27}$$

whereas kinematic hardening is still governed by the evolution equation

$$\dot{\boldsymbol{Q}}_{\text{kin}} = c_{\text{kin}}(Q_{\text{kin}}^{\infty}\,\boldsymbol{N} - \boldsymbol{Q}_{\text{kin}})\,\lambda. \tag{4.28}$$

In contrast to the Teodosiu model, the material parameters c_{kin} and Q_{kin}^{∞} in Eq. (4.28) are now constant, i.e., standard Armstrong-Frederick-type evolution equations are used (or Voce rule in the case of isotropic hardening).

Again in line with the Teodosiu model, the effects due to currently active dislocations (denoted as dynamic part in the Levkovitch & Svendsen model; indicated by the subscript D) and latent slip systems (denoted as latent part in the Levkovitch & Svendsen model; indicated by the subscript L) are described by a fourth-order tensor $\mathbb{B}$. Its evolution is assumed to be

$$\dot{\mathbb{B}} = c_{\text{D}}\;(s_{\text{D}}\,\boldsymbol{N}\otimes\boldsymbol{N} - \mathbb{B}_{\text{D}})\,\lambda + c_{\text{L}}\;[s_{\text{L}}\;(\mathbb{I}_{\text{dev}} - \boldsymbol{N}\otimes\boldsymbol{N}) - \mathbb{B}_{\text{L}}]\;\lambda, \tag{4.29}$$

where $\mathbb{I}_{\text{dev}}$ is the fourth-order deviatoric projection tensor ($\text{dev}\boldsymbol{A} = \mathbb{I}_{\text{dev}} : \boldsymbol{A}$, $\forall\boldsymbol{A}$). Accordingly, the first term governing the dynamic part is of Armstrong-Frederick-type. The similarity to the Teodosiu model becomes evident, if the functions g and h in Eq. (4.14) are assumed as constant and uniaxial tension is considered. In this case, only the part due the currently active slip systems evolves yielding an evolution equation of the form

$$\dot{\mathbb{S}} = \lambda\,\hat{A}\,\boldsymbol{N}\otimes\boldsymbol{N} - \lambda\,\hat{B}\,\mathbb{S} \tag{4.30}$$

for the Teodosiu model. By comparing Eq. (4.30) to the first term in Eq. (4.29), it can be clearly seen that the dynamic part in the Levkovitch & Svendsen model is a special case of the Teodosiu model. In contrast to Haddadi et al. (2006), the same evolution equation is also used for the latent part within the Levkovitch & Svendsen model, see Eq. (4.29).

So far, the Levkovitch & Svendsen model can be interpreted as a special case of the Teodosiu model in which hardening stagnation, softening and resumption have been excluded (the functions g and h are constant model parameters). However, the crucial difference is that the fourth-order tensor $\mathbb{B}$ directly affects the shape of the yield function. This idea goes back to Baltov & Sawczuk (1965) and is implemented within the Levkovitch & Svendsen model by setting

$$\dot{\mathbb{H}} = \dot{\mathbb{B}}. \tag{4.31}$$

As a consequence of Eq. (4.31), the shape of the yield surface changes during deformation. That allows inclusion of the cross hardening effect in a consistent manner. Another important feature of the Levkovitch & Svendsen model is that isotropic, kinematic and distortional hardening are uncoupled (the evolution equations). Hereby, the physical interpretation of the equations becomes less complicated.

4.2.2. Extensions of the Levkovitch & Svendsen model for magnesium alloys

To model magnesium, the Hill yield function defined by Eqs. (4.25) and (4.26) is again replaced by the one proposed by Barlat and co-workers (Cazacu & Barlat, 2004), i.e.

$$\phi = J_2^{\frac{3}{2}} - J_3 - Q_0^3 - Q_{\text{iso}}^3. \tag{4.32}$$

According to Eqs. (3.10) and (3.11), the material's symmetry is captured within the CB2004 yield function by the two fourth-order transformation tensors $\mathbb{H}_i$ ($J_2 = J_2(\mathbb{H}_1)$ and $J_3 = J_3(\mathbb{H}_2)$). Therefore, it is reasonable to introduce two independent evolution equations of the type (4.29). Consequently,

$$\dot{\mathbb{H}}_i = \lambda\, c_{\text{D}i}\ (s_{\text{D}i}\, \boldsymbol{N} \otimes \boldsymbol{N} - \mathbb{H}_{\text{D}i}) + \lambda\, c_{\text{L}i}\, [s_{\text{L}i}\ (\mathbb{I}_{\text{dev}} - \boldsymbol{N} \otimes \boldsymbol{N}) - \mathbb{H}_{\text{L}i}] \quad i \in \{1; 2\} \tag{4.33}$$

is chosen.

Eqs. (4.32) and (4.33) are the only modifications required to adapt the Levkovitch & Svendsen model to magnesium. Isotropic and kinematic hardening are assumed to be still governed by Eqs. (4.27) and (4.28).

4.2.3. Thermodynamical consistency

Analogously to the Teodosiu model, thermodynamical aspects have not been considered in the original Levkovitch & Svendsen model. Particularly, no Helmholtz energy was introduced. However an energy is required in order to analyze the Second Law of thermodynamics. For this reason, some additional assumptions are required.

The first assumption is the existence of a Helmholtz energy Ψ which is additively decomposed into Ψ^{e} and Ψ^{p}. While the neo-Hooke model (3.13) is adopted for Ψ^{e}, Ψ^{p} is additively split into the different hardening mechanisms, see Eqs. (4.17). This split agrees with an uncoupling of the hardening mechanisms as considered within the original Levkovitch & Svendsen model. Assuming further that the hardening mechanisms governing the tensors $\mathbb{H}_1$

and $\mathbb{H}_2$ are also uncoupled leads eventually to

$$\Psi^{\mathrm{p}}_{\mathrm{dis}} = \Psi^{\mathrm{p}}_{\mathrm{dis1}} + \Psi^{\mathrm{p}}_{\mathrm{dis2}}, \quad \Psi^{\mathrm{p}}_{\mathrm{dis}i} := \frac{1}{2}\, c_{\mathrm{dis}i}\, \mathbb{E}_i :: \mathbb{E}_i, \quad \mathbb{H}_i := -\partial_{\mathbb{E}_i} \Psi^{\mathrm{p}}. \tag{4.34}$$

Again choosing the exponential function (4.18) and the associative evolution equation (4.21) for isotropic hardening, the quadratic energy $(4.19)_1$ for kinematic hardening, together with the associative flow rule $\boldsymbol{L}^{\mathrm{p}} = \lambda\ \partial_{\boldsymbol{\Sigma}} \phi$, the reduced dissipation inequality

$$\mathcal{D} = \boldsymbol{\Sigma} : \boldsymbol{L}^{\mathrm{p}} + Q_{\mathrm{iso}}\, \dot{\alpha}_{\mathrm{iso}} + \boldsymbol{Q}_{\mathrm{kin}} : \dot{\boldsymbol{\alpha}}_{\mathrm{kin}} + \mathbb{H}_1 :: \dot{\mathbb{E}}_1 + \mathbb{H}_2 :: \dot{\mathbb{E}}_2 \geq 0 \tag{4.35}$$

can be rewritten as

$$\begin{aligned}
\mathcal{D} \quad = \quad & 3\,\lambda\, Q_0^3 + \lambda\, \frac{c_{\mathrm{kin}}}{\tilde{c}_{\mathrm{kin}}}\, \boldsymbol{Q}_{\mathrm{kin}} : \boldsymbol{Q}_{\mathrm{kin}} + \lambda\, \frac{c_{\mathrm{L}i}}{c_{\mathrm{dis}i}} \mathbb{H}_i :: \mathbb{H}_i \\
& + \lambda \left(1 - \frac{c_{\mathrm{kin}}\, Q^{\infty}_{\mathrm{kin}}}{\tilde{c}_{\mathrm{kin}}\, \|\partial_{\boldsymbol{\Sigma}} \phi\|} \right) \boldsymbol{Q}_{\mathrm{kin}} : \partial_{\boldsymbol{\Sigma}} \phi \\
& - \lambda\, \frac{c_{\mathrm{L}i}\ s_{\mathrm{L}i}}{c_{\mathrm{dis}i}}\, \mathbb{H}_i :: \mathbb{I}_{\mathrm{dev}} \\
& - \lambda \frac{\left[c_{\mathrm{D}i}\, s_{\mathrm{D}i} - c_{\mathrm{L}i}\, s_{\mathrm{L}i} + (c_{\mathrm{L}i} - s_{\mathrm{L}i})\, \boldsymbol{N} : \mathbb{H}_i : \boldsymbol{N} \right]}{c_{\mathrm{dis}i}} \mathbb{H}_i \\
& :: (\boldsymbol{N} \otimes \boldsymbol{N}) \geq 0.
\end{aligned} \tag{4.36}$$

Again, the positive homogeneity of degree three of the yield function with respect to isotropic, distortional hardening and the relative stresses has been used (for each of the aforementioned variables independently, see Remark 10). In Eq. (4.36), a summation over i from one to two has to be carried out. Although the first line in Ineq. (4.36) is non-negative, a resulting overall non-negative dissipation can usually not be guaranteed. That was also confirmed by several numerical simulations. Furthermore, since the inequality is highly nonlinear, it cannot be enforced in a straightforward manner during the calibration of the model parameters either.

4.3. The Feigenbaum & Dafalias model and its extensions

4.3.1. Fundamentals

Finally, the fundamentals of the Feigenbaum & Dafalias model are briefly discussed. However and in contrast to the original work of Feigenbaum & Dafalias (2007, 2008); Plesek et al. (2010), a finite strain description in terms Mandel stress is considered here in order to fulfill the principle of material frame indifference automatically.

In line with the Teodosiu and the Levkovitch & Svendsen models, a Hill-type yield function represents the starting point. However, Feigenbaum & Dafalias considered a slightly different version

$$\phi = \bar{\Sigma}_\mathrm{e}^2 - Q_\mathrm{iso}^2, \tag{4.37}$$

with

$$\bar{\Sigma}_\mathrm{e} = \sqrt{(\mathrm{dev}\boldsymbol{\Sigma} - \boldsymbol{Q}_\mathrm{kin}) : \mathbb{H} : (\mathrm{dev}\boldsymbol{\Sigma} - \boldsymbol{Q}_\mathrm{kin})}. \tag{4.38}$$

Accordingly, the first term of the yield function is now positively homogeneous of degree two with respect to the relative stresses $\mathrm{dev}\boldsymbol{\Sigma} - \boldsymbol{Q}_\mathrm{kin}$, whereas it is positively homogeneous of degree one within the original Teodosiu and the Levkovitch & Svendsen models.

Concerning isotropic and kinematic hardening, the Feigenbaum & Dafalias model is also based on Armstrong-Frederick-type evolution equations (or Voce rule). To be more precise the slightly modified equations

$$\dot{Q}_\mathrm{iso} = \lambda\, \kappa_1\, Q_\mathrm{iso}\, (1 - \kappa_2\, Q_\mathrm{iso}), \tag{4.39}$$

and

$$\dot{\boldsymbol{Q}}_\mathrm{kin} = \lambda\, \|\partial_{\boldsymbol{\Sigma}}\phi\|\, a_1\, (\boldsymbol{N} - a_2\, \boldsymbol{Q}_\mathrm{kin}) \tag{4.40}$$

are employed where κ_1, κ_2, a_1 and a_2 are model parameters.

So far, all models show strong similarities. However, the distortion of the yield function is captured differently in Feigenbaum & Dafalias (2007, 2008); Plesek et al. (2010). To be more precise, the major goal pursued in Feigenbaum & Dafalias (2007) was to capture the higher curvature of the yield surface in loading direction and the respective flattening in the opposite direction. This effect is modeled through the projection of the effective current loading direction

$$\boldsymbol{N}_\mathrm{r} = \frac{\mathrm{dev}\boldsymbol{\Sigma} - \boldsymbol{Q}_\mathrm{kin}}{\|\mathrm{dev}\boldsymbol{\Sigma} - \boldsymbol{Q}_\mathrm{kin}\|} \tag{4.41}$$

onto the previous loading direction represented by the back stress. This projection shows some similarities to Eq. (4.10) within the Teodosiu model. Using the aforementioned projection, the fourth-order tensor $\mathbb{H}$ defining the shape of the yield functions is assumed as

$$\mathbb{H} = \mathbb{H}_0 + (\boldsymbol{N}_\mathrm{r} : \boldsymbol{Q}_\mathrm{kin})\, \mathbb{A}, \tag{4.42}$$

where the fourth-order tensor $\mathbb{A}$ is introduced according to

$$\dot{\mathbb{A}} = -\lambda\, A_1\, \|\mathrm{dev}\boldsymbol{\Sigma} - \boldsymbol{Q}_\mathrm{kin}\|^2 \left[(\boldsymbol{N}_\mathrm{r} : \boldsymbol{Q}_\mathrm{kin})\, \boldsymbol{N}_\mathrm{r} \otimes \boldsymbol{N}_\mathrm{r} + \frac{3}{2}\, A_2\, \mathbb{A} \right]. \tag{4.43}$$

Here, A_1 and A_2 are model parameters.

In order to understand the model, the aforementioned projection which describes the curvature difference in the loading and the opposite direction is switched off first by setting $\boldsymbol{N}_\mathrm{r} : \boldsymbol{Q}_\mathrm{kin} = 1$. In this case, Eqs. (4.42, 4.43) can be simplified to

$$\dot{\mathbb{H}} = -\lambda \, A_1 \, \left[(\mathrm{dev}\boldsymbol{\Sigma} - \boldsymbol{Q}_\mathrm{kin}) \otimes (\mathrm{dev}\boldsymbol{\Sigma} - \boldsymbol{Q}_\mathrm{kin}) + \frac{3}{2} \, A_2 \, \|\mathrm{dev}\boldsymbol{\Sigma} - \boldsymbol{Q}_\mathrm{kin}\|^2 \, \mathbb{A} \right]. \tag{4.44}$$

According to Eq. (4.44) and in line with the Levkovitch & Svendsen model (see Eq. (4.29)) and the Teodosiu model (see Eq. (4.14)), distortional hardening is again modeled by an Armstrong-Frederick-type evolution equation. The only slight difference is that the flow direction $\boldsymbol{N}$ is replaced by the "radial" direction $\boldsymbol{N}_\mathrm{r}$ in Eq. (4.44). However, this does not lead to significant differences. Furthermore, all effects are incorporated into only one evolution equation in the Feigenbaum & Dafalias model. In contrast, a decomposition into dynamic and latent parts is considered within the Teodosiu as well as within the Levkovitch & Svendsen model.

Having discussed the special situation $\boldsymbol{N}_\mathrm{r} : \boldsymbol{Q}_\mathrm{kin} = 1$, focus is now on the general case. Conceptually, distortional hardening is still modeled by an Armstrong-Frederick-type evolution equation then. However, according to the factor $\boldsymbol{N}_\mathrm{r} : \boldsymbol{Q}_\mathrm{kin}$ the effective material parameters of this evolution equation can change - even their signs. This precisely yields a higher curvature of the yield function in the loading direction and a flattening in the opposite direction.

In summary, the difference between the Feigenbaum & Dafalias model and the Levkovitch & Svendsen model is the projection factor $\boldsymbol{N}_\mathrm{r} : \boldsymbol{Q}_\mathrm{kin}$. However, this factor does have an important effect on the evolution of the yield function. It is realized by a coupling between kinematic and distortional hardening through which the overall model becomes more complex.

4.3.2. Extensions of the Feigenbaum & Dafalias model for magnesium alloys

Based on the similarities between the original Feigenbaum & Dafalias model and the original Levkovitch & Svendsen model, the extensions necessary for the description of magnesium are also similar. Conceptually, the only significant difference is related to distortional hardening. In this connection, the two fourth-order tensors (4.33) governing the evolution of the CB2004 yield function (4.32) are assumed to be

$$\mathbb{H}_i = \mathbb{H}_{0i} + (\boldsymbol{N}_\mathrm{r} : \boldsymbol{Q}_\mathrm{kin})\, \mathbb{A}_i \qquad i \in \{1; 2\}. \tag{4.45}$$

Both fourth-order tensors $\mathbb{A}_i$ are independently governed by equation (4.43), i.e.

$$\dot{\mathbb{A}}_i = -\lambda A_{1i} \|\mathrm{dev}\boldsymbol{\Sigma} - \boldsymbol{Q}_\mathrm{kin}\|^2 \left[(\boldsymbol{N}_\mathrm{r} : \boldsymbol{Q}_\mathrm{kin})\, \boldsymbol{N}_\mathrm{r} \otimes \boldsymbol{N}_\mathrm{r} + \frac{3}{2} A_{2i} \mathbb{A}_i \right]. \tag{4.46}$$

4.3.3. Thermodynamical consistency

The Feigenbaum & Dafalias model is the only one of the distortional hardening approaches which has been derived from thermodynamical principles. Therefore, its original form fulfills the dissipation inequality within a geometrically linearized setting. However, here the more general case is considered. To be more precise, the extended model with the yield function as proposed in Cazacu & Barlat (2004) and a finite strain hyperelastoplasticity framework is adopted (see Chapter 3).

Following Subsection 4.2.3, the Helmholtz energy is additively decomposed according to

$$\Psi = \Psi^\mathrm{e} + \Psi^\mathrm{p}_\mathrm{iso}(\alpha_\mathrm{iso}) + \Psi^\mathrm{p}_\mathrm{kin}(\boldsymbol{\alpha}_\mathrm{kin}) + \Psi^\mathrm{p}_\mathrm{dis1}(\mathbb{E}_1) + \Psi^\mathrm{p}_\mathrm{dis2}(\mathbb{E}_2) \tag{4.47}$$

with

$$\begin{array}{ll} \Psi^\mathrm{e} = \mathrm{Eq.}\ (3.13) & \Psi^\mathrm{p}_\mathrm{iso} = \mathrm{Eq.}\ (4.18) \\ \Psi^\mathrm{p}_\mathrm{kin} = \mathrm{Eq.}\ (4.19)_1 & \Psi^\mathrm{p}_{\mathrm{dis}i} = \mathrm{Eq.}\ (4.34)_2. \end{array} \tag{4.48}$$

Accordingly, a neo-Hooke model is used for the elastic response, exponential saturation is considered for isotropic hardening, whereas kinematic and distortional hardening are described by quadratic functions. In order to make the notations comparable, the hardening parameters $\tilde{c}_\mathrm{kin}$ and $c_{\mathrm{dis}i}$ are set to

$$\tilde{c}_\mathrm{kin} = a_1 \quad c_{\mathrm{dis}i} = A_{1i}. \tag{4.49}$$

Inserting Eqs. (4.47 to 4.49), the evolution equations for distortional hardening (see Eqs. (4.43, 4.45)), the evolution equation for kinematic hardening (see Eq. (4.40)), an associative evolution equation for isotropic hardening and an associative flow rule into the reduced dissipation inequality (4.35) eventually yields

$$\mathcal{D} \;=\; \lambda \left(3Q_0^3 + a_2 \left\| \frac{\partial \phi}{\partial \boldsymbol{\Sigma}} \right\| \boldsymbol{Q}_\mathrm{kin} : \boldsymbol{Q}_\mathrm{kin} \right) \tag{4.50}$$

$$+\lambda \left\| \boldsymbol{\Sigma} - \boldsymbol{Q}_{\mathrm{kin}} \right\|^2 \left[\underbrace{\left(\boldsymbol{N}_{\mathrm{r}} : \boldsymbol{Q}_{\mathrm{kin}}\right)\left(\boldsymbol{N}_{\mathrm{r}} \otimes \boldsymbol{N}_{\mathrm{r}}\right) :: \mathbb{A}_i}_{=:\, R} + \frac{3}{2} A_{2i} \mathbb{A}_i :: \mathbb{A}_i \right] \geq 0.$$

Again, the positive homogeneity of degree three of the yield function has been applied here and a summation over i from one to two has to be carried out. By comparing Ineq. (4.50) to its counterpart (4.36) of the extended Levkovitch & Svendsen model it can be seen, that the mathematic structure of dissipation Ineq. (4.50) is significantly simpler. That is due to the thermodynamically consistent structure of the original Feigenbaum & Dafalias model. Only the term R in Ineq. (4.50) can change its sign. Consequently, a necessary condition for thermodynamical consistency is $R \geq 0$. However, this condition turned out to be too restrictive for calibrating the model parameters. For this reason, the weaker sufficient condition

$$\left(\boldsymbol{N}_{\mathrm{r}} : \boldsymbol{Q}_{\mathrm{kin}}\right)\left(\boldsymbol{N}_{\mathrm{r}} \otimes \boldsymbol{N}_{\mathrm{r}}\right) :: \mathbb{A}_i + \frac{3}{2} A_{2i} \mathbb{A}_i :: \mathbb{A}_i \geq 0. \tag{4.51}$$

is enforced. With Ineqs. (4.51), a thermodynamically consistent set of material parameters can be determined. However, the enforcement of Ineq. (4.51) is numerically relatively expensive and strictly speaking, this inequality is only checked for a finite number of loading states. Therefore, thermodynamical consistency cannot be guaranteed for arbitrary loading paths.

4.4. Numerical implementation

The novel constitutive models as presented in Subsections 4.1.2, 4.2.2 and 4.3.2 have been implemented by a state-of-the-art return-mapping scheme, cf. Simo (1998); Simo & Hughes (1998). In this connection, the flow rule has been discretized by an exponential mapping, while the remaining evolution equations have been approximated by means of a backward Euler integration. As a consequence, the resulting scheme is fully implicit and first-order accurate. In contrast to the frameworks Feigenbaum (2008); Noman et al. (2010); Haddadi et al. (2006) based on a co-rotated and hypoelastic framework, the implemented hyperelastoplastic algorithmic formulation shows significant advantages from a physical, as well as from a mathematical point of view, see Simo (1998); Simo & Hughes (1998). Further details are omitted here, but will be discussed in Section 6.5.

5. Identification of model parameters

Before the constitutive model is used in a finite element simulation, the material parameters must be calibrated by comparison of numerical results with experimental observations taken from a distinct material. In the present chapter, the implemented algorithm as well as the result of model parameter identification are discussed. The experimental basis and the calibration procedure are demonstrated in Sections 5.1 and 5.2, while the yield surface evolution for the original models and the extended models with calibrated material parameters are discussed in Sections 5.3 and 5.4, which have been taken from Shi & Mosler (2012).

5.1. Experimental basis for parameter calibration

The material under investigation is the magnesium alloy AZ31 in a heat treated condition (AZ31 O-temper) with a thickness of 1.3 mm. The experiments were conducted using flat specimens prepared according to the DIN 50125-H standard. Each specimen has a gage length of 60 mm and a width of 12.5 mm. The specimens are oriented in the rolling direction (RD), 45° and 90° (TD) from RD, as shown in Fig. 5.1. The tests were conducted using a ZWICK® universal testing machine. For deformation measurement, mechanical extensometer and an optical field deformation measuring system (ARAMIS® system) were employed. The detailed experimental setup can be found in Nebebe (2011).

The mechanical responses are obtained from the tensile tests in terms of direction-dependent flow curves and r-values. The flow curves relate the true stress and to the logarithmic plastic strain. The anisotropy of sheets is captured by the r-value, defined as:

$$r = \frac{\varepsilon_{\mathrm{w}}^{\mathrm{p}}}{\varepsilon_{\mathrm{t}}^{\mathrm{p}}}, \tag{5.1}$$

where $\varepsilon_{\mathrm{w}}^{\mathrm{p}}$ and $\varepsilon_{\mathrm{t}}^{\mathrm{p}}$ are the logarithmic plastic strains in the width and thickness direction, respectively. Further details can be found in Nebebe (2011).

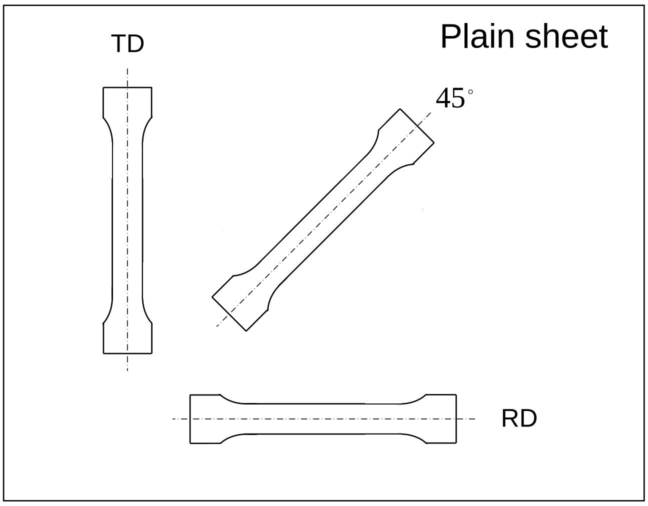

Figure 5.1.: Tensile test specimens geometry

5.2. Procedure for calibration of model parameters

The objective function for the calibration of the model parameters is:

$$\mathcal{F} = \sum_{j=1}^{m} \left[\sum_{i=1}^{n} \left(\frac{\Sigma_i^{\mathrm{sim}} - \Sigma_i^{\mathrm{exp}}}{\Sigma_i^{\mathrm{exp}}} \right)^2 + c_{\mathrm{r}} \left(\frac{r^{\mathrm{sim}} - r^{\mathrm{exp}}}{r^{\mathrm{exp}}} \right)^2 \right]_j , \tag{5.2}$$

where, j is related to the different loading paths, i is the loading step within the considered loading path, Σ^{exp} and r^{exp} are measured stress and r values, Σ^{sim} and r^{sim} are the stress and the r values predicted by the constitutive model and c_{r} is a weight coefficient. It should be mentioned that, for small elastic strains $\boldsymbol{F}^{\mathrm{e}} \to \boldsymbol{I}$, the true stress (σ_y) is equivalent to the corresponding Mandel stress (Σ_y). Therefore, the Mandel stress can be used for the flow curve. Concerning the equivalent plastic strain for the flow curve, the standard definition

$$\dot{\varepsilon}^{\mathrm{p}} = \sqrt{\boldsymbol{L}^{\mathrm{p}} : \boldsymbol{L}^{\mathrm{p}}} \tag{5.3}$$

is employed. Within the computation, the measured plastic strain (equivalent plastic strain) is taken and the stresses are computed. Details of the respective algorithm will be discussed in Subsection 6.5.3.

The underlying mathematical problem of parameter identification is the minimization of the objective function (5.2) depending on the model parameters, i.e., to minimize the difference between measured and computationally predicted mechanical response. It was implemented by a combination of a C++

program and a Scilab program. The scilab code represents a generic minimization algorithm and acts like a driver for the C++ code which, in turn, computes the objective function for a certain set of material parameters. Although the C++ code improves the performance of the overall code significantly, the calibration process is still very time consuming. A further boost of the implementation is realized by running the code on a blade server. For that purpose, the computing load is distributed by message passing interface (MPI). The minimization is done in two steps. In the first of those, an initial set of material parameters is computed. For that purpose, the space of admissible model parameters is discretized by a grid, i.e., the objective function is evaluated for some sets of material parameters. In the second step, the set showing the smallest objective function is used in a deterministic Nelder-Mead algorithm, see Scilab Documentation (2011). In both steps, physical admissibility of the model parameters has to be checked. For that purpose, the following constraints are enforced:

1. Convexity of yield surface, see Remark 4.
2. Second law of thermodynamics, i.e., the dissipation inequality, see Eq. (3.6).

As work hardening stagnation and softening are not the focus of present work, the simplified extended Teodosiu model is considered, refer to Eq. (4.30).

Remark 4 *For further details concerning the convexity constraint of the yield surface and its implementation, the interested reader is referred to Nebebe (2011).*

5.3. Numerical predictions for non-radial loading paths with the original and the extended models

Although the different distortional hardening models have already been discussed in detail in the previous sections, their precise predictive capabilities cannot be estimated in a straightforward manner. That holds particularly for the extended models suitable for the analysis of magnesium. For this reason, three different loading paths are considered in the present section, i.e.

- uniaxial tension
- uniaxial tension followed by reverse loading
- uniaxial loading followed by uniaxial loading into an orthogonal direction.

For these paths, the mechanical response as predicted by the different constitutive models is compared to each other. While in Subsection 5.3.1 the original models are used (reformulated in a hyperelastoplastic framework and a yield surface in terms of Mandel stress in order to guarantee material frame indifference automatically), the extended material models are analyzed in Subsection 5.3.2. For that purpose, the material parameters of the extended models are calibrated for the Mg alloy AZ31.

5.3.1. The original models of Teodosiu, Levkovitch & Svendsen and Feigenbaum & Dafalias

The fundamental characteristics of the different distortional hardening models according to Feigenbaum (2008); Noman et al. (2010); Haddadi et al. (2006) are briefly presented here. Since the model parameters used in the cited references correspond to different materials, the hardening responses predicted by the models can only be qualitatively compared. However, the final extended models analyzed in Subsection 5.3.2 are calibrated for the same material. The parameters of the different hardening models are summarized in Tab. 5.1. Accordingly, an interstitial free mild steel DC06 (1mm) (for the Teodosiu model), the ferritic steel LH800 (for the Levkovitch & Svendsen model) as well as the Al alloy AU4G T4 (for the Feigenbaum & Dafalias model) are the materials under investigation.

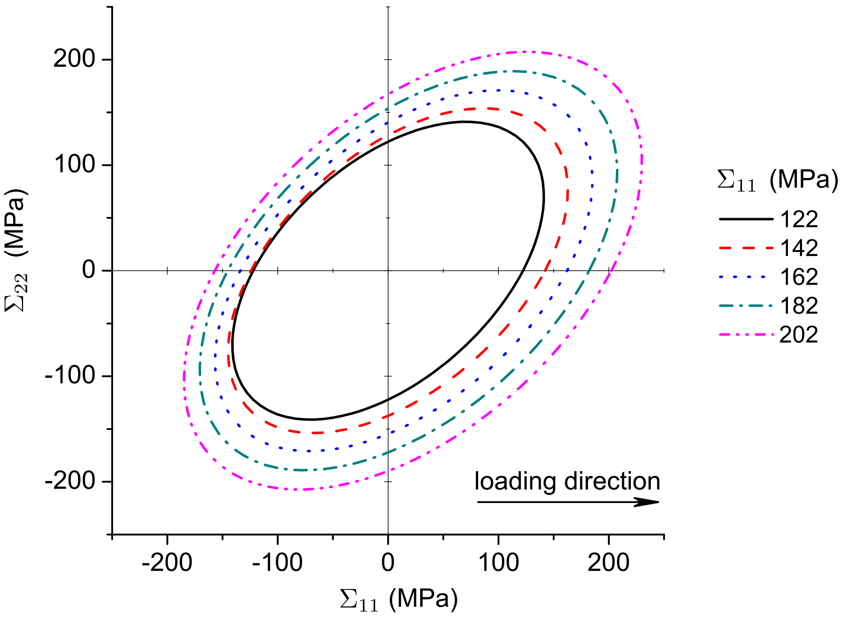

Figure 5.2.: Evolution of the yield surfaces as predicted by the original Teodosiu model for interstitial free mild steel DC06 (1mm), monotonic uniaxial tension test

The Teodosiu model - Interstitial free mild steel DC06 (1mm), cf. Haddadi et al. (2006),Hiwatashi et al. (1998)

Q_0 (MPa)	c_{iso}	Q^{∞}_{iso} (MPa)	c_{kin}	$Q^{(0)}_{\text{kin}}$ (MPa)
122.2	27.3	80.0	614.6	6.9

c_{SD}	c_{SL}	S^{∞} (MPa)	n	n_P	r_{t}	f	c_P	n_{L}
3.9	1.1	246.7	0	27.7	1.9	0.415	2.2	3.0

The Levkovitch & Svendsen model - Ferritic steel LH800, cf. Noman et al. (2010)

Q^{∞}_{iso} (MPa)	c_{iso}	Q^{∞}_{kin} (MPa)	c_{kin}	s_{D}	c_{D}	s_{L}	c_{L}
254.519	4.481	90.896	32.695	0	19.712	-0.863	5.0

The Feigenbaum & Dafalias model - Aluminum alloy AU4G T4 (2024), cf. Feigenbaum & Dafalias (2007)

E (MPa)	ν	Q_0 (MPa)
75000	0.33	205

κ_1	κ_2 (MPa^{-1})	a_1	a_2 (MPa^{-1})	A_1 (MPa^{-4})	A_2 (MPa^2)
$2 \cdot 10^5$	0.004	$2 \cdot 10^6$	0.015	20	2000

Table 5.1.: Model parameters of the original distortional hardening models, taken from literature for various materials, cf. Haddadi et al. (2006); Hiwatashi et al. (1998); Noman et al. (2010); Feigenbaum & Dafalias (2007)

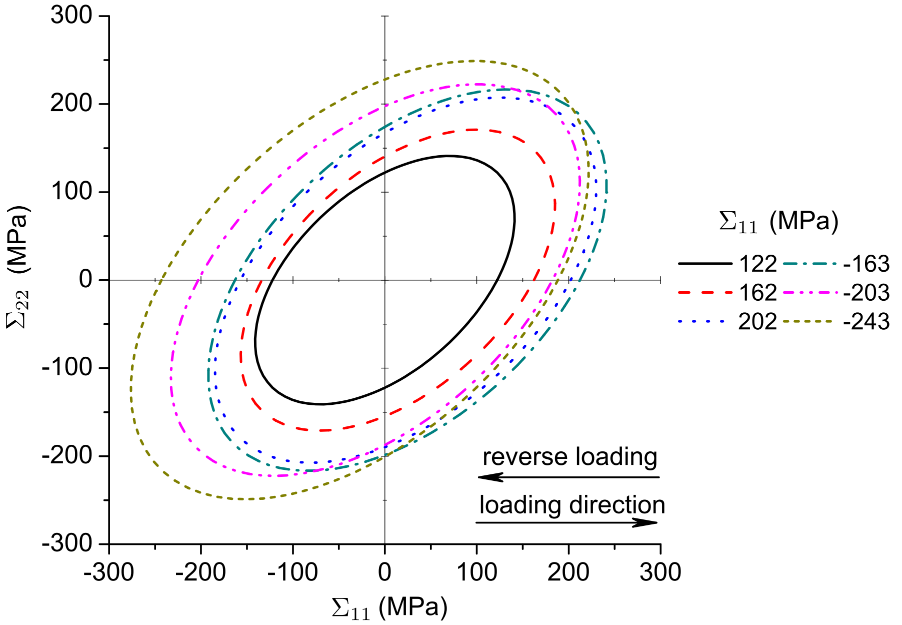

Figure 5.3.: Evolution of the yield surfaces as predicted by the original Teodosiu model for interstitial free mild steel DC06 (1mm), monotonic uniaxial tension test followed by reverse loading (compression)

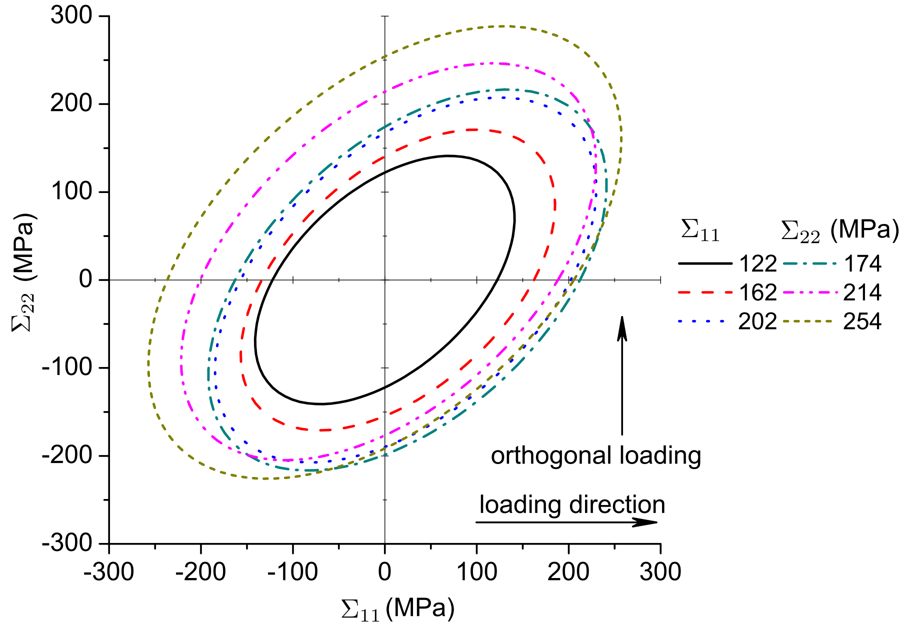

Figure 5.4.: Evolution of the yield surfaces as predicted by the original Teodosiu model for interstitial free mild steel DC06 (1mm), monotonic uniaxial tension test followed by monotonic uniaxial tension into the orthogonal direction

The mechanical responses obtained from the original Teodosiu model are shown in Figs. 5.2 to 5.4 in the form of evolving yield surfaces. Concerning the original Teodosiu model, isotropic hardening is the main hardening mechanism during monotonic loading. If the loading direction is subsequently reversed, see Fig. 5.3, the size of the yield surface increases slowly first (hardening stagnation). After the strain amplitude has reached a certain amplitude, the yield surface increases significantly faster. Similarly, the size of the yield surface changes slowly in the first stage after the loading path change to orthogonal loading. However, kinematic hardening is now more pronounced compared to uniaxial loading. Only when the rate of plastic deformation is again aligned with the current loading direction, isotropic hardening is again the major hardening mechanism. Independently of the loading case, the Teodosiu model cannot predict a distortion of the yield function, since cross hardening is only modeled by modifying isotropic and kinematic hardening.

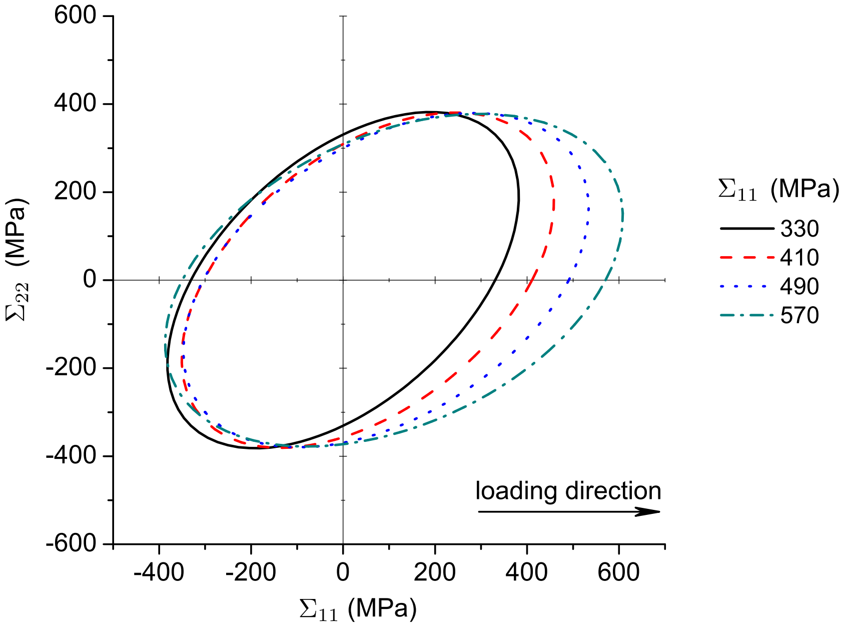

Figure 5.5.: Evolution of the yield surfaces as predicted by the original Levkovitch & Svendsen model for ferritic steel LH800, monotonic uniaxial tension test

The evolution of yield surfaces predicted by the original Levkovitch & Svendsen model is shown in Figs. 5.5 to 5.7. For monotonic loading, the yield function becomes distorted with a preferred elongation in the loading direction. Since the largest diameter of the initial yield surface is associated with a stress state of the type $\Sigma_{11} = \Sigma_{22}$, the elongation along Σ_{11} during deformation leads to a rotation of the yield surface's principal axes. While the yield surface's diameter increases significantly in the loading direction, a small decrease in the

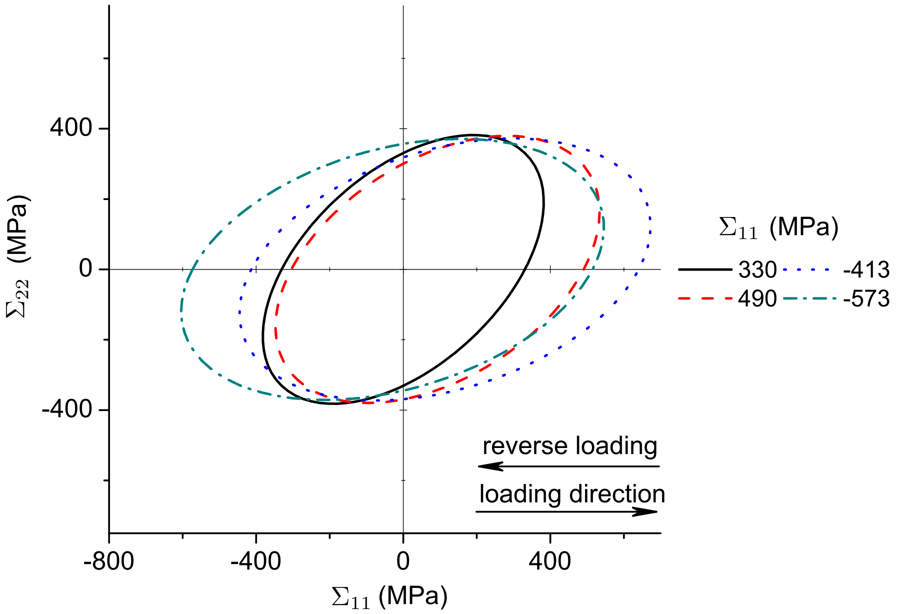

Figure 5.6.: Evolution of the yield surfaces as predicted by the original Levkovitch & Svendsen model for ferritic steel LH800, monotonic uniaxial tension test followed by reverse loading (compression)

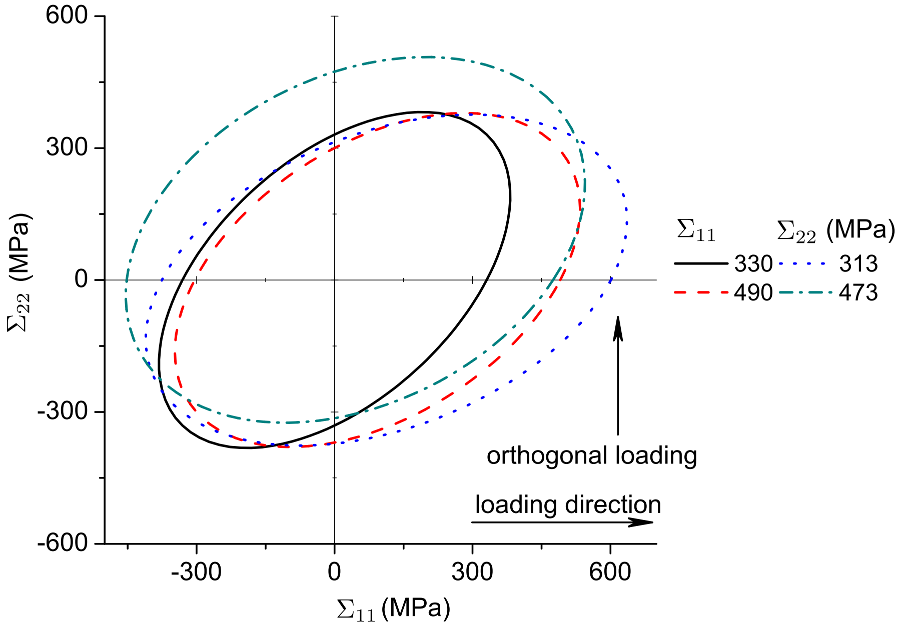

Figure 5.7.: Evolution of the yield surfaces as predicted by the original Levkovitch & Svendsen model for ferritic steel LH800, monotonic uniaxial tension test followed by monotonic uniaxial tension into the orthogonal direction

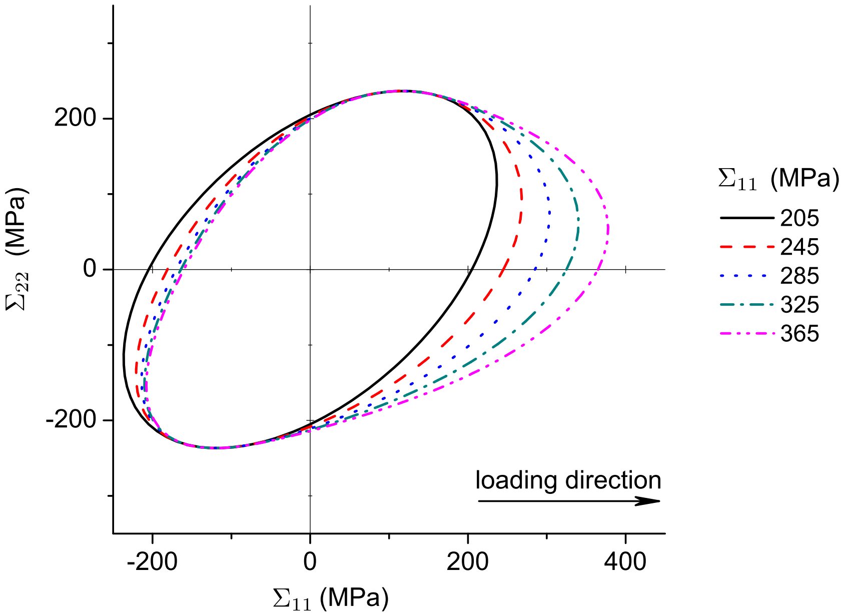

Figure 5.8.: Evolution of the yield surfaces as predicted by the original Feigenbaum & Dafalias model for Al alloy AU4G T4 (2024), monotonic uniaxial tension test

orthogonal direction is also seen. The effects observed in the case of uniaxial tension are also present for reverse loading and orthogonal loading. In sharp contrast to the Teodosiu model, the original Levkovitch & Svendsen model captures the cross hardening effect by a distortion of the yield surface.

Finally, the predictions obtained from the Feigenbaum & Dafalias are analyzed, see Figs. 5.8 to 5.10. As expected, by coupling the kinematic and distortional hardening, the yield surface shows a high curvature in the loading direction, whereas it is rather flat in the opposite direction. This effects can be seen for all loadings paths.

5.3.2. The extended models calibrated for the Mg alloy AZ31

Next, the extended distortional hardening models as discussed in Subsections 4.1.2, 4.2.2, 4.3.2 are applied to the modeling of magnesium. The respective model parameters used to capture the mechanical response of the Mg alloy AZ31 are summarized in Appendix A. They have been identified by the algorithm discussed in Section 5.2. In this connection, loading in three different directions (rolling (RD), transversal (TD) and 45°) has been considered and the numerical predictions have been compared to experimental measurements, cf. Fig. 5.11. Additionally, the r-value at a strain amplitude of 5% was also

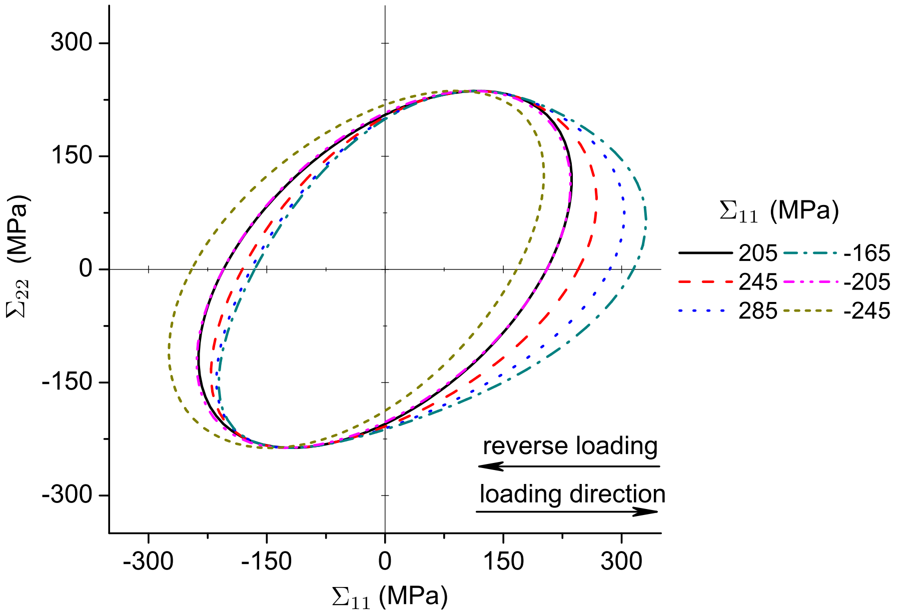

Figure 5.9.: Evolution of the yield surfaces as predicted by the original Feigenbaum & Dafalias model for Al alloy AU4G T4 (2024), monotonic uniaxial tension test followed by reverse loading (compression)

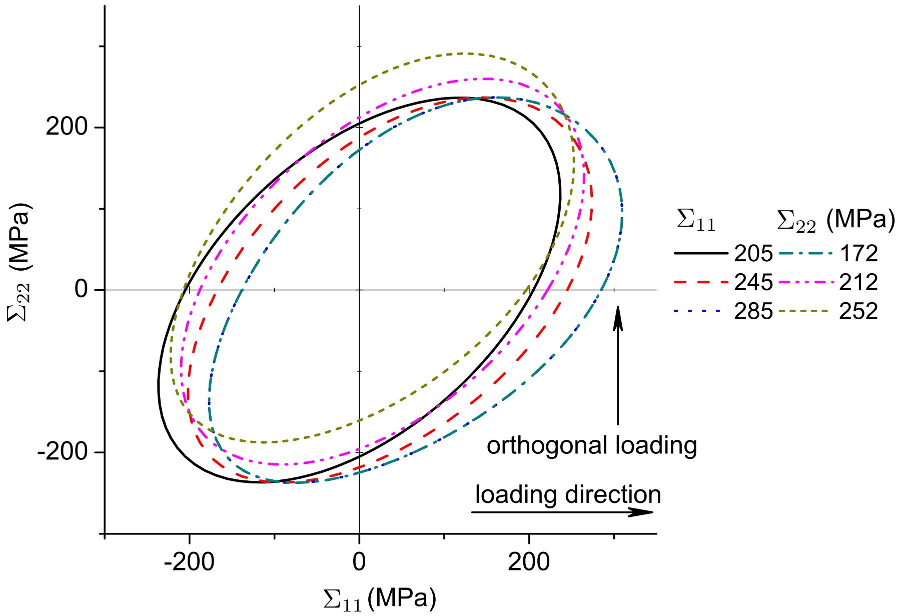

Figure 5.10.: Evolution of the yield surfaces as predicted by the original Feigenbaum & Dafalias model for Al alloy AU4G T4 (2024), monotonic uniaxial tension test followed by monotonic uniaxial tension into the orthogonal direction

included in the least square fit. The respective experimental data have been taken from Mekonen et al. (2012). It has to be mentioned that the measurements considered are not sufficient to identify the model parameters uniquely. For that purpose, additional experiments like the measurements of Mg alloys yield surfaces under non-radial loadings, which have not yet been conducted, are required. Therefore, the predicted evolutions of the yield functions have to be taken with care.

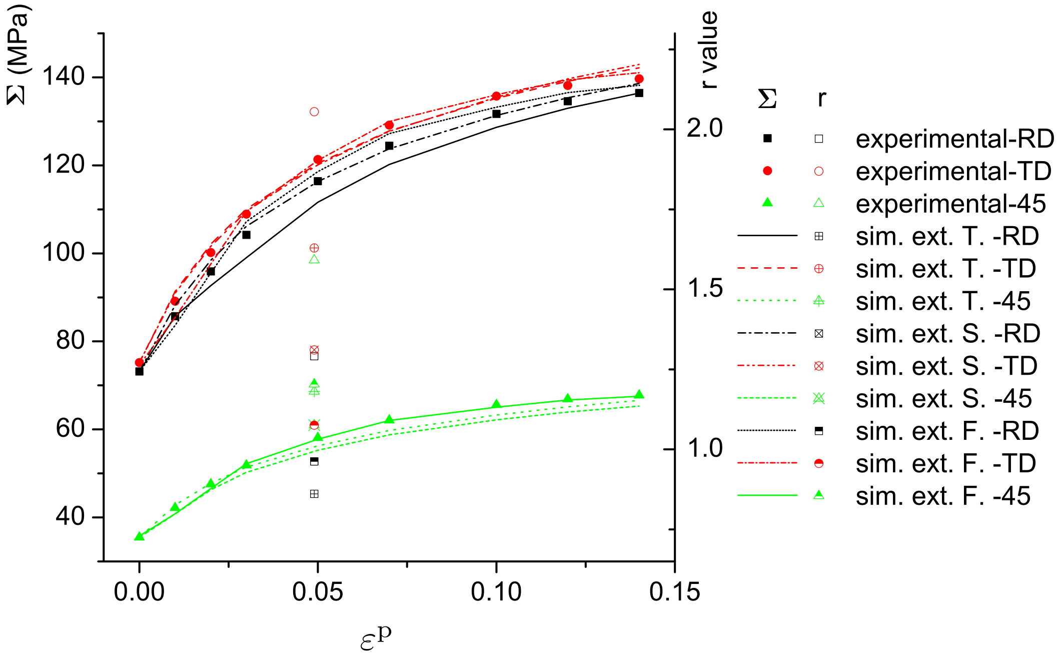

Figure 5.11.: Flow curves and r values for AZ31. Comparison between experiments and predictions by the extended models. Abbreviations: sim.=simulation; ext.=extended; T.=Teodosiu; S.=Levkovitch & Svendsen; F.=Feigenbaum & Dafalias, cf. Subsections 4.1.2, 4.2.2, 4.3.2, 5.3.2

The predictions of the extended distortional hardening models are shown in Figs. 5.12 to 5.20. In line with the previous subsection and due to the structure of the underlying equations, the yield function's shape of the extended Teodosiu model does not change, cf. Figs. 5.12 to 5.14.

Distortion is predicted by the extended Levkovitch & Svendsen model, cf. Figs. 5.15 to 5.17. As already shown in Figs. 5.5 to 5.7, a reorientation of the yield function in the loading direction can be seen. However, this effect is less pronounced for the Mg alloy AZ31 compared to the ferritic steel LH800.

While the mechanical response associated with the extended Teodosiu model and the extended Levkovitch & Svendsen model are in line – at least, qualitatively – with the previous subsection, that is not the case for the extended

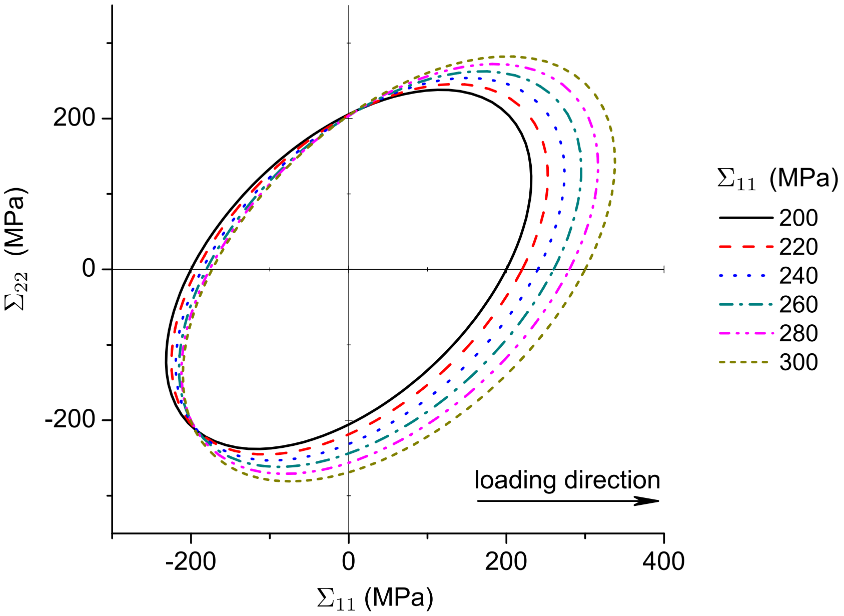

Figure 5.12.: Evolution of the yield surfaces as predicted by the extended Teodosiu model for the Mg alloy AZ31, monotonic uniaxial tension test

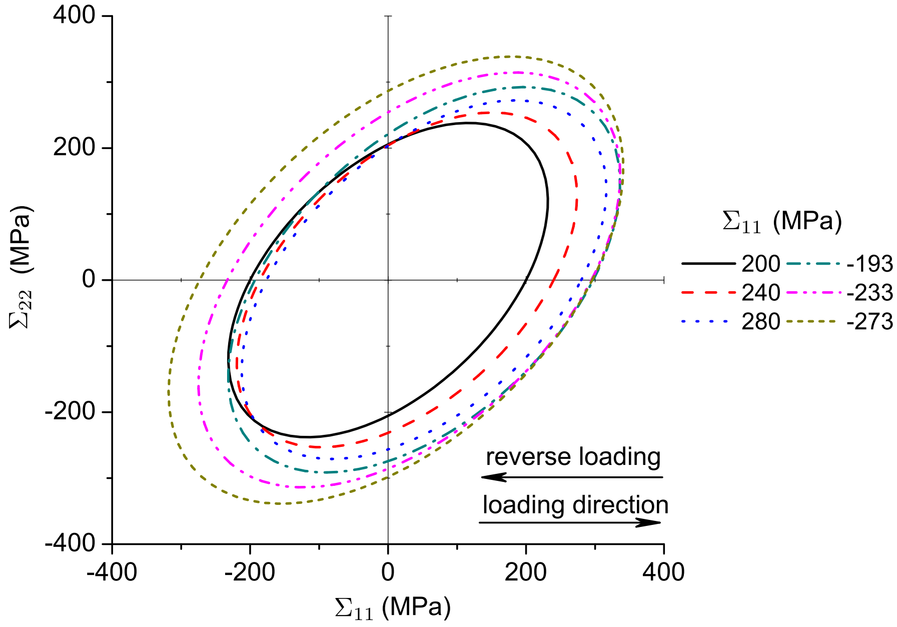

Figure 5.13.: Evolution of the yield surfaces as predicted by the extended Teodosiu model for the Mg alloy AZ31, monotonic uniaxial tension test followed by reverse loading (compression)

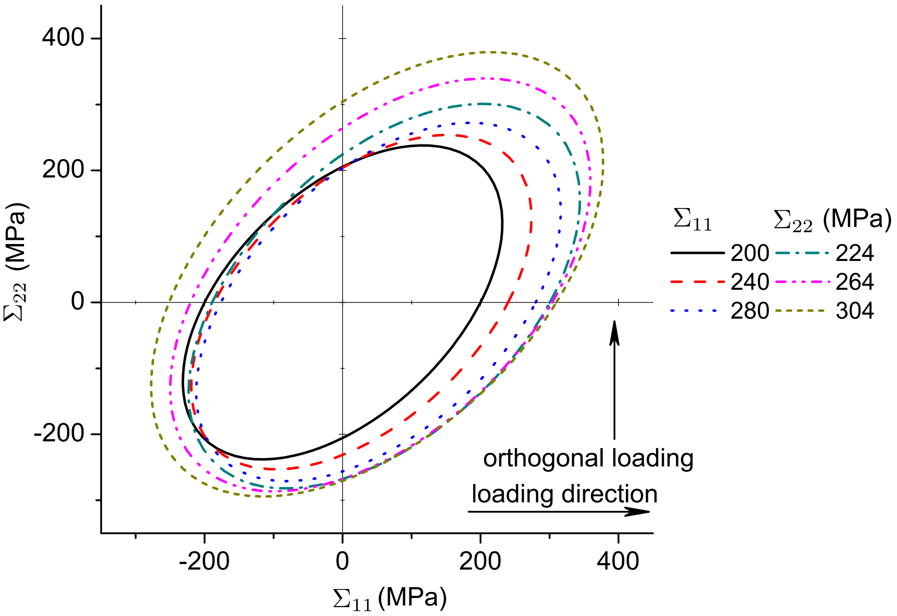

Figure 5.14.: Evolution of the yield surfaces as predicted by the extended Teodosiu model for the Mg alloy AZ31, monotonic uniaxial tension test followed by monotonic uniaxial tension into the orthogonal direction

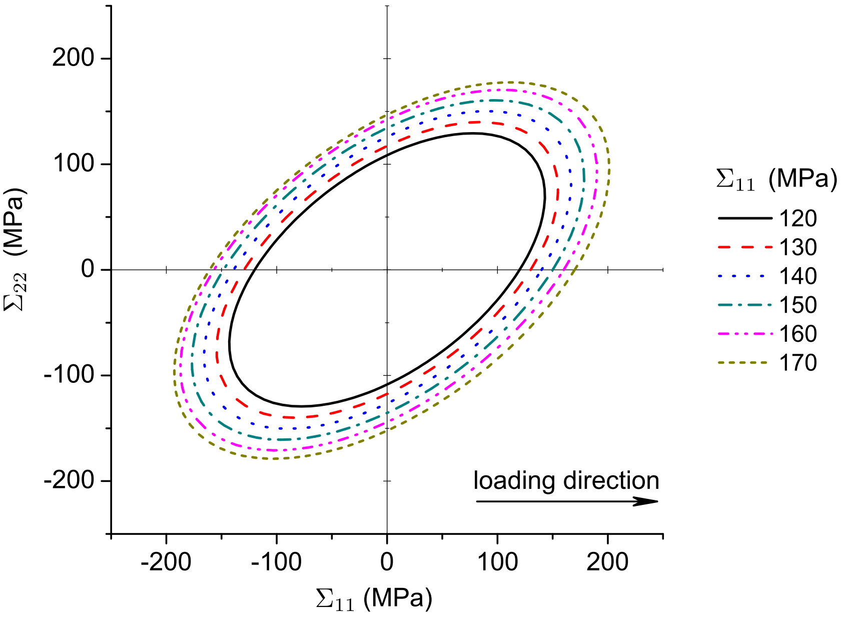

Figure 5.15.: Evolution of the yield surfaces as predicted by the extended Levkovitch & Svendsen model for the Mg alloy AZ31, monotonic uniaxial tension test

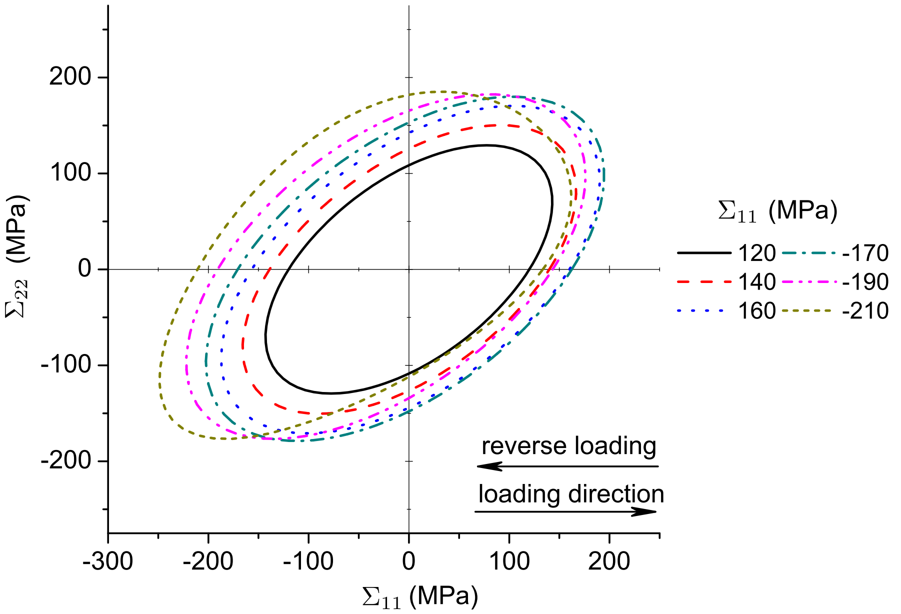

Figure 5.16.: Evolution of the yield surfaces as predicted by the extended Levkovitch & Svendsen model for the Mg alloy AZ31, monotonic uniaxial tension test followed by reverse loading (compression)

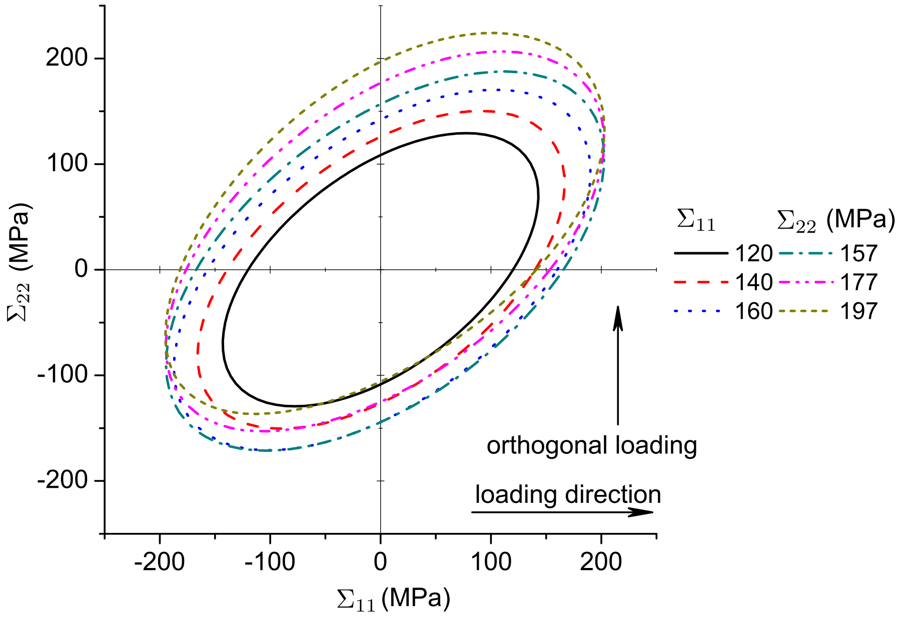

Figure 5.17.: Evolution of the yield surfaces as predicted by the extended Levkovitch & Svendsen model for the Mg alloy AZ31, monotonic uniaxial tension test followed by monotonic uniaxial tension into the orthogonal direction

Feigenbaum & Dafalias model. According to Figs. 5.18 to 5.20, the yield function's curvature is not higher in the loading direction compared to the opposite direction for AZ31. A careful analysis of the underlying model parameters reveals that distortional hardening is virtually not active, e.g., the saturation rate of the distortional hardening tensors A_{1i} is much lower than the one for isotropic hardening κ_1, cf. Tab. A.2.

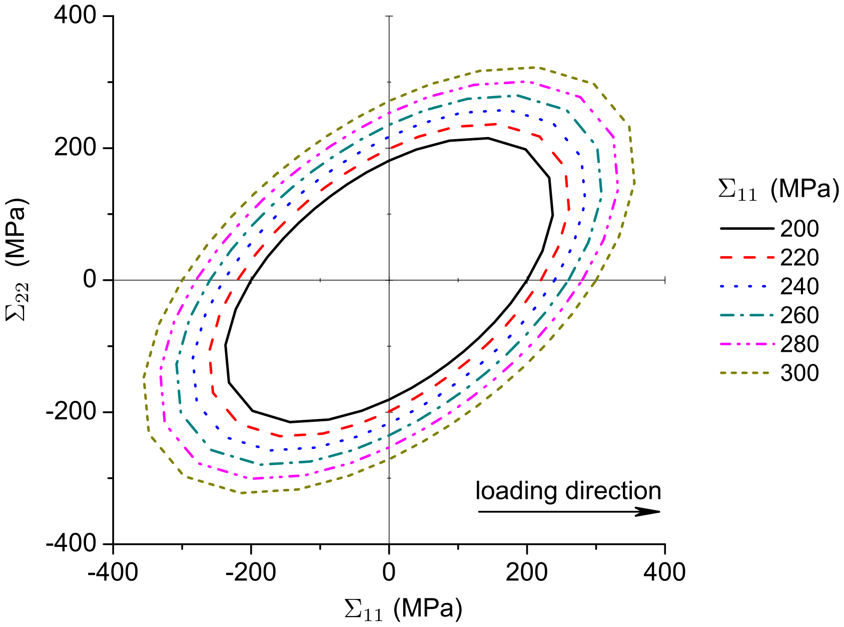

Figure 5.18.: Evolution of the yield surfaces as predicted by the extended Feigenbaum & Dafalias model for the Mg alloy AZ31, monotonic uniaxial tension test

5.4. Discussion

According to the previous section, the extended Teodosiu, Levkovitch & Svendsen and the Feigenbaum & Dafalias models can capture some of the important mechanical effects observed in magnesium alloy sheets, cf. Fig. 5.11. However, in the several optimization trials that have been carried out, an accurate modeling of the stress-strain data together with r values was impossible for the extended models.

Among these models, only the approach originally proposed by Teodosiu and co-workers does not account for a distortion of the yield function, but incorporates cross hardening by modifying isotropic and kinematic hardening. The unique feature of the Teodosiu model is the precise description of work hardening stagnation, softening and resumption. This description requires a

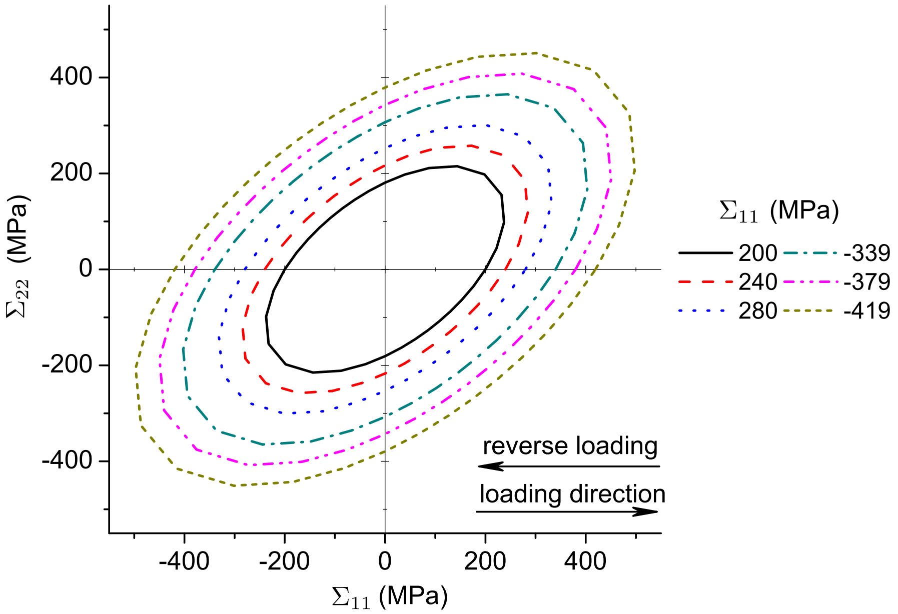

Figure 5.19.: Evolution of the yield surfaces as predicted by the extended Feigenbaum & Dafalias model for the Mg alloy AZ31, monotonic uniaxial tension test followed by reverse loading (compression)

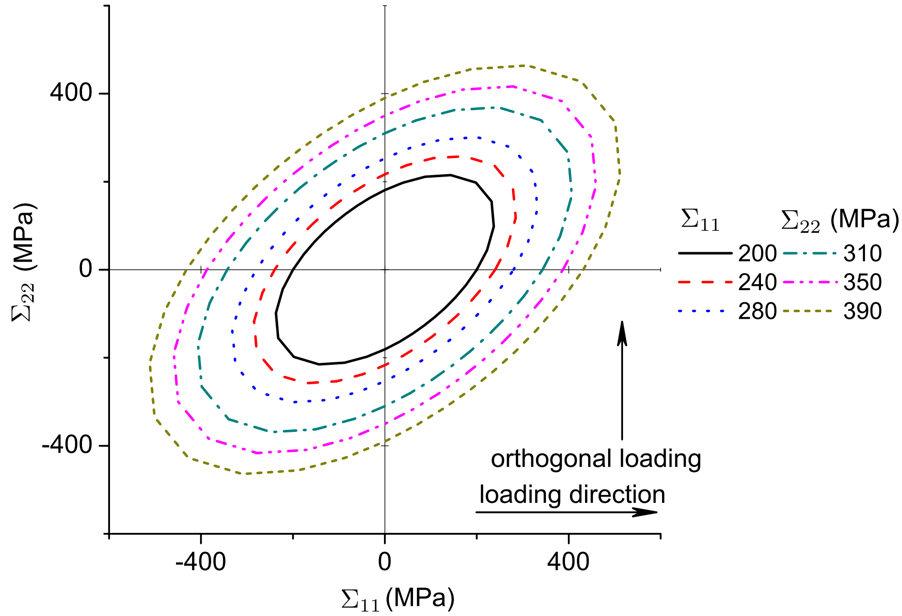

Figure 5.20.: Evolution of the yield surfaces as predicted by the extended Feigenbaum & Dafalias model for the Mg alloy AZ31, monotonic uniaxial tension test followed by monotonic uniaxial tension into the orthogonal direction

significantly larger number of material parameters compared to the extended Levkovitch & Svendsen and Feigenbaum & Dafalias models. Since focus is on the effect of texture evolution in magnesium sheets, the distortion of the yield surface is the major issue, and thus, the extended Teodosiu model will not be considered in the following.

By way of contrast, the extended Levkovitch & Svendsen model does account for a distortion of the yield surface and, since work hardening stagnation, softening and resumption are not described, the modified model requires just four material parameters for the evolution equation of distortional hardening. However, one drawback is the thermodynamical inconsistency of the model, i.e., it does not fulfill the Second Law of thermodynamics.

Although the extended Feigenbaum & Dafalias model does not automatically guarantee the fulfillment of the dissipation inequality either, thermodynamical consistency can be enforced through Ineqs. (4.51). Another positive feature is the small number of material parameters which is particularly appealing within the material parameter identification process. The small number of material parameters is related to the fact that distortional hardening is not decomposed into hardening due to active slip systems and latent slip systems. The only problem associated with the extended Feigenbaum & Dafalias model is that the high curvature of the yield function in the loading direction and the flattening in the opposite direction do not seem to fit the experimental observations for Mg alloys, cf. Plunkett et al. (2006).

In summary, there is a need for a new macroscopic constitutive model that is able to capture the distortion of the yield function due to texture evolution in magnesium alloy sheets. Consequently, a new thermodynamically consistent constitutive model is developed for Mg alloys in the next chapter.

6. A new thermodynamically consistent constitutive model suitable for magnesium alloys

In the present chapter, a new constitutive model for describing distortional hardening in magnesium is elaborated. In contrast to the models discussed in the previous chapters, the new approach is thermodynamically consistent and thus, it fulfills the second law of thermodynamics for arbitrary (positive) model parameters and loading paths. The predictive capabilities of the final model are shown by analyzing the computed mechanical response for different loading paths. Sections 6.1 and 6.2 have been taken from Shi & Mosler (2012).

6.1. Fundamentals

The starting point of the new model is again the CB2004 yield function (3.10). However, in order to normalize the flow rule in advance, the original yield function, which is positively homogeneous of degree three with respect to the relative stresses, is replaced here by its positively homogeneous of degree one counterpart

$$\phi = \left(J_2^{\frac{3}{2}} - J_3 \right)^{\frac{1}{3}} - Q_{\mathrm{iso}} - Q_0. \tag{6.1}$$

Clearly, by setting $\phi = 0$ it can be seen that both functions span essentially the same space of admissible stresses. Similarly to the extended Levkovitch & Svendsen model (see Subsection 4.2.3), all hardening mechanisms are assumed to be uncoupled leading to the Helmholtz energy

$$\Psi = \Psi^{\mathrm{e}} + \Psi^{\mathrm{p}}_{\mathrm{iso}}(\alpha_{\mathrm{iso}}) + \Psi^{\mathrm{p}}_{\mathrm{kin}}(\boldsymbol{\alpha}_{\mathrm{kin}}) + \Psi^{\mathrm{p}}_{\mathrm{dis1}}(\mathbb{E}_1) + \Psi^{\mathrm{p}}_{\mathrm{dis2}}(\mathbb{E}_2). \tag{6.2}$$

In this connection and analogously to the previous models, an isotropic neo-Hooke energy is adopted for the elastic response Ψ^{e}, isotropic hardening Ψ_{iso} is captured by an exponential function and kinematic hardening $\Psi^{\mathrm{p}}_{\mathrm{kin}}$ and distortional hardening $\Psi^{\mathrm{p}}_{\mathrm{dis}i}$ are represented by quadratic functions, i.e.,

$$\Psi^{\mathrm{e}} = \text{Eq. (3.13)} \quad \Psi^{\mathrm{p}}_{\mathrm{iso}} = \text{Eq. (4.18)}$$

$$\Psi^{\mathrm{p}}_{\mathrm{kin}} = \text{Eq. } (4.19)_1 \quad \Psi^{\mathrm{p}}_{\mathrm{dis}i} = \text{Eq. } (4.34)_2. \tag{6.3}$$

The model is completed by suitable evolution equations. Concerning the flow rule, isotropic and kinematic hardening, a convex plastic potential of the type

$$\Omega = \phi + \frac{1}{2}\,\frac{b_{\mathrm{kin}}}{c_{\mathrm{kin}}}\,\boldsymbol{Q}_{\mathrm{kin}} : \boldsymbol{Q}_{\mathrm{kin}} \tag{6.4}$$

is introduced (see Eq. (3.16)) leading to

$$\boldsymbol{L}^{\mathrm{p}} = \lambda \frac{\partial \Omega}{\partial \boldsymbol{\Sigma}} = \lambda \frac{\partial \phi}{\partial \boldsymbol{\Sigma}}, \quad \dot{\alpha}_{\mathrm{iso}} = \lambda\,\frac{\partial \Omega}{\partial Q_{\mathrm{iso}}} = \lambda\,\frac{\partial \phi}{\partial Q_{\mathrm{iso}}} = -\lambda, \quad \dot{\boldsymbol{\alpha}}_{\mathrm{kin}} = \lambda\,\frac{\partial \Omega}{\partial \boldsymbol{Q}_{\mathrm{kin}}}. \tag{6.5}$$

According to Eq. (6.5), an associative flow rule and an associative evolution equation for isotropic hardening are adopted, whereas an Armstrong-Frederick model is used for kinematic hardening.

In order to derive evolution equations for distortional hardening of the type $\dot{\mathbb{H}}_i = \mathbb{F}(\lambda)$, the similarities between the Teodosiu, the Levkovitch & Svendsen and the Feigenbaum & Dafalias model are recalled. Essentially, all such models postulate an Armstrong-Frederick-type evolution equation for the fourth-order tensor related to cross hardening and the distortion of the yield surface. The only differences are that Teodosiu also considered the effects of work hardening stagnation, softening and resumption and Feigenbaum & Dafalias do not decompose the evolution equation into *dynamic* and *latent* parts, cf. Noman et al. (2010). As evident from Eqs. (6.4, 6.5) an Armstrong-Frederick-type evolution equation automatically fulfilling the Second Law of thermodynamics can be designed by means of a plastic potential Ω which contains, in addition to the yield function, a quadratic term. For this reason, distortional hardening can be described by the extended plastic potential

$$\Omega = \phi + \frac{1}{2}\,\frac{b_{\mathrm{kin}}}{c_{\mathrm{kin}}}\,\boldsymbol{Q}_{\mathrm{kin}} : \boldsymbol{Q}_{\mathrm{kin}} + \frac{1}{2}\,\frac{b_{\mathrm{dis1}}}{c_{\mathrm{dis1}}}\,\mathbb{H}_1 :: \mathbb{H}_1 + \frac{1}{2}\,\frac{b_{\mathrm{dis2}}}{c_{\mathrm{dis2}}}\,\mathbb{H}_2 :: \mathbb{H}_2, \tag{6.6}$$

where $c_{\mathrm{dis}i}$ and $b_{\mathrm{dis}i}$ are model parameters. Due to the additive structure of Ω, Eqs. (6.5) are not affected. However, distortional hardening is now consistently included by

$$\dot{\mathbb{E}}_i = \lambda\,\frac{\partial \Omega}{\partial \mathbb{H}_i}, \qquad i \in \{1; 2\}. \tag{6.7}$$

After a lengthy, but nevertheless straightforward calculation, Eqs. (6.7) can be rewritten as

$$\dot{\mathbb{H}}_1 = \lambda\, b_{\mathrm{dis1}}\,\left[-\frac{1}{4}\, b_1\, J_2^{\frac{1}{2}}\,\left((\boldsymbol{\Sigma} - \boldsymbol{Q}_{\mathrm{kin}}) \otimes \boldsymbol{\xi}_1 + \boldsymbol{\xi}_1 \otimes (\boldsymbol{\Sigma} - \boldsymbol{Q}_{\mathrm{kin}}) \right) - \mathbb{H}_1 \right], \tag{6.8}$$

and

$$\dot{\mathbb{H}}_2 = \lambda\, b_{\mathrm{dis2}} \left[\frac{1}{6}\, b_2\ \left((\boldsymbol{\xi}_2 \cdot \boldsymbol{\xi}_2) \otimes (\boldsymbol{\Sigma} - \boldsymbol{Q}_{\mathrm{kin}}) + (\boldsymbol{\Sigma} - \boldsymbol{Q}_{\mathrm{kin}}) \otimes (\boldsymbol{\xi}_2 \cdot \boldsymbol{\xi}_2)\right) - \mathbb{H}_2\right], \tag{6.9}$$

with the abbreviations

$$b_i = \frac{c_{\mathrm{dis}i}}{b_{\mathrm{dis}i}} \left(J_2^{\frac{3}{2}} - J_3\right)^{-\frac{2}{3}}. \tag{6.10}$$

In Eqs. (6.8, 6.9), symmetry of $\mathbb{H}_i$ has been assumed and consistently enforced. Although the structure of Eqs. (6.8) and (6.9) looks relatively complex, convexity of Ω automatically guarantees thermodynamical consistency. In contrast to the extended Feigenbaum & Dafalias models this holds true independently of the chosen material parameters for distortional hardening. By using Eq. (6.6), the dissipation can be conveniently computed in closed form. It eventually results in

$$\begin{aligned}\mathcal{D} = \lambda\Big(& 2\, Q_0 + Q_{\mathrm{iso}} + \frac{b_{\mathrm{kin}}}{c_{\mathrm{kin}}}\, \boldsymbol{Q}_{\mathrm{kin}} : \boldsymbol{Q}_{\mathrm{kin}} \\ &+ \frac{b_{\mathrm{dis1}}}{c_{\mathrm{dis1}}}\, \mathbb{H}_1 :: \mathbb{H}_1 + \frac{b_{\mathrm{dis2}}}{c_{\mathrm{dis2}}}\, \mathbb{H}_2 :: \mathbb{H}_2\Big) \geq 0,\end{aligned} \tag{6.11}$$

where the positive homogeneity of the yield function of degree one with respect to the relative stresses, isotropic hardening and distortional hardening has been considered, refer to Remark 10. Clearly, $\mathcal{D}$ is non-negative.

The new distortional hardening model requires two material parameters ($c_{\mathrm{dis}i}$ and $b_{\mathrm{dis}i}$) for each of the two distortional hardening tensors $\mathbb{H}_i$. The only remaining problem for a model parameter identification is due to the postulated convexity of ϕ, see also Plesek et al. (2010). Within the employed optimization algorithm, a respective constraint has been incorporated (refer to Section 5.2).

Remark 5 *From the structure of the evolution equations for $\mathbb{H}_1$ and $\mathbb{H}_2$, cf. Eqs. (6.8, 6.9), they can be regarded as Armstrong-Frederick type. However, the respective saturation value (tensor) is implicitly a function of $\mathbb{H}_1$ and $\mathbb{H}_2$. Therefore, distortional hardening is only formally identical to an Armstrong-Frederick-rule.*

Remark 6 *In line with the symmetry of the Mandel stresses (in the case of an isotropic elastic model) and a potential description, the fourth-order tensors $\mathbb{H}_i$ are assumed to show minor and major symmetry, i.e.,*

$$\mathbb{H}_{ijkl} = \mathbb{H}_{jikl} = \mathbb{H}_{ijlk} = \mathbb{H}_{klij}.$$

Moreover, the pressure invariance condition

$$\mathbb{H}_{iikl} = 0$$

are also adopted.

6.2. Numerical predictions under non-radial loading paths

As described in Subsection 5.3.2, the parameters of the new model have been calibrated by a standard least square approach including the flow curves for tests along the RD, TD and 45° directions as well as the r-values at strain amplitudes of 5%. The respective results are shown in Fig. 6.1.

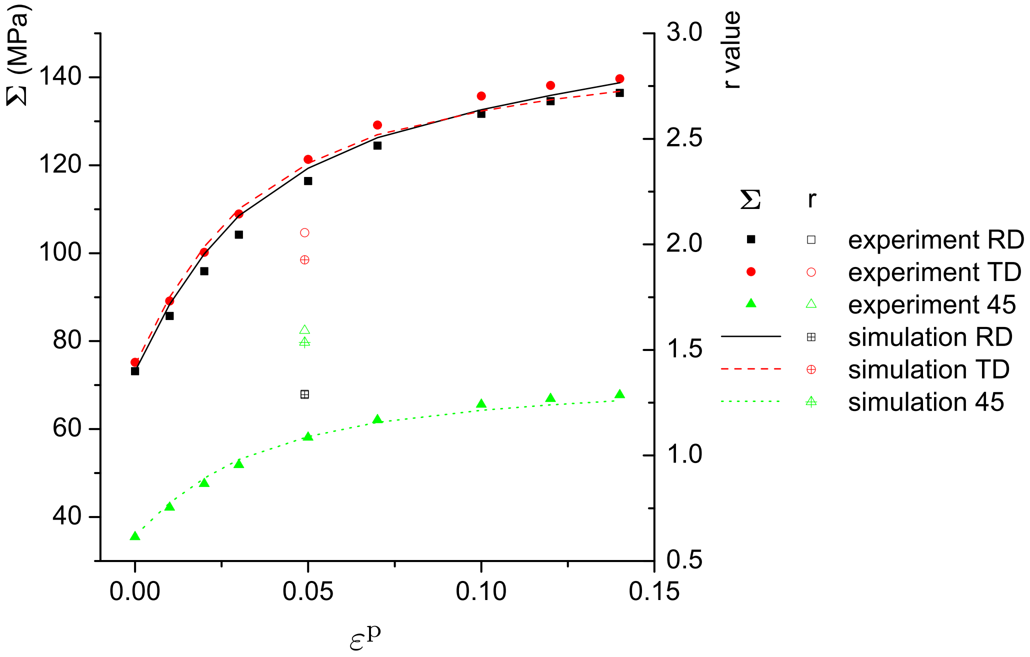

Figure 6.1.: Flow curves for AZ31. Comparison between experiments and predictions by the new model. The r-values at a strain amplitude of 5% are also included in the diagram

Accordingly, the agreement with respect to the flow curves is excellent. The r-values are captured reasonably well compared to the predictions made by other models.

Based on the calibrated model parameters, the evolution of the yield function during reverse loading and orthogonal loading is computed, shown in Figs. 6.2

to 6.4. For the sake of comparison and since the distortion of the yield function is not very high, the results without distortional hardening are also presented, see Figs. 6.2 to 6.4. The model parameters are given in Tab. A.2.

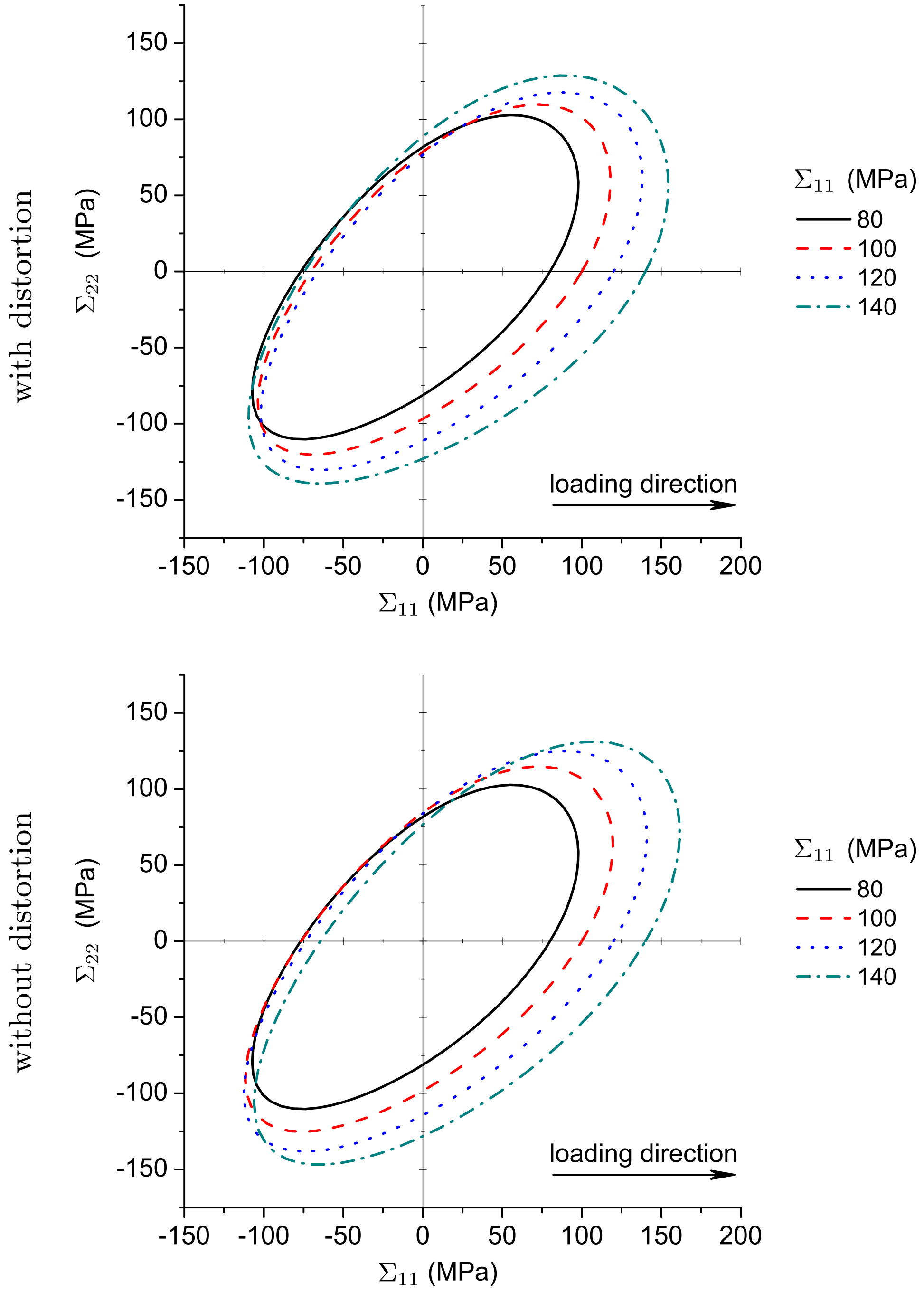

Figure 6.2.: Evolution of the yield surfaces as predicted by the new model for the Mg alloy AZ31. Monotonic uniaxial tension test

The shape change of the yield function can be seen best in the case of the

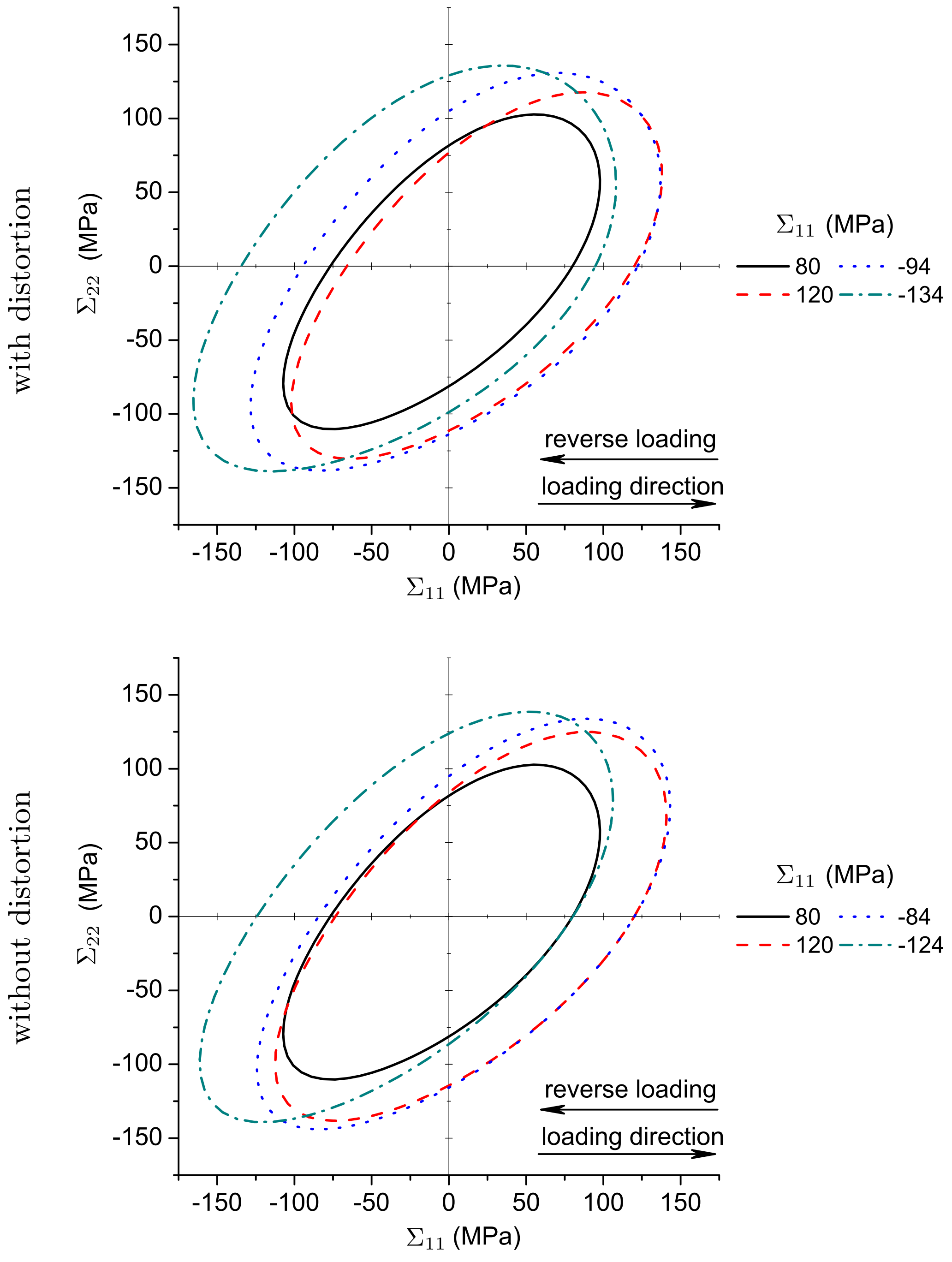

Figure 6.3.: Evolution of the yield surfaces as predicted by the new model for the Mg alloy AZ31. Monotonic uniaxial tension test followed by reverse loading (compression)

orthogonal loading path. In this case, the principal diameter of the yield surface always rotates slightly into the current loading direction, if distortional hardening is taken into account. However, this effect is not very pronounced

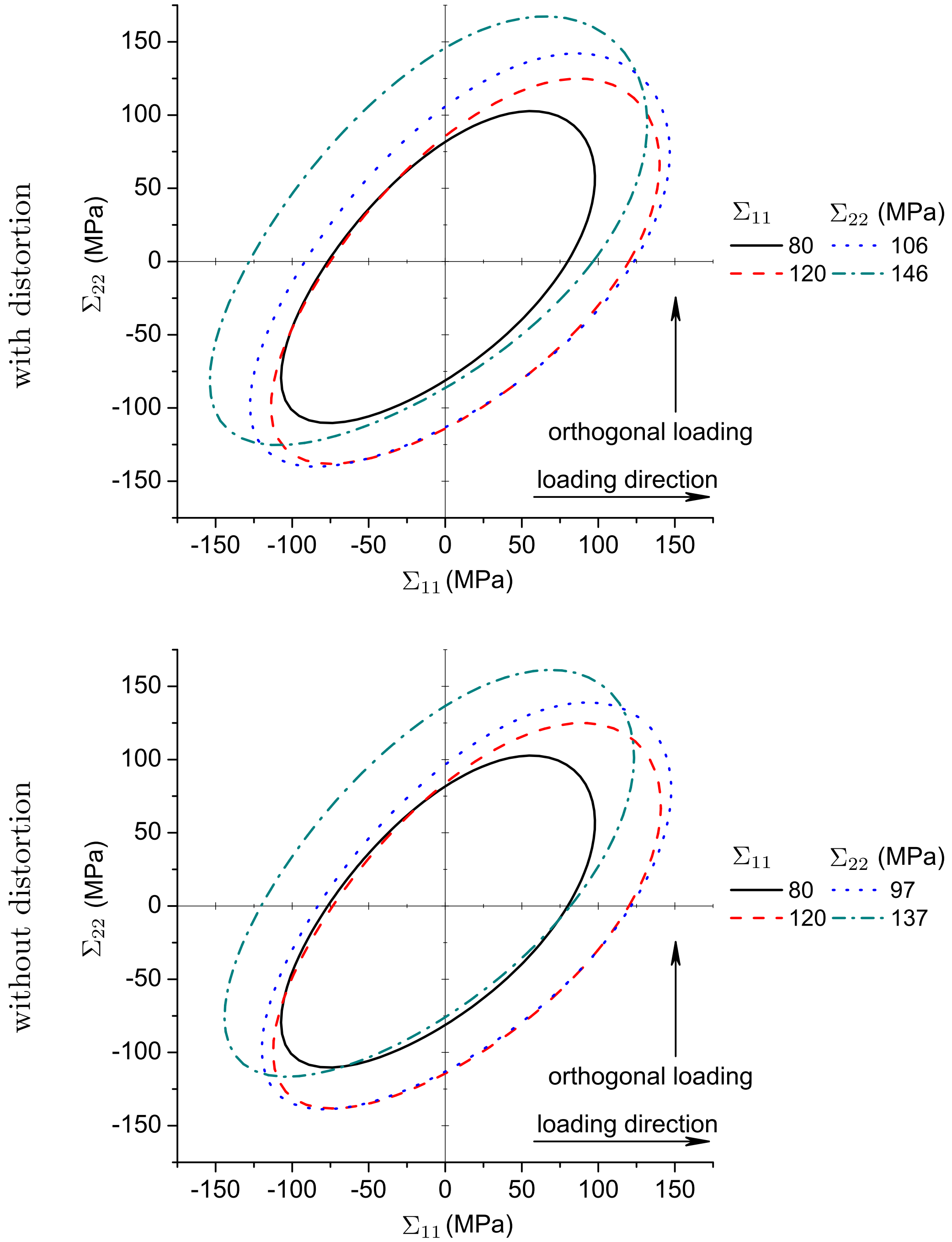

Figure 6.4.: Evolution of the yield surfaces as predicted by the new model for the Mg alloy AZ31. Monotonic uniaxial tension test followed by monotonic uniaxial tension into the orthogonal direction

here. Furthermore, the results have to be interpreted with care due to lack of additional experiments, i.e., yield surface measurements for orthogonal loading are currently not available for AZ31. In any case, the new model does capture the evolution of the yield function by simultaneously fulfilling the Second Law of thermodynamics.

6.3. An alternative derivation of the novel constitutive model

In Section 6.1, the novel model has been derived from a convex plastic potential. Here, a slightly more general derivation is shown. The resulting family of models contains, as a special case, also the model elaborated in Section 6.1. The assumption concerning the Helmholtz energy as well as the yield function are identical to those in Section 6.1 (see Eqs. (6.1,3.11)). However, the explicit existence of a plastic potential is not postulated.

Certainly, the model has to fulfill the second law of thermodynamics. Computing the flow direction

$$\frac{\partial \phi}{\partial \boldsymbol{\Sigma}} = \frac{1}{2} J_2^{\frac{1}{2}} \left(J_2^{\frac{3}{2}} - J_3 \right)^{-\frac{2}{3}} (\boldsymbol{\xi}_1 : \mathbb{H}_1) - \frac{1}{3} \left(J_2^{\frac{3}{2}} - J_3 \right)^{-\frac{2}{3}} (\boldsymbol{\xi}_2 \cdot \boldsymbol{\xi}_2) : \mathbb{H}_2, \quad (6.12)$$

the dissipation inequality

$$\mathcal{D} = \lambda \boldsymbol{\Sigma} : \frac{\partial \phi}{\partial \boldsymbol{\Sigma}} + Q_{\text{iso}} \dot{\alpha}_{\text{iso}} - \frac{1}{C_{\text{kin}}} \boldsymbol{Q}_{\text{kin}} : \dot{\boldsymbol{Q}}_{\text{kin}} - \frac{1}{C_{\text{dis1}}} \mathbb{H}_1 :: \dot{\mathbb{H}}_1 - \frac{1}{C_{\text{dis2}}} \mathbb{H}_2 :: \dot{\mathbb{H}}_2 \quad (6.13)$$

can be rewritten as

$$\begin{aligned} \mathcal{D} \quad = \quad & \lambda \left(\boldsymbol{\Sigma} - \boldsymbol{Q}_{\text{kin}} \right) : \left[\frac{1}{2} J_2^{\frac{1}{2}} \left(J_2^{\frac{3}{2}} - J_3 \right)^{-\frac{2}{3}} (\boldsymbol{\xi}_1 : \mathbb{H}_1) \right. \\ & \left. - \frac{1}{3} \left(J_2^{\frac{3}{2}} - J_3 \right)^{-\frac{2}{3}} (\boldsymbol{\xi}_2 \cdot \boldsymbol{\xi}_2) : \mathbb{H}_2 \right] \\ & + \lambda \boldsymbol{Q}_{\text{kin}} : \frac{\partial \phi}{\partial \boldsymbol{\Sigma}} + Q_{\text{iso}} \dot{\alpha}_{\text{iso}} - \frac{1}{C_{\text{kin}}} \boldsymbol{Q}_{\text{kin}} : \dot{\boldsymbol{Q}}_{\text{kin}} \\ & - \frac{1}{C_{\text{dis1}}} \mathbb{H}_1 :: \dot{\mathbb{H}}_1 - \frac{1}{C_{\text{dis2}}} \mathbb{H}_2 :: \dot{\mathbb{H}}_2. \end{aligned} \quad (6.14)$$

The first two lines in Eq. (6.14) can be significantly simplified. More precisely,

$$\begin{aligned} & \lambda \left(\boldsymbol{\Sigma} - \boldsymbol{Q}_{\text{kin}} \right) : \left[\frac{1}{2} J_2^{\frac{1}{2}} \left(J_2^{\frac{3}{2}} - J_3 \right)^{-\frac{2}{3}} (\boldsymbol{\xi}_1 : \mathbb{H}_1) \right. \\ & \left. - \frac{1}{3} \left(J_2^{\frac{3}{2}} - J_3 \right)^{-\frac{2}{3}} (\boldsymbol{\xi}_2 \cdot \boldsymbol{\xi}_2) : \mathbb{H}_2 \right] \end{aligned}$$

$$\begin{aligned} &= \lambda\left[\frac{1}{2}J_2^{\frac{1}{2}}\left(J_2^{\frac{3}{2}}-J_3\right)^{-\frac{2}{3}}(\boldsymbol{\xi}_1:\boldsymbol{\xi}_1)-\frac{1}{3}\left(J_2^{\frac{3}{2}}-J_3\right)^{-\frac{2}{3}}(\boldsymbol{\xi}_2\cdot\boldsymbol{\xi}_2):\boldsymbol{\xi}_2\right] \\ &= \lambda\left(J_2^{\frac{3}{2}}-J_3\right)^{\frac{1}{3}}, \qquad (6.15)\end{aligned}$$

which is consistent with the Euler theorem for positive homogeneous functions (see Remarks 8, 9). In order to derive physically sound evolution equations, the term (6.15) within the dissipation inequality is decomposed into two parts. A similar approach was also used in Feigenbaum & Dafalias (2007). By introducing a weighting coefficient w (model parameter), Eq. (6.15) is rewritten as

$$\begin{aligned} &\lambda\left(\boldsymbol{\Sigma}-\boldsymbol{Q}_{\mathrm{kin}}\right):\left[\frac{1}{2}J_2^{\frac{1}{2}}\left(J_2^{\frac{3}{2}}-J_3\right)^{-\frac{2}{3}}(\boldsymbol{\xi}_1:\mathbb{H}_1)\right. \\ &\left.-\frac{1}{3}\left(J_2^{\frac{3}{2}}-J_3\right)^{-\frac{2}{3}}(\boldsymbol{\xi}_2\cdot\boldsymbol{\xi}_2):\mathbb{H}_2\right] \\ = \;& w\lambda\left(J_2^{\frac{3}{2}}-J_3\right)^{\frac{1}{3}} \\ &+(1-w)\lambda\left[\frac{1}{2}J_2^{\frac{1}{2}}\left(J_2^{\frac{3}{2}}-J_3\right)^{-\frac{2}{3}}(\boldsymbol{\xi}_1:\boldsymbol{\xi}_1)\right. \\ &\left.-\frac{1}{3}\left(J_2^{\frac{3}{2}}-J_3\right)^{-\frac{2}{3}}(\boldsymbol{\xi}_2\cdot\boldsymbol{\xi}_2):\boldsymbol{\xi}_2\right]. \qquad (6.16)\end{aligned}$$

and the dissipation inequality is restructured accordingly, i.e.,

$$\begin{aligned} \mathcal{D} = \;& w\lambda Q_0 + w\lambda Q_{\mathrm{iso}} + Q_{\mathrm{iso}}\dot{\alpha}_{\mathrm{iso}} \\ &+\lambda\boldsymbol{Q}_{\mathrm{kin}}:\frac{\partial\phi}{\partial\boldsymbol{\Sigma}}-\frac{1}{C_{\mathrm{kin}}}\boldsymbol{Q}_{\mathrm{kin}}:\dot{\boldsymbol{Q}}_{\mathrm{kin}} \\ &+(1-w)\lambda\frac{1}{2}J_2^{\frac{1}{2}}\left(J_2^{\frac{3}{2}}-J_3\right)^{-\frac{2}{3}}(\boldsymbol{\xi}_1:\boldsymbol{\xi}_1)-\frac{1}{C_{\mathrm{dis1}}}\mathbb{H}_1::\dot{\mathbb{H}}_1 \\ &-(1-w)\lambda\frac{1}{3}\left(J_2^{\frac{3}{2}}-J_3\right)^{-\frac{2}{3}}(\boldsymbol{\xi}_2\cdot\boldsymbol{\xi}_2):\boldsymbol{\xi}_2-\frac{1}{C_{\mathrm{dis2}}}\mathbb{H}_2::\dot{\mathbb{H}}_2, \qquad (6.17)\end{aligned}$$

Here $\phi=0$, i.e., $\left(J_2^{\frac{3}{2}}-J_3\right)^{\frac{1}{3}}=Q_0+Q_{\mathrm{iso}}$ was utilized. This form of the dissipation inequality suggests to decompose the dissipation into four parts, each of those being non-negative. The first part is associated with isotropic hardening and the initial size of yield surface, the second part corresponds to kinematic hardening and the third and fourth parts for distortional hardening. By doing so, the second law of thermodynamics would automatically be fulfilled.

Application of the standard associative evolution equation for isotropic hardening

$$\dot{\alpha}_{\mathrm{iso}} = \lambda \frac{\partial \phi}{\partial Q_{\mathrm{iso}}} = -\lambda \tag{6.18}$$

results in

$$w\lambda Q_0 + w\lambda Q_{\mathrm{iso}} + Q_{\mathrm{iso}}\dot{\alpha}_{\mathrm{iso}} = w\lambda Q_0 + w\lambda Q_{\mathrm{iso}} - \lambda Q_{\mathrm{iso}} \geq 0. \tag{6.19}$$

Accordingly, the model parameter w has to fulfill the inequality

$$\frac{Q_{\mathrm{iso}}}{Q_{\mathrm{iso}} + Q_0} \leq w. \tag{6.20}$$

Since again an exponential function is used in order to capture isotropic hardening and furthermore, $\frac{Q_{\mathrm{iso}}}{Q_{\mathrm{iso}}+Q_0}$ is a monotonically increasing function of Q_{iso}, Eq. (6.20) is replaced by

$$\frac{Q^{\infty}_{\mathrm{iso}}}{Q^{\infty}_{\mathrm{iso}} + Q_0} \leq w. \tag{6.21}$$

For the kinematic hardening and distortional hardening parts within the dissipation inequality

$$\boldsymbol{Q}_{\mathrm{kin}} : \left(\lambda \frac{\partial \phi}{\partial \boldsymbol{\Sigma}} - \frac{1}{C_{\mathrm{kin}}} \dot{\boldsymbol{Q}}_{\mathrm{kin}} \right) := \lambda C_{\mathrm{k}} \boldsymbol{Q}_{\mathrm{kin}} : \boldsymbol{Q}_{\mathrm{kin}}, \tag{6.22}$$

$$(1-w)\lambda \frac{1}{2} J_2^{\frac{1}{2}} \left(J_2^{\frac{3}{2}} - J_3 \right)^{-\frac{2}{3}} (\boldsymbol{\xi}_1 : \boldsymbol{\xi}_1) - \frac{1}{C_{\mathrm{dis1}}} \mathbb{H}_1 :: \dot{\mathbb{H}}_1 := \lambda C_{\mathrm{d1}} \mathbb{H}_1 :: \mathbb{H}_1, \tag{6.23}$$

$$-(1-w)\lambda \frac{1}{3} \left(J_2^{\frac{3}{2}} - J_3 \right)^{-\frac{2}{3}} (\boldsymbol{\xi}_2 \cdot \boldsymbol{\xi}_2) : \boldsymbol{\xi}_2 - \frac{1}{C_{\mathrm{dis2}}} \mathbb{H}_2 :: \dot{\mathbb{H}}_2 := \lambda C_{\mathrm{d2}} \mathbb{H}_2 :: \mathbb{H}_2, \tag{6.24}$$

is assumed. By inserting Eqs. (6.22, 6.23, 6.24) into the dissipation inequality, it can be seen that these evolution equations automatically fulfill the second law of thermodynamics, since each of the four terms is non-negative. This underlying idea to use quadratic terms in Eqs. (6.22, 6.23, 6.24) is nowadays standard and can be found in several textbooks, see also Feigenbaum & Dafalias (2007). Eqs. (6.22, 6.23, 6.24) yield the evolution equations

$$\dot{\boldsymbol{Q}}_{\text{kin}} = \lambda C_{\text{kin}} C_{\text{k}} \left(\frac{1}{C_{\text{k}}} \frac{\partial \phi}{\partial \boldsymbol{\Sigma}} - \boldsymbol{Q}_{\text{kin}} \right), \tag{6.25}$$

$$\begin{aligned} \dot{\mathbb{H}}_1 \quad = \quad & \lambda C_{\text{dis1}} \left[(1-w) \frac{1}{4} J_2^{\frac{1}{2}} \left(J_2^{\frac{3}{2}} - J_3 \right)^{-\frac{2}{3}} \big[(\boldsymbol{\Sigma} - \boldsymbol{Q}_{\text{kin}}) \otimes \boldsymbol{\xi}_1 \right. \\ & \left. + \boldsymbol{\xi}_1 \otimes (\boldsymbol{\Sigma} - \boldsymbol{Q}_{\text{kin}}) \big] - C_{\text{d1}} \mathbb{H}_1 \right], \end{aligned} \tag{6.26}$$

$$\begin{aligned} \dot{\mathbb{H}}_2 \quad = \quad & -\lambda C_{\text{dis2}} \left[\frac{(1-w)}{6} \left(J_2^{\frac{3}{2}} - J_3 \right)^{-\frac{2}{3}} \Big[(\boldsymbol{\xi}_2 \cdot \boldsymbol{\xi}_2) \otimes (\boldsymbol{\Sigma} - \boldsymbol{Q}_{\text{kin}}) \right. \\ & \left. + (\boldsymbol{\Sigma} - \boldsymbol{Q}_{\text{kin}}) \otimes (\boldsymbol{\xi}_2 \cdot \boldsymbol{\xi}_2) \Big] + C_{\text{d2}} \mathbb{H}_2 \right]. \end{aligned} \tag{6.27}$$

During material parameter calibration, it was found that the weighting parameter has to fulfill the inequality $1 - w < 0$ in order to yield a mechanical response in line with the experiments. For the admissible choice $w = 2$, the model discussed in the present section is identical to that elaborated in Section 6.1, and now Eq. (6.28) holds. In this respect, the approach based on the weighting coefficient is more general.

$$C_{\text{kin}} := c_{\text{kin}}, \quad C_{\text{k}} := \frac{b_{\text{kin}}}{c_{\text{kin}}}, \quad C_{\text{dis}i} := c_{\text{dis}i}, \quad C_{\text{d}i} := \frac{b_{\text{dis}i}}{c_{\text{dis}i}}, \quad i = 1, 2. \tag{6.28}$$

Remark 7 *It should be emphasized that for all new models elaborated in the present thesis, the distortional hardening part of the plastic free energy is assumed as positive. However, it is negative according to Feigenbaum & Dafalias (2007). Physically, the sign of the distortional hardening part (positive or negative) is determined by the assumption that during distortional hardening part, the plastic free energy is stored or released. It is determined by the microstructure evolution. Accordingly, the structure of the Helmholtz energy proposed in Feigenbaum & Dafalias (2007) is:*

$$\Psi^{\text{p}} = \Psi^{\text{p}}_{\text{iso}} + \Psi^{\text{p}}_{\text{kin}} - \Psi^{\text{p}}_{\text{dis}}. \tag{6.29}$$

However, by changing also the sign of the evolution equations defining distortional, i.e.,

$$\begin{aligned}\dot{\mathbb{H}}_1 &= -\lambda C_{\text{dis1}} C_{\text{d1}} \left(-\frac{1}{4C_{\text{d1}}} J_2^{\frac{1}{2}} \left(J_2^{\frac{3}{2}} - J_3 \right)^{-\frac{2}{3}} \left[(\boldsymbol{\Sigma} - \boldsymbol{Q}_{\text{kin}}) \otimes \boldsymbol{\xi}_1 \right.\right. \\ & \left.\left. + \boldsymbol{\xi}_1 \otimes (\boldsymbol{\Sigma} - \boldsymbol{Q}_{\text{kin}}) \right] - \mathbb{H}_1 \right), \qquad (6.30)\end{aligned}$$

$$\begin{aligned}\dot{\mathbb{H}}_2 &= -\lambda C_{\text{dis2}} C_{\text{d2}} \left(\frac{1}{6C_{\text{d2}}} \left(J_2^{\frac{3}{2}} - J_3 \right)^{-\frac{2}{3}} \left[(\boldsymbol{\xi}_2 \cdot \boldsymbol{\xi}_2) \otimes (\boldsymbol{\Sigma} - \boldsymbol{Q}_{\text{kin}}) \right.\right. \\ & \left.\left. + (\boldsymbol{\Sigma} - \boldsymbol{Q}_{\text{kin}}) \otimes (\boldsymbol{\xi}_2 \cdot \boldsymbol{\xi}_2) \right] - \mathbb{H}_2 \right), \qquad (6.31)\end{aligned}$$

both assumptions are equivalent.

Remark 8 *Positively homogeneous function of degree k*

$\forall\, k \in \mathbb{R}$, a function $f : \mathbb{R}^n \to \mathbb{R}$ is positively homogeneous of degree k if

$$f(\lambda \boldsymbol{x}) = \lambda^k f(\boldsymbol{x}),$$

for all $\lambda > 0$ and $\boldsymbol{x} \in \mathbb{R}^n$.

Remark 9 *Euler's theorem*

For a function $f : \mathbb{R}^n \to \mathbb{R}$ which is positively homogeneous of degree k, the identity

$$\boldsymbol{x} \cdot \nabla f(\boldsymbol{x}) = k f(\boldsymbol{x})$$

is fulfilled.

Remark 10 *The yield function defined in the extended models, cf. Eqs. (4.12, 4.32), shows the following properties:*

- $J_2^{\frac{3}{2}} - J_3$ *is positively homogeneous of degree 3 with respect to* $\boldsymbol{\Sigma}, \boldsymbol{Q}_{\text{kin}}$*;*
- $J_2^{\frac{3}{2}} - J_3$ *is positively homogeneous of degree 3 with respect to* $\mathbb{H}_1, \mathbb{H}_2$*;*
- $J_2^{\frac{3}{2}} - J_3$ *is positively homogeneous of degree 6 with respect to* $\boldsymbol{\Sigma}, \boldsymbol{Q}_{\text{kin}}, \mathbb{H}_1, \mathbb{H}_2$*;*

The yield function of the new model, cf. Eq. (6.1), is based on the equivalent stress

$$\bar{\Sigma}_{\mathrm{e}} := \left(J_2^{\frac{3}{2}} - J_3\right)^{\frac{1}{3}}.$$

It is positively homogeneous of degree 1 with respect to $\boldsymbol{\Sigma}, \boldsymbol{Q}_{\mathrm{kin}}$.

6.4. Variational consistency of the new plasticity model

The new model (see Section 6.1 or Section 6.3 for $w = 2$) does not only fulfill the Second Law of thermodynamics, it also shows a variational structure, cf. Mosler (2007); Mosler & Bruhns (2009, 2010); Mosler (2010). To be more precise, the model can be rewritten as a minimization problem which naturally defines the evolution equations. From a physics point of view, the evolution of the internal variables can thus be interpreted as stable energy minimizers.

6.4.1. Fundamentals

In the present section, the variational structure of finite strain plasticity theory is briefly discussed. It is strongly related to the framework of standard dissipative solids. It will be shown that the potential to be minimized is the stress power, cf. Ortiz & Stainier (1999); Carstensen et al. (2002); Mosler (2007); Mosler & Bruhns (2009):

$$\mathfrak{P}(\dot{\boldsymbol{\varphi}}, \dot{\boldsymbol{F}}^{\mathrm{p}}, \dot{\boldsymbol{\alpha}}, \boldsymbol{\Sigma}, \boldsymbol{Q}) = \boldsymbol{P} : \dot{\boldsymbol{F}} = \dot{\Psi}(\dot{\boldsymbol{\varphi}}, \dot{\boldsymbol{F}}^{\mathrm{p}}, \dot{\boldsymbol{\alpha}}) + \mathcal{D}(\dot{\boldsymbol{F}}^{\mathrm{p}}, \dot{\boldsymbol{\alpha}}, \boldsymbol{\Sigma}, \boldsymbol{Q}). \qquad (6.32)$$

Eq. (6.32) is only valid, if the Mandel stress $\boldsymbol{\Sigma}$ and the internal variables $\boldsymbol{Q}$ defining the plastic flow $\boldsymbol{L}^{\mathrm{p}}$ and the strain-like variables $\boldsymbol{\alpha}$, respectively, are admissible. In line with Ortiz & Stainier (1999); Carstensen et al. (2002); Mosler (2007), this constraint can be enforced by introducing the characteristic function of $\mathbb{E}_{\boldsymbol{\Sigma}}$, i.e.,

$$J(\boldsymbol{\Sigma}, \boldsymbol{Q}) := \begin{cases} 0 & \forall (\boldsymbol{\Sigma}, \boldsymbol{Q}) \in \mathbb{E}_{\boldsymbol{\Sigma}} \qquad \text{cf. Eq. (3.8)} \\ \infty & \text{otherwise.} \end{cases} \qquad (6.33)$$

With the definition of $J(\boldsymbol{\Sigma}, \boldsymbol{Q})$, the constrained problem (6.32) is reformulated into the unconstrained counterpart

$$\tilde{\mathcal{E}}(\dot{\boldsymbol{\varphi}}, \dot{\boldsymbol{F}}^{\mathrm{p}}, \dot{\boldsymbol{\alpha}}, \boldsymbol{\Sigma}, \boldsymbol{Q}) = \mathfrak{P}(\dot{\boldsymbol{\varphi}}, \dot{\boldsymbol{F}}^{\mathrm{p}}, \dot{\boldsymbol{\alpha}}, \boldsymbol{\Sigma}, \boldsymbol{Q}) + J(\boldsymbol{\Sigma}, \boldsymbol{Q}). \qquad (6.34)$$

The attractive properties of functional (6.34) become apparent, if the stationarity conditions are computed, i.e.,

$$\begin{aligned} \delta_{(\boldsymbol{\Sigma},\boldsymbol{Q})}\tilde{\mathcal{E}} = \boldsymbol{0} \quad &\Longrightarrow \quad (\boldsymbol{L}^{\mathrm{p}}, \dot{\boldsymbol{\alpha}}) \in \partial J \\ \delta_{(\dot{\boldsymbol{\alpha}})}\tilde{\mathcal{E}} = \boldsymbol{0} \quad &\Longrightarrow \quad \boldsymbol{Q} = -\tfrac{\partial \Psi}{\partial \boldsymbol{\alpha}} \\ \delta_{(\dot{\boldsymbol{F}}^{\mathrm{p}})}\tilde{\mathcal{E}} = \boldsymbol{0} \quad &\Longrightarrow \quad \boldsymbol{\Sigma} = \boldsymbol{F}^{\mathrm{e}T} \cdot \tfrac{\partial \Psi}{\partial \boldsymbol{F}^{\mathrm{e}}} = 2\boldsymbol{C}^{\mathrm{e}} \cdot \tfrac{\partial \Psi}{\partial \boldsymbol{C}^{\mathrm{e}}} \end{aligned} \tag{6.35}$$

Here, ∂J is the subdifferential of J, cf. Rockafellar (1970). According to Eqs. (6.35), the stationarity condition of $\tilde{\mathcal{E}}$ results in the flow rule, the constitutive relation for the internal stress-like variables $\boldsymbol{Q}$ and the constitutive relation for the Mandel stress $\boldsymbol{\Sigma}$, cf. Carstensen et al. (2002); Mosler (2007); Mosler & Bruhns (2009).

So far, a stationarity principle equivalent to associative plasticity theory at finite strain has been introduced. It can be shown that this principle is represented by a saddle point problem (minimization with respect to $(\dot{\boldsymbol{\alpha}}, \dot{\boldsymbol{F}}^{\mathrm{p}})$, maximization with respect to $(\boldsymbol{\Sigma}, \boldsymbol{Q})$), cf. Mosler (2007); Mosler & Bruhns (2009). However, as discussed in Ortiz & Stainier (1999); Carstensen et al. (2002), it is possible to derive a reduced functional whose minimum yields the evolution equations. For that purpose, the dual of J (the dissipation), i.e.,

$$J^*(\bar{\boldsymbol{L}}^{\mathrm{p}}, \dot{\boldsymbol{\alpha}}) = \sup\left\{\boldsymbol{\Sigma} : \bar{\boldsymbol{L}}^{\mathrm{p}} + \boldsymbol{Q} \cdot \dot{\boldsymbol{\alpha}} | (\boldsymbol{\Sigma}, \boldsymbol{Q}) \in \mathbb{E}_{\boldsymbol{\Sigma}}\right\} \tag{6.36}$$

defined by a Legendre transformation is considered. Inserting the reduced dissipation Ineq. (3.6) into the stress power (6.32) and subsequently, into (6.34), together with the Legendre transformation (6.36), yields the reduced counterpart of Eq. (6.34)

$$\mathcal{E}(\dot{\boldsymbol{\varphi}}, \dot{\boldsymbol{F}}^{\mathrm{p}}, \dot{\boldsymbol{\alpha}}) = \dot{\Psi}(\dot{\boldsymbol{\varphi}}, \dot{\boldsymbol{F}}^{\mathrm{p}}, \dot{\boldsymbol{\alpha}}) + J^*(\boldsymbol{L}^{\mathrm{p}}, \dot{\boldsymbol{\alpha}}). \tag{6.37}$$

For admissible stress states and associative evolution equations, J^* is the dissipation, cf. Mosler (2010). It can be shown, that Eq. (6.37) represents a natural minimization principle of finite strain plasticity theory, i.e.

$$\left(\dot{\boldsymbol{F}}^{\mathrm{p}}, \dot{\boldsymbol{\alpha}}\right) = \arg \inf_{\dot{\boldsymbol{F}}^{\mathrm{p}}, \dot{\boldsymbol{\alpha}}} \mathcal{E}\left(\dot{\boldsymbol{\varphi}}, \dot{\boldsymbol{F}}^{\mathrm{p}}, \dot{\boldsymbol{\alpha}}\right). \tag{6.38}$$

Although variational principle (6.38) looks very simple, the nonlinear constraints imposed by the flow rule

$$\dot{\boldsymbol{F}}^{\mathrm{p}} \cdot \boldsymbol{F}^{\mathrm{p}\,-1} = \lambda \frac{\partial \phi}{\partial \boldsymbol{\Sigma}} \tag{6.39}$$

increase the complexity of the minimization principle significantly. An effective method for a priori fulfilling the respective constraints is the introduction of so-called pseudo stresses $\tilde{\boldsymbol{\Sigma}}$, cf. Mosler & Bruhns (2009); Mosler (2010);

Mosler & Bruhns (2010). They are not necessarily identical to their physical counterparts, i.e., $\tilde{\boldsymbol{\Sigma}} \neq \boldsymbol{\xi} := \boldsymbol{\Sigma} - \boldsymbol{Q}_{\text{kin}}$ (cf. Section 6.1), but they result in the same flow direction by definition, i.e., $\partial_{\boldsymbol{\Sigma}}\phi|_{\tilde{\boldsymbol{\Sigma}}} = \partial_{\boldsymbol{\Sigma}}\phi|_{\boldsymbol{\xi}}$. Employing such a parameterization, the functional dependency of the stress power is given by $\mathcal{E} = \mathcal{E}(\dot{\boldsymbol{\varphi}}, \tilde{\boldsymbol{\Sigma}}, \lambda)$. Consequently, in line with Mosler & Bruhns (2009); Mosler (2010); Mosler & Bruhns (2010), it can be shown that all unknown state variables, together with the deformation mapping, follow jointly from minimizing the potential $\mathcal{E}$, i.e.,

$$\left(\tilde{\boldsymbol{\Sigma}}, \lambda\right) = \arg \inf_{\tilde{\boldsymbol{\Sigma}},\lambda} \mathcal{E}\left(\dot{\boldsymbol{\varphi}}, \tilde{\boldsymbol{\Sigma}}, \lambda\right). \tag{6.40}$$

6.4.2. Variational consistency of the novel model

Considering

$$\boldsymbol{\varphi} = \text{const.} \quad \Longrightarrow \quad \dot{\boldsymbol{F}} = \boldsymbol{0} \quad \Longrightarrow \quad \dot{\boldsymbol{F}}^{\text{e}} = -\boldsymbol{F}^{\text{e}} \cdot \boldsymbol{L}^{\text{p}}, \tag{6.41}$$

the stress power can be written as

$$\begin{array}{rcl}
\mathcal{E} & = & \dot{\Psi} + \mathcal{D} \\
 & = & \dfrac{\partial \Psi}{\partial \boldsymbol{F}} : \dot{\boldsymbol{F}} + \dot{\Psi}\big|_{\dot{\boldsymbol{F}}=\boldsymbol{0}} + \mathcal{D} \\
 & = & \dot{\Psi}\big|_{\dot{\boldsymbol{F}}=\boldsymbol{0}} + \mathcal{D} + \boldsymbol{P} : \dot{\boldsymbol{F}} \\
 & = & \dot{\Psi}^{\text{e}}\big|_{\dot{\boldsymbol{F}}=\boldsymbol{0}} + \dot{\Psi}^{\text{p}}\big|_{\dot{\boldsymbol{F}}=\boldsymbol{0}} + \mathcal{D} + \boldsymbol{P} : \dot{\boldsymbol{F}} \\
 & = & -\boldsymbol{\Sigma} : \boldsymbol{L}^{\text{p}} + \left(\dot{\Psi}^{\text{p}}_{\text{iso}}\big|_{\dot{\boldsymbol{F}}=\boldsymbol{0}} + \dot{\Psi}^{\text{p}}_{\text{kin}}\big|_{\dot{\boldsymbol{F}}=\boldsymbol{0}} + \dot{\Psi}^{\text{p}}_{\text{dis}}\big|_{\dot{\boldsymbol{F}}=\boldsymbol{0}} + \mathcal{D}\right) + \boldsymbol{P} : \dot{\boldsymbol{F}} \\
 & = & -\boldsymbol{\Sigma} : \boldsymbol{L}^{\text{p}} + \Bigg(- \lambda Q_{\text{iso}} \dfrac{\partial \Omega}{\partial Q_{\text{iso}}} - \lambda \boldsymbol{Q}_{\text{kin}} : \dfrac{\partial \Omega}{\partial \boldsymbol{Q}_{\text{kin}}} - \lambda \mathbb{H}_1 :: \dfrac{\partial \Omega}{\partial \mathbb{H}_1} \\
 & & -\lambda \mathbb{H}_1 :: \dfrac{\partial \Omega}{\partial \mathbb{H}_1} + \mathcal{D}\Bigg) + \boldsymbol{P} : \dot{\boldsymbol{F}} \\
 & \overset{\phi=0}{=} & -\boldsymbol{\Sigma} : \boldsymbol{L}^{\text{p}} + \Bigg(- \lambda Q_{\text{iso}} \dfrac{\partial \Omega}{\partial Q_{\text{iso}}} - \lambda \boldsymbol{Q}_{\text{kin}} : \dfrac{\partial \Omega}{\partial \boldsymbol{Q}_{\text{kin}}} - \lambda \mathbb{H}_i :: \dfrac{\partial \Omega}{\partial \mathbb{H}_i} \\
 & & +\lambda \left(2\, Q_0 + Q_{\text{iso}} + \dfrac{b_{\text{kin}}}{c_{\text{kin}}}\, \boldsymbol{Q}_{\text{kin}} : \boldsymbol{Q}_{\text{kin}} + \dfrac{b_{\text{dis}i}}{c_{\text{dis}i}}\, \mathbb{H}_i :: \mathbb{H}_i\right)\Bigg) + \boldsymbol{P} : \dot{\boldsymbol{F}} \\
 & = & -\boldsymbol{\Sigma} : \boldsymbol{L}^{\text{p}} + \Bigg(- \lambda Q_{\text{iso}} \dfrac{\partial \phi}{\partial Q_{\text{iso}}} - \lambda \boldsymbol{Q}_{\text{kin}} : \dfrac{\partial \phi}{\partial \boldsymbol{Q}_{\text{kin}}} - \lambda \mathbb{H}_i :: \dfrac{\partial \phi}{\partial \mathbb{H}_i} \\
 & & +\lambda \left(2\, Q_0 + Q_{\text{iso}}\right)\Bigg) + \boldsymbol{P} : \dot{\boldsymbol{F}}
\end{array}$$

$$\begin{aligned}
&\overset{\phi=0}{=} && -\boldsymbol{\Sigma} : \boldsymbol{L}^{\mathrm{p}} + \left(-\lambda Q_{\mathrm{iso}} \frac{\partial \phi}{\partial Q_{\mathrm{iso}}} - \lambda \boldsymbol{Q}_{\mathrm{kin}} : \frac{\partial \phi}{\partial \boldsymbol{Q}_{\mathrm{kin}}} + \lambda Q_0 \right) + \boldsymbol{P} : \dot{\boldsymbol{F}} \\
&= && -\lambda \boldsymbol{\Sigma} : \frac{\partial \phi}{\partial \boldsymbol{\Sigma}} + \left(-\lambda Q_{\mathrm{iso}} \frac{\partial \phi}{\partial Q_{\mathrm{iso}}} - \lambda \boldsymbol{Q}_{\mathrm{kin}} : \frac{\partial \phi}{\partial \boldsymbol{Q}_{\mathrm{kin}}} + \lambda Q_0 \right) + \boldsymbol{P} : \dot{\boldsymbol{F}} \\
&= && -\lambda \left(\left(J_2^{\frac{3}{2}} - J_3 \right)^{\frac{1}{3}} - Q_{\mathrm{iso}} - Q_0 \right) + \boldsymbol{P} : \dot{\boldsymbol{F}} \\
&= && -\lambda\, \phi + \boldsymbol{P} : \dot{\boldsymbol{F}}. \qquad (6.42)
\end{aligned}$$

Certainly, the same results could be derived by considering $\mathcal{E} = \boldsymbol{P} : \dot{\boldsymbol{F}}$ and $\lambda\, \phi = 0$. By inserting the Helmholtz energy (6.2), the definition of the stress-like variables (3.6,6.3), together with the evolutions equations (6.8,6.9), into Eq. (6.42) yields the stationarity condition (energy stability with respect to the plastic multiplier)

$$\begin{aligned}
\delta_\lambda \mathcal{E} &= \left\{ -\boldsymbol{\Sigma} : \frac{\partial \phi}{\partial \boldsymbol{\Sigma}}\Big|_{\tilde{\boldsymbol{\Sigma}}} + \boldsymbol{Q}_{\mathrm{kin}} : \frac{\partial \phi}{\partial \boldsymbol{\Sigma}}\Big|_{\tilde{\boldsymbol{\Sigma}}} - Q_{\mathrm{iso}} \frac{\partial \phi}{\partial Q_{\mathrm{iso}}} + Q_0 \right\} \delta\lambda = 0 \\
\iff & \quad -\phi = 0 \qquad (6.43)
\end{aligned}$$

which thus enforces the stresses to be admissible, i.e., to fulfill the constraint induced by the yield function. Moreover, the stationarity condition with respect to pseudo stress $\tilde{\boldsymbol{\Sigma}}$ leads to

$$\begin{aligned}
\delta_{\tilde{\boldsymbol{\Sigma}}} \mathcal{E} &= \left\{ -\lambda \boldsymbol{\Sigma} : \frac{\partial^2 \phi}{\partial \boldsymbol{\Sigma}^2}\Big|_{\tilde{\boldsymbol{\Sigma}}} + \lambda \boldsymbol{Q}_{\mathrm{kin}} : \frac{\partial^2 \phi}{\partial \boldsymbol{\Sigma}^2}\Big|_{\tilde{\boldsymbol{\Sigma}}} \right\} : \delta \tilde{\boldsymbol{\Sigma}} = \boldsymbol{0} \\
\iff & \quad (\boldsymbol{\Sigma} - \boldsymbol{Q}_{\mathrm{kin}}) : \frac{\partial^2 \phi}{\partial (\boldsymbol{\Sigma} - \boldsymbol{Q}_{\mathrm{kin}})^2}\Big|_{\tilde{\boldsymbol{\Sigma}}} = \boldsymbol{0} \qquad (6.44)
\end{aligned}$$

which is consistent with the flow rule, refer to Remark 11. As a result, variational principle (6.40) is indeed equivalent to the constitutive model elaborated in Section 6.1.

Remark 11 *Based on Remarks 8 to 10*

$$\Sigma_{\mathrm{eq}}(\boldsymbol{\xi}) = \frac{\partial \Sigma_{\mathrm{eq}}}{\partial \boldsymbol{\xi}} : \boldsymbol{\xi}.$$

Therefore,

$$\Sigma_{\mathrm{eq}} = \frac{\partial \Sigma_{\mathrm{eq}}}{\partial \boldsymbol{\xi}} : \boldsymbol{\xi}$$

$$
\begin{aligned}
&= \frac{\partial\left(\frac{\partial \Sigma_{\mathrm{eq}}}{\partial \boldsymbol{\xi}} : \boldsymbol{\xi}\right)}{\partial \boldsymbol{\xi}} : \boldsymbol{\xi} \\
&= \left(\frac{\partial \Sigma_{\mathrm{eq}}}{\partial \boldsymbol{\xi}} + \frac{\partial^2 \Sigma_{\mathrm{eq}}}{\partial \boldsymbol{\xi}^2} : \boldsymbol{\xi}\right) : \boldsymbol{\xi} \\
&= \frac{\partial \Sigma_{\mathrm{eq}}}{\partial \boldsymbol{\xi}} : \boldsymbol{\xi} + \left(\frac{\partial^2 \Sigma_{\mathrm{eq}}}{\partial \boldsymbol{\xi}^2} : \boldsymbol{\xi}\right) : \boldsymbol{\xi} \\
&= \Sigma_{\mathrm{eq}} + \left(\frac{\partial^2 \Sigma_{\mathrm{eq}}}{\partial \boldsymbol{\xi}^2} : \boldsymbol{\xi}\right) : \boldsymbol{\xi}.
\end{aligned}
$$

As a result,

$$
\left(\frac{\partial^2 \Sigma_{\mathrm{eq}}}{\partial \boldsymbol{\xi}^2} : \boldsymbol{\xi}\right) : \boldsymbol{\xi} = 0, \quad \Longrightarrow \quad \frac{\partial^2 \phi}{\partial \boldsymbol{\xi}^2} : \boldsymbol{\xi} = \mathbf{0},
$$

which is equivalent to Eq. (6.44). Consequently, Eq. (6.44) is indeed consistent with the underlying flow direction, i.e., the minimization principle (6.40) naturally enforces the flow direction.

6.5. Numerical implementation based on the return-mapping algorithm

The numerical implementation of the constitutive models discussed in the previous sections is elaborated here. Since all models show a similar structure, a similar algorithm can be applied to all of them. In this connection, a nowadays classical return-mapping algorithm is elaborated. Further details can be found in Simo (1998); Simo & Hughes (1998).

6.5.1. Predictor / corrector algorithm - The return-mapping scheme

6.5.1.1. The predictor step

At the current loading step $n+1$, a purely elastic (trial) step is defined. This so-called trial state is determined solely in terms of the initial conditions $(\boldsymbol{F}^{\mathrm{p}}_n, \boldsymbol{Q}_n)$ together with the current deformation measure $\boldsymbol{F}_{n+1}$. Certainly, this state may not correspond to any actual, physically admissible state, cf. Simo & Hughes (1998). Once the trial state is calculated via Tab. 6.1, the discrete unloading condition

$$
\phi^{\mathrm{trial}}_{n+1} \le 0 \tag{6.45}
$$

- Trial value of the Mandel stress at current loading step $n+1$

$$\boldsymbol{\Sigma}^{\text{trial}}_{n+1} := \boldsymbol{\Sigma}^{\text{trial}}_{n+1}(\boldsymbol{C}^{\text{e}^{\text{trial}}}_{n+1}) = \boldsymbol{\Sigma}^{\text{trial}}_{n+1}(\boldsymbol{F}_{n+1}, \boldsymbol{F}^{\text{p}^{\text{trial}}}_{n+1})$$

with

$$\boldsymbol{F}^{\text{p}^{\text{trial}}}_{n+1} := \boldsymbol{F}^{\text{p}}_{n}, \qquad \boldsymbol{Q}^{\text{trial}}_{n+1} := \boldsymbol{Q}_{n}.$$

- Trial value of the yield function

$$\phi^{\text{trial}}_{n+1} := \phi^{\text{trial}}_{n+1}(\boldsymbol{\Sigma}^{\text{trial}}_{n+1}, \boldsymbol{Q}^{\text{trial}}_{n+1}).$$

Table 6.1.: Definition of the trial state

is checked. If it is fulfilled, the trial step is admissible and thus, it represents the solution, i.e.

$$\begin{aligned} \boldsymbol{F}^{\text{p}}_{n+1} &= \boldsymbol{F}^{\text{p}}_{n}, \\ \boldsymbol{Q}_{n+1} &= \boldsymbol{Q}_{n}, \\ \boldsymbol{\Sigma}_{n+1} &= \boldsymbol{\Sigma}^{\text{trial}}_{n+1}. \end{aligned} \tag{6.46}$$

6.5.1.2. The corrector step

Clearly, if

$$\phi^{\text{trial}}_{n+1} > 0, \tag{6.47}$$

the trial state cannot be a solution to the incremental problem. Thus, $\boldsymbol{F}^{\text{p}}_{n+1}$ and $\boldsymbol{Q}_{n+1}$ are not constant, but have to be updated. For that purpose, the discretized Karush-Kuhn-Tucker conditions

$$\Delta\lambda > 0 \quad \text{and} \quad \Delta\lambda\,\phi_{n+1} = 0 \qquad \Longrightarrow \qquad \phi_{n+1} = 0 \tag{6.48}$$

are considered. Here, $\Delta\lambda := \int\limits_{t_n}^{t_{n+1}} \lambda \, \mathrm{d}t$ is the integrated plastic multiplier. The Karush-Kuhn-Tucker condition is supplemented by the discretized flow rule and the evolution equations. More precisely, based on the implicit backward Euler time integration, the updated internal variables associated with isotropic, kinematic and distortional hardening are given by:

$$Q_{\text{iso}_{n+1}} = Q^{\infty}_{\text{iso}} \left(1 - \exp[-c_{\text{iso}} \alpha_{\text{iso}_{n+1}}]\right), \tag{6.49}$$

$$\boldsymbol{Q}_{\mathrm{kin}_{n+1}} = \frac{\Delta\lambda c_{\mathrm{kin}} \boldsymbol{N} + \boldsymbol{Q}_{\mathrm{kin}_n}}{1 + b_{\mathrm{kin}}\Delta\lambda}, \tag{6.50}$$

$$\begin{aligned} \mathbb{H}_{1_{n+1}} - \mathbb{H}_{1_n} \quad = \quad & \Delta\lambda b_{\mathrm{dis1}} \Bigg(- \frac{c_{\mathrm{dis1}}}{4 b_{\mathrm{dis1}}} J_{2_{n+1}}^{\frac{1}{2}} \left(J_{2_{n+1}}^{\frac{3}{2}} - J_{3_{n+1}} \right)^{-\frac{2}{3}} \\ & \Bigg[\left(\boldsymbol{\Sigma}_{n+1} - \boldsymbol{Q}_{\mathrm{kin}_{n+1}} \right) \otimes \boldsymbol{\xi}_{1_{n+1}} \\ & + \boldsymbol{\xi}_{1_{n+1}} \otimes \left(\boldsymbol{\Sigma}_{n+1} - \boldsymbol{Q}_{\mathrm{kin}_{n+1}} \right) \Bigg] - \mathbb{H}_{1_{n+1}} \Bigg), \end{aligned} \tag{6.51}$$

$$\begin{aligned} \mathbb{H}_{2_{n+1}} - \mathbb{H}_{2_n} \quad = \quad & \Delta\lambda b_{\mathrm{dis2}} \Bigg(\frac{c_{\mathrm{dis2}}}{6 b_{\mathrm{dis2}}} \left(J_{2_{n+1}}^{\frac{3}{2}} - J_{3_{n+1}} \right)^{-\frac{2}{3}} \\ & \Bigg[\left(\boldsymbol{\xi}_{2_{n+1}} \cdot \boldsymbol{\xi}_{2_{n+1}} \right) \otimes \left(\boldsymbol{\Sigma}_{n+1} - \boldsymbol{Q}_{\mathrm{kin}_{n+1}} \right) \\ & + \left(\boldsymbol{\Sigma}_{n+1} - \boldsymbol{Q}_{\mathrm{kin}_{n+1}} \right) \otimes \left(\boldsymbol{\xi}_{2_{n+1}} \cdot \boldsymbol{\xi}_{2_{n+1}} \right) \Bigg] \\ & - \mathbb{H}_{2_{n+1}} \Bigg). \end{aligned} \tag{6.52}$$

Since such a fully implicit time integration would result in a large set of unknowns (distortional hardening is modeled by two fourth-order tensors), the following assumptions are made (explicit-implicit integration):

$$J_{2_{n+1}}(\mathbb{H}_{1_{n+1}}, \boldsymbol{\Sigma}_{n+1}, \boldsymbol{Q}_{\mathrm{kin}_{n+1}}) = J_{2_{n+1}}(\mathbb{H}_{1_n}, \boldsymbol{\Sigma}_{n+1}, \boldsymbol{Q}_{\mathrm{kin}_{n+1}}), \tag{6.53}$$

$$J_{3_{n+1}}(\mathbb{H}_{2_{n+1}}, \boldsymbol{\Sigma}_{n+1}, \boldsymbol{Q}_{\mathrm{kin}_{n+1}}) = J_{3_{n+1}}(\mathbb{H}_{2_n}, \boldsymbol{\Sigma}_{n+1}, \boldsymbol{Q}_{\mathrm{kin}_{n+1}}), \tag{6.54}$$

$$\boldsymbol{\xi}_{1_{n+1}}(\mathbb{H}_{1_{n+1}}, \boldsymbol{\Sigma}_{n+1}, \boldsymbol{Q}_{\mathrm{kin}_{n+1}}) = \boldsymbol{\xi}_{1_{n+1}}(\mathbb{H}_{1_n}, \boldsymbol{\Sigma}_{n+1}, \boldsymbol{Q}_{\mathrm{kin}_{n+1}}), \tag{6.55}$$

$$\boldsymbol{\xi}_{2_{n+1}}(\mathbb{H}_{2_{n+1}}, \boldsymbol{\Sigma}_{n+1}, \boldsymbol{Q}_{\mathrm{kin}_{n+1}}) = \boldsymbol{\xi}_{2_{n+1}}(\mathbb{H}_{2_n}, \boldsymbol{\Sigma}_{n+1}, \boldsymbol{Q}_{\mathrm{kin}_{n+1}}). \tag{6.56}$$

This leads to the effcient update scheme:

$$\mathbb{H}_{1\,n+1} = \frac{\mathbb{H}_{1\,n} - \frac{\Delta\lambda c_{\mathrm{dis1}}}{4} \mathbb{D}_1}{1 + b_{\mathrm{dis1}}\Delta\lambda}, \tag{6.57}$$

with

$$\mathbb{D}_1 := J_{2_{n+1}}^{\frac{1}{2}} \left(J_{2_{n+1}}^{\frac{3}{2}} - J_{3_{n+1}} \right)^{-\frac{2}{3}} \left[\boldsymbol{\xi}_{n+1} \otimes \boldsymbol{\xi}_{1_{n+1}} + \boldsymbol{\xi}_{1_{n+1}} \otimes \boldsymbol{\xi}_{n+1} \right]. \tag{6.58}$$

Similarly,

$$\mathbb{H}_{2\,n+1} = \frac{\mathbb{H}_{2\,n} + \frac{1}{6}\Delta\lambda c_{\text{dis2}} \mathbb{D}_2}{1 + b_{\text{dis2}} \Delta\lambda}, \tag{6.59}$$

with

$$\mathbb{D}_2 := \left(J_{2_{n+1}}^{\frac{3}{2}} - J_{3_{n+1}} \right)^{-\frac{2}{3}} \left[\left(\boldsymbol{\xi}_{2_{n+1}} \cdot \boldsymbol{\xi}_{2_{n+1}} \right) \otimes \boldsymbol{\xi}_{n+1} + \boldsymbol{\xi}_{n+1} \otimes \left(\boldsymbol{\xi}_{2_{n+1}} \cdot \boldsymbol{\xi}_{2_{n+1}} \right) \right]. \tag{6.60}$$

Accordingly, the update of the fourth-order tensors $\mathbb{H}_i$ shows the same structure as the update defining kinematic hardening, compare to Eq. (6.50). Finally, the flow rule

$$\boldsymbol{L}^{\text{p}} = \lambda \frac{\partial \Omega}{\partial \boldsymbol{\Sigma}} \tag{6.61}$$

is approximated by means of an exponential time integration resulting in

$$\boldsymbol{F}^{\text{p}}_{n+1} = \exp\left[\Delta\lambda \boldsymbol{N}_{n+1}\right] \cdot \boldsymbol{F}^{\text{p}}_{n}, \quad \boldsymbol{N}_{n+1} := \left. \frac{\partial \phi}{\partial \boldsymbol{\xi}} \right|_{n+1}. \tag{6.62}$$

In order to update the state variables $\boldsymbol{F}^{\text{p}}_{n+1}$ and $\boldsymbol{Q}_{n+1}$, Eqs. (6.48 to 6.52, 6.62) have to be solved. In line with assumptions (6.53 to 6.56), there are two residuals ($\boldsymbol{R}_1$ and R_2) depending on the two unknown variables $\Delta\lambda$ and $\boldsymbol{N}$,

$$\boldsymbol{R}_1 := \boldsymbol{N}_{n+1} - \left. \frac{\partial \phi}{\partial \boldsymbol{\Sigma}} \right|_{n+1}, \tag{6.63}$$

$$R_2 := \phi|_{n+1}. \tag{6.64}$$

In order to solve the problem $(\boldsymbol{R}_1; R_2) = 0$, the standard Newton method is adopted. Here, the Jacobian matrix is

$$\begin{bmatrix} \frac{\partial \boldsymbol{R}_1}{\partial \boldsymbol{N}} & \frac{\partial \boldsymbol{R}_1}{\partial \Delta\lambda} \\ \frac{\partial R_2}{\partial \boldsymbol{N}} & \frac{\partial R_2}{\partial \Delta\lambda} \end{bmatrix}. \tag{6.65}$$

It is based on the derivatives

$$\frac{\partial^2\phi}{\partial\boldsymbol{\Sigma}\partial\boldsymbol{N}}, \qquad \frac{\partial^2\phi}{\partial\boldsymbol{\Sigma}\partial\Delta\lambda}, \qquad \frac{\partial\phi}{\partial\boldsymbol{N}}, \qquad \frac{\partial\phi}{\partial\Delta\lambda}. \tag{6.66}$$

Focus is first on the flow direction $\frac{\partial\phi}{\partial\boldsymbol{\Sigma}} = \frac{\partial\phi}{\partial\boldsymbol{\xi}}$. A straightforward computation gives

$$\left.\frac{\partial\phi}{\partial\boldsymbol{\xi}}\right|_{n+1} = \left.\frac{\partial\phi}{\partial J_2}\right|_{n+1} \left.\frac{\partial J_2}{\partial\boldsymbol{\xi}}\right|_{n+1} + \left.\frac{\partial\phi}{\partial J_3}\right|_{n+1} \left.\frac{\partial J_3}{\partial\boldsymbol{\xi}}\right|_{n+1}, \tag{6.67}$$

with

$$\left.\frac{\partial J_2}{\partial\boldsymbol{\xi}}\right|_{n+1} = \left.\frac{\partial J_2}{\partial\boldsymbol{\xi}_1}\right|_{n+1} : \left.\frac{\partial\boldsymbol{\xi}_1}{\partial\boldsymbol{\xi}}\right|_{n+1}, \tag{6.68}$$

and

$$\left.\frac{\partial\xi_{1ab}}{\partial\xi_{ij}}\right|_{n+1} = \left.\frac{\partial\left(H_{1abcd}\xi_{cd}\right)}{\partial\xi_{ij}}\right|_{n+1} = H_{1\,n+1\,abij} + \left.\frac{\partial H_{1\,n+1\,abcd}}{\partial\xi_{ij}}\xi_{cd}\right|_{n+1}. \tag{6.69}$$

In order to compute the derivative of the distortional hardening tensors with respect to the relative stresses, the assumptions (6.53 to 6.56) are applied. Therefore, $\frac{\partial\mathbb{H}_{1\,n+1}}{\partial\boldsymbol{\xi}}$ simplifies to

$$\frac{\partial\mathbb{H}_{1\,n+1}}{\partial\boldsymbol{\xi}} = -\frac{\Delta\lambda c_{\mathrm{dis1}}}{4\left(1+\Delta\lambda b_{\mathrm{dis1}}\right)}\left.\frac{\partial\mathbb{D}_1}{\partial\boldsymbol{\xi}}\right|_{n+1}, \tag{6.70}$$

with

$$\begin{aligned}\left.\frac{\partial\mathbb{D}_1}{\partial\boldsymbol{\xi}}\right|_{n+1} = {} & \underbrace{\frac{\partial\left[J_{2_{n+1}}^{\frac{1}{2}}\left(J_{2_{n+1}}^{\frac{3}{2}} - J_{3_{n+1}}\right)^{-\frac{2}{3}}\right]}{\partial\boldsymbol{\xi}}}_{:=\boldsymbol{T}_1}\Big[\boldsymbol{\xi}_{n+1}\otimes\boldsymbol{\xi}_{1_{n+1}} \\ & +\boldsymbol{\xi}_{1_{n+1}}\otimes\boldsymbol{\xi}_{n+1}\Big] + J_{2_{n+1}}^{\frac{1}{2}}\left(J_{2_{n+1}}^{\frac{3}{2}} - J_{3_{n+1}}\right)^{-\frac{2}{3}} \\ & \underbrace{\frac{\partial\left[\boldsymbol{\xi}_{n+1}\otimes\boldsymbol{\xi}_{1_{n+1}} + \boldsymbol{\xi}_{1_{n+1}}\otimes\boldsymbol{\xi}_{n+1}\right]}{\partial\boldsymbol{\xi}}}_{:=\mathbb{T}_2},\end{aligned} \tag{6.71}$$

where $\boldsymbol{T}_1$ and $\mathbb{T}_2$ are given by:

$$T_{1ij} = \left[\frac{1}{2}J_2^{-\frac{1}{2}}\left(J_2^{\frac{3}{2}} - J_3\right)^{-\frac{2}{3}} - J_2\left(J_2^{\frac{3}{2}} - J_3\right)^{-\frac{5}{3}}\right]\mathrm{sym}\left(\xi_{1ab}\right)H_{1abij}$$

$$+\frac{2}{3}J_2^{-\frac{1}{2}}\left(J_2^{3/2}-J_3\right)^{-5/3}$$
$$\left[\frac{2}{3}\,\xi_{2na}\xi_{2am}+\frac{1}{3}(\xi_{2nb}\xi_{2bm})^T\right]H_{2mnij}, \tag{6.72}$$

$$T_{2abcdij}=\delta_{ai}\,\delta_{bj}\,\xi_{1cd}+\xi_{ab}\,H_{1cdij}+\delta_{ci}\,\delta_{dj}\,\xi_{1ab}+\xi_{cd}\,H_{1abij}. \tag{6.73}$$

Here, δ_{ij} is again the Kronecker delta. Following similar lines, $\frac{\partial J_3}{\partial \boldsymbol{\xi}}$ is obtained, and thus, the flow direction (6.67) is calculated.

With Eqs. (6.67 to 6.73), the Hessian (6.65) can finally be computed. The second row of that matrix results in

$$\frac{\partial \phi}{\partial \boldsymbol{N}}=\frac{\partial \phi}{\partial \boldsymbol{\xi}}:\frac{\partial \boldsymbol{\xi}}{\partial \boldsymbol{N}}, \tag{6.74}$$

with

$$\frac{\partial \boldsymbol{\xi}}{\partial \boldsymbol{N}}=\frac{\partial \boldsymbol{\Sigma}}{\partial \boldsymbol{N}}-\frac{\partial \boldsymbol{Q}_{\text{kin}}}{\partial \boldsymbol{N}} \tag{6.75}$$

and

$$\frac{\partial \phi}{\partial \Delta\lambda}=\frac{\partial \phi}{\partial \boldsymbol{\xi}}:\frac{\partial \boldsymbol{\xi}}{\partial \Delta\lambda}+\frac{\partial \phi}{\partial Q_{\text{iso}}}\frac{\partial Q_{\text{iso}}}{\partial \Delta\lambda}+\frac{\partial \phi}{\partial \mathbb{H}_1}::\frac{\partial \mathbb{H}_1}{\partial \Delta\lambda}+\frac{\partial \phi}{\partial \mathbb{H}_2}::\frac{\partial \mathbb{H}_2}{\partial \Delta\lambda}. \tag{6.76}$$

Regarding the first row of the Hessian matrix (6.65), a straightforward computation yields

$$\frac{\partial^2 \phi}{\partial \boldsymbol{\xi}\partial \Delta\lambda}=\underbrace{\frac{\partial^2 \phi}{\partial \boldsymbol{\xi}\partial \boldsymbol{\xi}}}_{:=\mathbb{T}_3}:\frac{\partial \boldsymbol{\xi}}{\partial \Delta\lambda}+\frac{\partial^2 \phi}{\partial \boldsymbol{\xi}\partial \mathbb{H}_1}::\frac{\partial \mathbb{H}_1}{\partial \Delta\lambda}+\frac{\partial^2 \phi}{\partial \boldsymbol{\xi}\partial \mathbb{H}_2}::\frac{\partial \mathbb{H}_2}{\partial \Delta\lambda}, \tag{6.77}$$

where

$$\begin{aligned} T_{3ijmn} \quad = \quad & \frac{\partial^2 \phi}{\partial J_2 \partial \xi_{mn}}\frac{\partial J_2}{\partial \xi_{ij}}+\frac{\partial \phi}{\partial J_2}\frac{\partial^2 J_2}{\partial \xi_{ij}\partial \xi_{mn}} \\ & +\frac{\partial^2 \phi}{\partial J_3 \partial \xi_{mn}}\frac{\partial J_3}{\partial \xi_{ij}}+\frac{\partial \phi}{\partial J_3}\frac{\partial^2 J_3}{\partial \xi_{ij}\partial \xi_{mn}}. \end{aligned} \tag{6.78}$$

The derivative of the flow direction with respect to the tensor $\boldsymbol{N}$ follows identical lines and is thus not presented in detail here.

6.5.2. Tangent operator

The return-mapping algorithm is completed by the so-called algorithmic tangent operator. That operator is required for an asymptotic quadratic convergence of the finite element framework. In the material setting, the tangent operator is defined as

$$\mathbb{C} = 2\,\frac{\mathrm{d}\boldsymbol{S}}{\mathrm{d}\boldsymbol{C}} = 2\Bigg[\underbrace{\left(\frac{\partial \boldsymbol{S}}{\partial \boldsymbol{C}^{\mathrm{e}}} : \frac{\partial \boldsymbol{C}^{\mathrm{e}}}{\partial \boldsymbol{F}^{\mathrm{p}}} + \frac{\partial \boldsymbol{S}}{\partial \boldsymbol{F}^{\mathrm{p}}}\right)}_{=:\frac{\mathrm{d}\boldsymbol{S}}{\mathrm{d}\boldsymbol{F}^{\mathrm{p}}}} : \frac{\mathrm{d}\boldsymbol{F}^{\mathrm{p}}}{\mathrm{d}\boldsymbol{C}} + \frac{\partial \boldsymbol{S}}{\partial \boldsymbol{C}^{\mathrm{e}}} : \frac{\partial \boldsymbol{C}^{\mathrm{e}}}{\partial \boldsymbol{C}}\Bigg]. \tag{6.79}$$

Here, $\boldsymbol{S}$ and $\boldsymbol{C}$ are the second Piola-Kirchhoff stress tensor and the right Cauchy-Green strain tensor. Considering $\boldsymbol{F}^{\mathrm{p}}$ as a function of $\boldsymbol{N}$ and $\Delta\lambda$ (see Eq. (6.62)), $\frac{\mathrm{d}\boldsymbol{F}^{\mathrm{p}}}{\mathrm{d}\boldsymbol{C}}$ is further expanded as

$$\frac{\mathrm{d}\boldsymbol{F}^{\mathrm{p}}}{\mathrm{d}\boldsymbol{C}} = \frac{\partial \boldsymbol{F}^{\mathrm{p}}}{\partial \boldsymbol{N}} : \frac{\mathrm{d}\boldsymbol{N}}{\mathrm{d}\boldsymbol{C}} + \frac{\partial \boldsymbol{F}^{\mathrm{p}}}{\partial \Delta\lambda} \otimes \frac{\mathrm{d}\Delta\lambda}{\mathrm{d}\boldsymbol{C}}. \tag{6.80}$$

Here, $\frac{\mathrm{d}\Delta\lambda}{\mathrm{d}\boldsymbol{C}}$ and $\frac{\mathrm{d}\boldsymbol{N}}{\mathrm{d}\boldsymbol{C}}$ are calculated by linearizing the nonlinear system (6.63, 6.64) with respect to $\boldsymbol{C}$ (the return-mapping algorithm), i.e.,

$$\frac{\mathrm{d}\boldsymbol{R}_1}{\mathrm{d}\boldsymbol{C}} = \frac{\partial \boldsymbol{R}_1}{\partial \boldsymbol{N}} : \frac{\mathrm{d}\boldsymbol{N}}{\mathrm{d}\boldsymbol{C}} + \frac{\partial \boldsymbol{R}_1}{\partial \Delta\lambda} \otimes \frac{\mathrm{d}\Delta\lambda}{\mathrm{d}\boldsymbol{C}} + \frac{\partial \boldsymbol{R}_1}{\partial \boldsymbol{C}}, \tag{6.81}$$

$$\frac{\mathrm{d}R_2}{\mathrm{d}\boldsymbol{C}} = \frac{\partial R_2}{\partial \boldsymbol{N}} : \frac{\mathrm{d}\boldsymbol{N}}{\mathrm{d}\boldsymbol{C}} + \frac{\partial R_2}{\partial \Delta\lambda}\frac{\mathrm{d}\Delta\lambda}{\mathrm{d}\boldsymbol{C}} + \frac{\partial R_2}{\partial \boldsymbol{C}}. \tag{6.82}$$

For a converged return-mapping step ($|\boldsymbol{R}_1| \to 0$ and $|R_2| \to 0$), implying $\frac{\mathrm{d}\boldsymbol{R}_1}{\mathrm{d}\boldsymbol{C}} = \boldsymbol{0}$ and $\frac{\mathrm{d}R_2}{\mathrm{d}\boldsymbol{C}} = \boldsymbol{0}$, $\frac{\mathrm{d}\Delta\lambda}{\mathrm{d}\boldsymbol{C}}$ and $\frac{\mathrm{d}\boldsymbol{N}}{\mathrm{d}\boldsymbol{C}}$ are obtained as

$$\frac{\mathrm{d}\Delta\lambda}{\mathrm{d}\boldsymbol{C}} = -\frac{\frac{\partial R_2}{\partial \boldsymbol{C}} - \frac{\partial R_2}{\partial \boldsymbol{N}} : \left(\frac{\partial \boldsymbol{R}_1}{\partial \boldsymbol{N}}\right)^{-1} : \frac{\partial \boldsymbol{R}_1}{\partial \boldsymbol{C}}}{\frac{\partial R_2}{\partial \Delta\lambda} - \frac{\partial R_2}{\partial \boldsymbol{N}} : \left(\frac{\partial \boldsymbol{R}_1}{\partial \boldsymbol{N}}\right)^{-1} : \frac{\partial \boldsymbol{R}_1}{\partial \Delta\lambda}}, \tag{6.83}$$

and

$$\frac{\mathrm{d}\boldsymbol{N}}{\mathrm{d}\boldsymbol{C}} = -\left(\frac{\partial \boldsymbol{R}_1}{\partial \boldsymbol{N}}\right)^{-1} : \left(\frac{\partial \boldsymbol{R}_1}{\partial \Delta\lambda} \otimes \frac{\mathrm{d}\Delta\lambda}{\mathrm{d}\boldsymbol{C}} + \frac{\partial \boldsymbol{R}_1}{\partial \boldsymbol{C}}\right). \tag{6.84}$$

The remaining derivatives necessary for the algorithmic tangent (6.79) are

$$\frac{\partial C^{\mathrm{e}}_{ij}}{\partial C_{kl}} = {F^{\mathrm{p}}}^{-1}_{ik}\,{F^{\mathrm{p}}}^{-T}_{lj}, \tag{6.85}$$

$$
\begin{aligned}
\frac{\partial S_{ij}}{\partial C^{\mathrm{e}}_{mn}} &= \left(\Lambda \frac{\det \boldsymbol{C}^{\mathrm{e}} - 1}{2} - \mu\right) F^{\mathrm{p}^{-1}}_{ia} \, F^{\mathrm{p}^{-1}}_{jb} \, \frac{\partial C^{\mathrm{e}^{-1}}_{ab}}{\partial C^{\mathrm{e}}_{mn}} \\
&\quad + \frac{\Lambda}{2} \frac{\partial \det \boldsymbol{C}^{\mathrm{e}}}{\partial C^{\mathrm{e}}_{mn}} F^{\mathrm{p}^{-1}}_{ia} \, C^{\mathrm{e}^{-1}}_{ab} \, F^{\mathrm{p}^{-1}}_{jb} \,,
\end{aligned}
\tag{6.86}
$$

$$
\begin{aligned}
\frac{\partial S_{ij}}{\partial F^{\mathrm{p}}_{mn}} &= \left(\Lambda \frac{\det \boldsymbol{C}^{\mathrm{e}} - 1}{2} - \mu\right) C^{\mathrm{e}^{-1}}_{ab} \left(\frac{\partial F^{\mathrm{p}^{-1}}_{ia}}{\partial F^{\mathrm{p}}_{mn}} F^{\mathrm{p}^{-1}}_{jb} + F^{\mathrm{p}^{-1}}_{ia} \frac{\partial F^{\mathrm{p}^{-1}}_{jb}}{\partial F^{\mathrm{p}}_{mn}} \right) \\
&\quad + \mu \left(\frac{\partial F^{\mathrm{p}^{-1}}_{ib}}{\partial F^{\mathrm{p}}_{mn}} F^{\mathrm{p}^{-1}}_{jb} + F^{\mathrm{p}^{-1}}_{ib} \frac{\partial F^{\mathrm{p}^{-1}}_{jb}}{\partial F^{\mathrm{p}}_{mn}} \right),
\end{aligned}
\tag{6.87}
$$

$$
\frac{\partial C^{\mathrm{e}}_{ij}}{\partial F^{\mathrm{p}}_{kl}} = F_{ca} \, F_{cb} \left(\frac{\partial F^{\mathrm{p}^{-1}}_{ai}}{\partial F^{\mathrm{p}}_{kl}} F^{\mathrm{p}^{-1}}_{bj} + F^{\mathrm{p}^{-1}}_{ai} \frac{\partial F^{\mathrm{p}^{-1}}_{bj}}{\partial F^{\mathrm{p}}_{kl}} \right). \tag{6.88}
$$

The elaborated return-mapping scheme has been implemented as user material subroutine (UMAT) in ABAQUS® via FORTRAN.

Remark 12 *It should be mentioned that the tangent moduli required by the ABAQUS® solver is given by the push-forward of the material description of the tangent operator* $\mathbb{C}$ *with respect to* $\boldsymbol{F}$*, cf. Nebebe (2011).*

6.5.3. The algorithm for model parameters identification

In contrast to the classical strain-driven return-mapping scheme described in the previous sections, a slightly modified stress-driven algorithm is employed for the calibration of the material parameters. It is sketched in Fig. 6.5. It bears emphasis that this algorithm does not dependent explicitly on the elastic material model, since the respective mechanical response is already included in the prescribed stresses. Based on the Karush-Kuhn-Tucker conditions and the flow rule, the updated plastic deformation gradient and the internal variables are computed for a certain loading step. Subsequently, the yield surface of that state is computed by scanning the stress space in 128 steps.

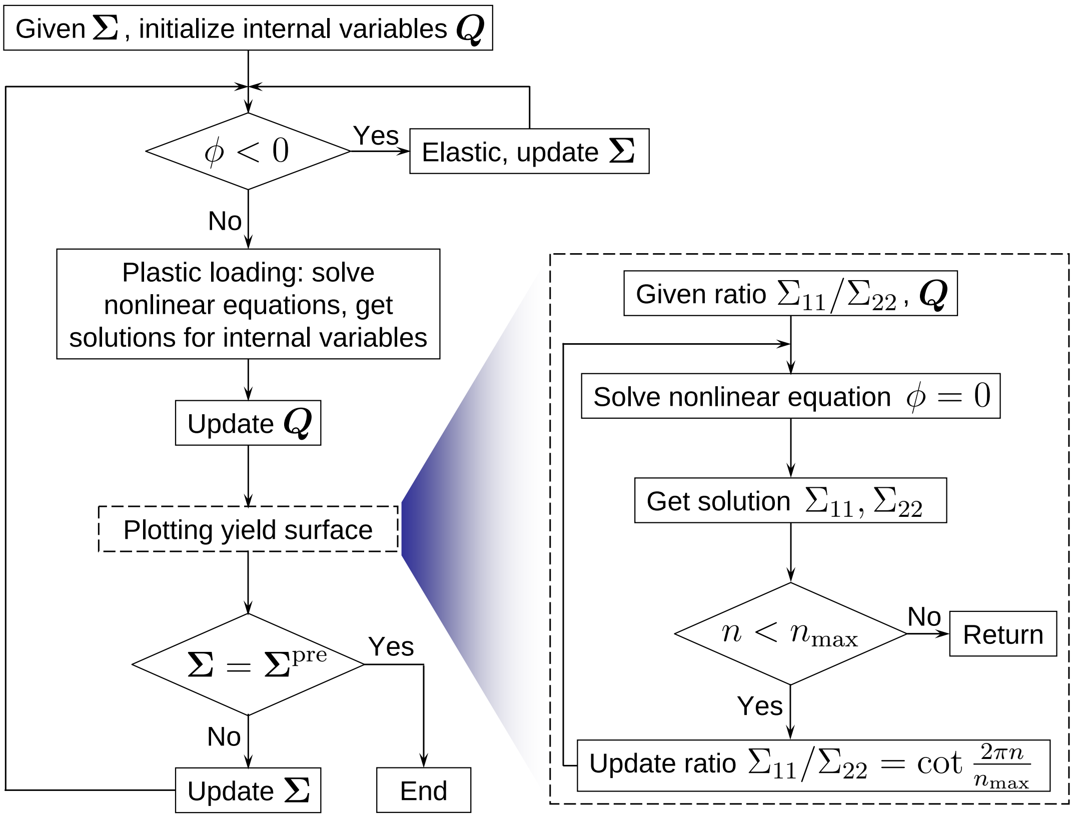
Given $\boldsymbol{\Sigma}$, initialize internal variables $\boldsymbol{Q}$
$\phi < 0$
Yes
Elastic, update $\boldsymbol{\Sigma}$
No
Plastic loading: solve nonlinear equations, get solutions for internal variables
Update $\boldsymbol{Q}$
Plotting yield surface
$\boldsymbol{\Sigma} = \boldsymbol{\Sigma}^{\text{pre}}$
Yes
No
Update $\boldsymbol{\Sigma}$
End
Given ratio Σ_{11}/Σ_{22}, $\boldsymbol{Q}$
Solve nonlinear equation $\phi = 0$
Get solution Σ_{11}, Σ_{22}
$n < n_{\max}$
No
Return
Yes
Update ratio $\Sigma_{11}/\Sigma_{22} = \cot \frac{2\pi n}{n_{\max}}$

Figure 6.5.: Algorithm for the computation of the yield surface in the $\Sigma_{11}-\Sigma_{22}$ space. $n_{\max}$ is the number of points on a single yield surface, $\boldsymbol{\Sigma}^{\text{pre}}$ is the prescribed (upper) limit of the Mandel stress during plotting

7. Numerical example

A numerical application of the constitutive model proposed in Section 6.1 and implemented as user material subroutine in ABAQUS, see Section 6.5, is discussed in the current chapter. This shall demonstrate the predictive capabilities of the model and is used as a verification test. The model parameters employed in the following are those which have been calibrated for AZ31 (cf. Section 6.2 and Tab. A.2). A circumferentially notched round bar loaded under uni-axial tension is considered.

7.1. Notched bar

The novel constitutive model implemented in UMAT/ABAQUS standard is applied to simulate the deformation of a 3D notched bar under uniaxial tension. The FE model consists of one eighth of the solid exploiting symmetry conditions. The dimensions are given in Fig. 7.1 (left). The geometry is discretized by fully integrated 8-noded 3D brick finite elements, see Fig. 7.1 (middle). A uniform displacement is prescribed at the upper cross section of the specimen. Loading is applied in the material's RD direction. The axial reaction force as well as the change of diameter at the notch in two perpendicular directions, namely in RD and TD directions, are recorded. For the sake of comparison, the computation is also performed by means of the classical von Mises model without distortional hardening.

The accumulated equivalent plastic strain for a top displacement of a magnitude 2.5 mm is depicted in Fig. 7.2. Accordingly, strain localization at the notch root is observed (necking). In order to study the global behaviour of the specimen, the reaction force is evaluated as a function of the reduction of the diameter (Δd, shown in Fig. 7.2). For anisotropic materials, the reduction of the diameter may not be uniform and thus, the initially circular cross section becomes an ellipsoid. This effect can be identified by the branching of the force-Δd signal, see Fig. 7.2. In the simulation based on von Mises plasticity, this effect is not included (with $\mathbb{H}_i$ simplified to the isotropic case, distortional hardening was turned off by setting $b_{\mathrm{dis}i} = 0$).

The correctness of the implementation was checked by analyzing the conver-

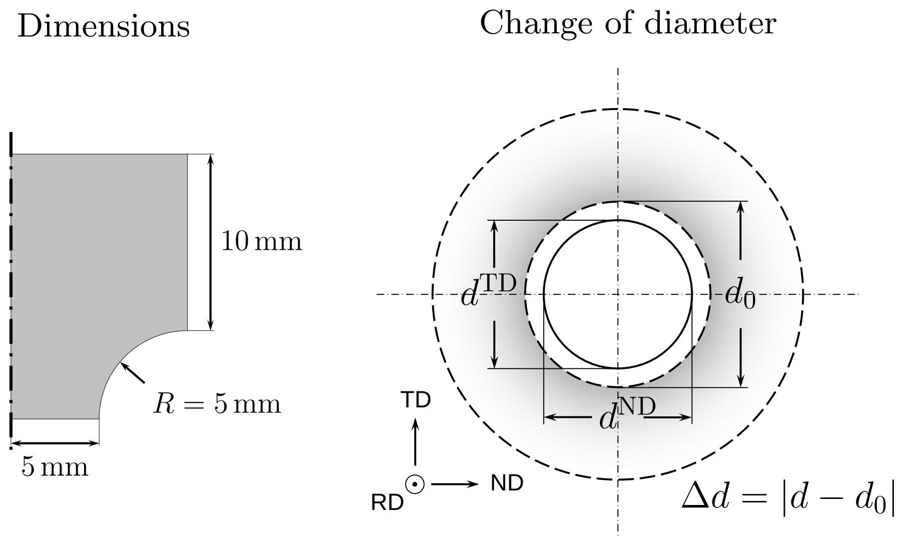
Dimensions
Change of diameter
Mesh
10 mm
$R = 5\,\mathrm{mm}$
5 mm
d^{TD}
d_0
d^{ND}
TD
RD
ND
$\Delta d = |d - d_0|$

Figure 7.1.: Notched round bar under uniaxial tension: geometry and finite element mesh

gence rate. According to Tab. 7.1, the convergence is asymptotically quadratic, as expected from the Newton scheme.

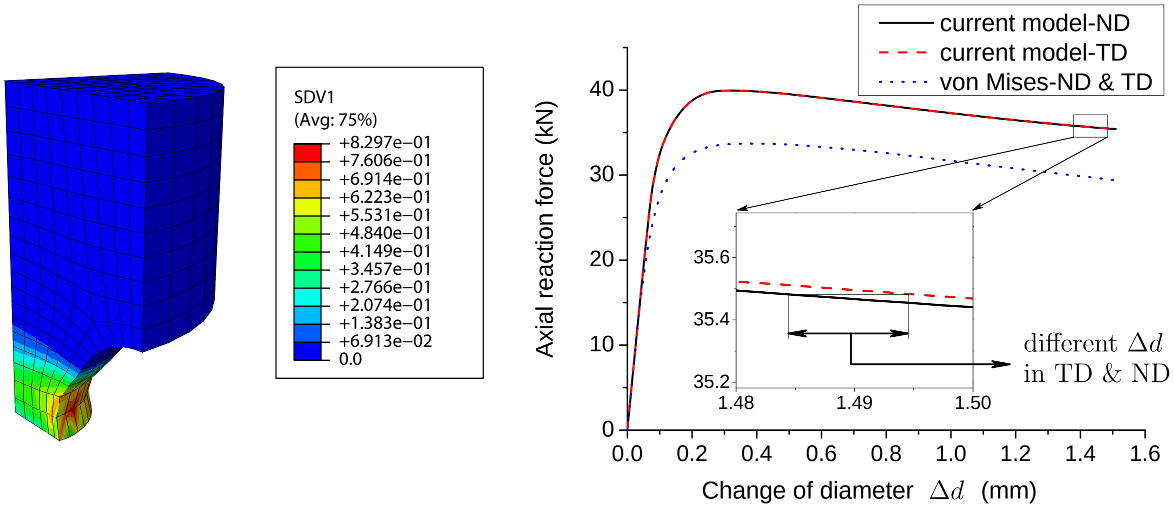

Figure 7.2.: Notched round bar under uniaxial tension (only the vertical displacements are prescribed at the upper surface): contour of equivalent plastic strain for a top displacement of 2.5mm and load-displacement diagram

Convergence of the return-mapping scheme: Convergence of the finite element residual for a plastic deformation

Iteration	1	2	3
Residual	$1.78{\cdot}10^{-1}$	$-7.61{\cdot}10^{-2}$	$1.05{\cdot}10^{-5}$

Table 7.1.: Convergence of the FEM model

8. Conclusions and outlook

In the present thesis, different macroscopic phenomenological constitutive models suitable for describing the distortion of the yield function due to texture evolution in polycrystals have been presented. Focus was on the mechanical response of magnesium alloys. Among the existing models, one proposed by Teodosiu and co-workers, one advocated by Levkovitch & Svendsen and one introduced by Feigenbaum & Dafalias were analyzed in detail. It was found that cross hardening and the distortion of the yield function is captured in all the models by an evolving fourth-order tensor governed by a differential equation similar to the one of by now classical Armstrong-Frederick rule. Within the Teodosiu and the Levkovitch & Svendsen models, this evolution equation is decomposed into a part related to currently active slip systems and an additional part that corresponding to latent slip systems. Furthermore, Teodosiu and co-workers focused on the effects of work hardening stagnation, softening and resumption and do not account for a distortion of the yield surface. For a better comparison, all models were reformulated and implemented into the modern frame of hyperelastoplasticity, and a yield function in terms of the Mandel stress was chosen in order to guarantee thermodynamical consistency of the elastic processes at finite strain and material frame indifference. Since the original models do not account for the strength differential effect as observed in magnesium alloys, respective extensions were discussed and subsequently implemented. For these extended models, it was shown that only the extended Feigenbaum & Dafalias model can fulfill the Second Law of thermodynamics by enforcing an additional non-linear inequality. However, that model predicts a high curvature of the yield function in the loading direction, while the opposite region of the yield function is rather flat. Since such a response is not observed for most magnesium alloys, a novel constitutive model was introduced. The crucial idea was to model distortional hardening similarly to kinematic hardening by an Armstrong-Frederick-type equation obtained from a convex plastic potential, i.e., to apply the framework of generalized standard materials. This procedure automatically guaranteed thermodynamical consistency of the resulting model, independent of the chosen material parameters and for arbitrary loading paths. The predictive capabilities of the final model were eventually demonstrated by comparisons to experimentally measured data. With calibrated material parameters, the final model was implemented in UMAT/ABAQUS standard via a semi-implicit integration algorithm. Numerical examples demonstrated the predictive capabilities of the resulting model.

Although the novel model proposed within the present thesis was both thermodynamically and variationally sound, several further improvements of the constitutive laws are still needed. Firstly, further experiments are required for a more accurate calibration of the material parameters, particularly experiments showing non-radial and non-proportional loading paths. Secondly, the relationship between the variables defined at the macroscale and the underlying processes at the microstructure has to be further strengthened. That is of utmost importance for understanding processing-material-properties relationships.

A. MODEL PARAMETERS CALIBRATED FOR AZ31

$$\mathcal{H}_1 = \begin{pmatrix} 6.70 & -8.58 & 1.87 & 0 & 0 & 0 \\ -8.58 & 3.19 & 5.38 & 0 & 0 & 0 \\ 1.87 & 5.38 & -7.26 & 0 & 0 & 0 \\ 0 & 0 & 0 & -14.05 & 0 & 0 \\ 0 & 0 & 0 & 0 & 1 & 0 \\ 0 & 0 & 0 & 0 & 0 & 1 \end{pmatrix} \tag{A.1}$$

$$\mathcal{H}_2 = \begin{pmatrix} -5.77 & -0.78 & 6.56 & 0 & 0 & 0 \\ -0.78 & 2.49 & -1.71 & 0 & 0 & 0 \\ 6.56 & -1.71 & -4.85 & 0 & 0 & 0 \\ 0 & 0 & 0 & -3.02 & 0 & 0 \\ 0 & 0 & 0 & 0 & 1 & 0 \\ 0 & 0 & 0 & 0 & 0 & 1 \end{pmatrix} \tag{A.2}$$

Table A.1.: Initial anisotropy of the yield surface - Matrix representations $\mathcal{H}_i$ of the tensors $\mathbb{H}_i$, compare to Mekonen et al. (2012), cf. Subsection 5.3.2, Section 6.2, Figs. 5.11, 6.1. Since the Mandel stress is symmetric (isotropic elastic response), $\mathbb{H}_i$ can be represented by 6×6 matrices.

The extended Teodosiu model - Subsection 4.1.2

Q_0 (MPa)	c_{iso}	Q_{iso}^{∞} (MPa)	c_{kin}
124.78	107416.15	95.55	-6528.50

$Q_{\text{kin}}^{(0)}$ (MPa)	$\hat{A}$	$\hat{B}$	f (MPa)
1546.72	$1.41 \cdot 10^{-2}$	$-1.17 \cdot 10^{-2}$	0.57

The extended Levkovitch & Svendsen model - Subsection 4.2.2

Q_{iso}^{∞} (MPa)	c_{iso}	Q_{kin}^{∞} (MPa)	c_{kin}
96.09	155764.85	1019.76	101.20

s_{D1}	c_{D1}	s_{L1}	c_{L1}	s_{D2}	c_{D2}	s_{L2}	c_{L2}
948.10	-0.014	1029.27	-0.0033	1746.09	0.99	987.01	1.10

The extended Feigenbaum & Dafalias model - Subsection 4.3.2

Q_0 (MPa)	κ_1	κ_2 (MPa^{-1})	a_1	a_2 (MPa^{-1})
115.47	$2.975 \cdot 10^{8}$	$9.37 \cdot 10^{-4}$	102437.7	0.0015

A_{11} (MPa^{-4})	A_{21} (MPa^{2})	A_{12} (MPa^{-4})	A_{22} (MPa^{2})
0.826	2029.1	-0.00003	1995.3

New constitutive model - Chapter 6

Q_0 (MPa)	Q_{iso}^{∞} (MPa)	c_{iso}	b_{kin}	c_{kin} (MPa)
611.90	798.16	288.05	171.53	521.89

b_{dis1}	c_{dis1} (MPa^{-1})	b_{dis2}	c_{dis2} (MPa^{-1})
0.001869	0.774	0.003482	2.094

Table A.2.: Model parameters for the magnesium alloy AZ31. The elasticity constants are $E = 45000$ (MPa) and $\nu = 0.35$.

Bibliography

Agnew, S. & Duygulu, O. (2005): *Plastic anisotropy and the role of non-basal slip in magnesium alloy AZ31B*, in: International Journal of Plasticity, Volume 21, 6, 1161–1193.

Avedesian, M. & Baker, H. (1999): *Magnesium and magnesium alloys*, ASM speciality handbook, Materials Park, OH: ASM International 1999.

Baltov, A. & Sawczuk, A. (1965): *A rule of anisotropic hardening*, in: Acta Mechanica, Volume 1, 81–92.

Banabic, D., Kuwabara, T., Balan, T. & Comsa, D. (2004): *An anisotropic yield criterion for sheet metals*, in: Journal of Materials Processing Technology, Volume 157-158, 0, 462 – 465.

Barlat, F., Aretz, H., Yoon, J., Karabin, M., Brem, J. & Dick, R. (2005): *Linear transformation-based anisotropic yield functions*, in: International Journal of Plasticity, Volume 21, 1009–1039.

Barlat, F., Yoon, J. & Cazacu, O. (2007): *On linear transformations of stress tensors for the description of plastic anisotropy*, in: International Journal of Plasticity, Volume 23, 876–896.

Barthel, C., Levkovitch, V. & Svendsen, B. (2008): *Modeling of sheet metal forming processes taking into account distortional hardening*, in: International Journal of Material Forming, Volume 1, 105–108.

Boers, S., Schreurs, P., Geers, M., Levkovitch, V., Wang, J. & Svendsen, B. (2010): *Experimental characterization and model indentification of directional hardening effects in metals for complex strain path changes*, in: International Journal of Solids and Structures, Volume 47, 1361–1374.

Bruhns, O., Xiao, H. & Meyers, A. (1999): *Self-consistent Eulerian rate type elasto-plasticity models based upon the logarithmic stress rate*, in: International Journal of Plasticity, Volume 15, 5, 479 – 520.

Bui, H. (1966): *Ecrouissage des métaux*, in: Comptes Rendus de l Académie des Sciences, Volume AB262, A401–A404.

Carstensen, C., Hackl, K. & Mielke, A. (2002): *Non-convex potentials and microstructures in finite-strain plasticity*, in: Proceedings of the Royal Society, Series A, Volume 458, 299–317.

Cazacu, O. & Barlat, F. (2001): *Generalization of Drucker's yield criterion to orthotropy*, in: Mathematics and Mechanics of Solids, Volume 6, 6, 613–630.

Cazacu, O. & Barlat, F. (2004): *A criterion for description of anisotropy and yield differential effects in pressure-insensitive metals*, in: International Journal of Plasticity, Volume 20, 2027–2045.

Cazacu, O., Plunkett, B. & Barlat, F. (2006): *Orthotropic yield criterion for hexagonal closed packed metals*, in: International Journal of Plasticity, Volume 22, 1171–1194.

Christian, J. & Mahajan, S. (1995): *Deformation twinning*, in: Progress in Materials Science, Volume 39, 1-2, 1–157.

Coleman, B. & Gurtin, M. (1967): *Thermodynamics with internal state variables*, in: Journal of Chemical Physics, Volume 47, 597–613.

D.E. Helling, A. K. Miller, M. G. S. (1986): *An experimental investigation of the yield loci of 1100-0 aluminum, 70:30 brass, and an overaged 2024 aluminum alloy after various prestrains*, in: Journal of Engineering Materials and Technology, Volume 108, 313–320.

Drucker, D. C. (1949): *Relations of experiments to mathematical theories of plasticity*, in: Journal of Applied Mechanics, Volume 16, 349–357.

Feigenbaum, H. (2008): *Directional distortional hardening in plasticity based on thermodynamics* 2008, Dissertation, University of California Davis.

Feigenbaum, H. & Dafalias, Y. (2007): *Directional distortional hardening in metal plasticity within thermodynamics*, in: International Journal of Solids and Structures, Volume 44, 7526–7542.

Feigenbaum, H. & Dafalias, Y. (2008): *Simple model for directional distortional hardening in metal plasticity within thermodynamics*, in: Journal of Engineering Mechanics, Volume 134, 9, 730–738.

Graff, S., Brocks, W. & Steglich, D. (2007): *Yielding of magnesium: From single crystal to polycrystalline aggregates*, in: International Journal of Plasticity, Volume 23, 12, 1957–1978.

HADDADI, H., BOUVIER, S., BANU, M., MAIER, C. & TEODOSIU, C. (2006): *Towards an accurate description of the anisotropic behaviour of sheet metals under large plastic deformations: Modelling, numerical analysis and indentification*, in: International Journal of Plasticity, Volume 22, 2226–2271.

HAN-CHIN & WU (2003): *Effect of loading-path on the evolution of yield surface for anisotropic metals subjected to large pre-strain*, in: International Journal of Plasticity, Volume 19, 10, 1773 – 1800.

HECKER, S. S. (1973): *Influence of deformation history on the yield locus and stress-strain behaviour of aluminum and copper*, in: Metallurgical and Materials Transactions, Volume 4, 985–989.

HILL, R. (Ed.) (1973): *Inhomogeneity of Plastic Deformation*, ASM, Metals Park 1973.

HIWATASHI, S., BAEL, A., HOUTTE, P. & TEODOSIU, C. (1998): *Prediction of forming limit strains under strain-path changes: application of an anisotropic model based on texture and dislocation structure*, in: International Journal of Plasticity, Volume 14, 7, 647–669.

HOLZAPFEL, G. (2000): *Nonlinear Solid Mechanics A Continuum Approach for Engineering*, John Wiley & Sons Ltd 2000.

HOMAYONIFAR, M. & MOSLER, J. (2012): *Efficient modeling of microstructure evolution in magnesium by energy minimization*, in: International Journal of Plasticity, Volume 28, 1–20.

JOHANSSON, G., EKH, M. & RUNESSON, K. (2005): *Computational modeling of inelastic large ratcheting strains*, in: International Journal of Plasticity, Volume 21, 5, 955 – 980.

KELLEY, E. & HOSFORD, W. (1968a): *Plane-strain compression of magnesium and magnesium alloy crystals*, in: Transactions of the Metallurgical Society of the American Institute of Mechanical Engineers, Volume 242, 5–13.

KELLEY, E. & HOSFORD, W. (1968b): *The deformation characteristics of textured magnesium*, in: Transactions of the Metallurgical Society of the American Institute of Mechanical Engineers, Volume 242, 654–661.

KURTYKA, T. & ZYCZKOWSKI, M. (1996): *Evolution equations for distortional plastic hardening*, in: International Journal of Plasticity, Volume 12, 191–213.

KUWABARA, T., IKEDA, S. & KURODA, K. (1998): *Measurement and analysis of differential work hardening in cold-rolled steel sheet under biaxial tension*, in: Journal of Materials Processing Technology, Volume 80-81, 0, 517–523.

Kuwabara, T., Yoshida, K., Narihara, K. & Takahashi, S. (2005): *Anisotropic plastic deformation of extruded aluminum alloy tube under axial forces and internal pressure*, in: International Journal of Plasticity, Volume 21, 1, 101 – 117.

Lebensohn, R., Liu, Y. & Castaneda, P. P. (2004): *On the accuracy of the self-consistent approximation for polycrystals: comparison with full-field numerical simulations*, in: Acta Materialia, Volume 52, 18, 5347 – 5361.

Lee, E. (1969): *Elastic-plastic deformation at finite strains*, in: Journal of Applied Mechanics, Volume 36, 1–6.

Lee, M., Kim, S., Wagoner, R., Chung, K. & Kim, H. (2009): *Constitutive modeling for anisotropic/asymmetric hardening behaviour of magnesium alloy sheets: Application to sheet springback*, in: International Journal of Plasticity, Volume 25, 1, 70–104.

Lee, M., Wagoner, R., Lee, J., Chung, K. & Kim, H. (2008): *Constitutive modeling for anisotropic/asymmetric hardening behaviour of magnesium alloy sheets*, in: International Journal of Plasticity, Volume 24, 4, 545–582.

Lemaitre, J. (1985): *A continuous damage mechanics model for ductile fracture*, in: J. Eng. Mat. Techn., Volume 107, 83–89.

Lemaitre, J. & Chaboche, J. (1990): *Mechanics of solid materials*, Cambridge University Press 1990.

Li, M., Lou, X., Kim, J. & Wagoner, R. (2010): *An efficient constitutive model for room-temperature, low-rate plasticity of annealed Mg AZ31B sheet*, in: International Journal of Plasticity, Volume 26, 820–858.

Li, S., Hoferlin, E., Bael, A., Houtte, P. & Teodosiu, C. (2003): *Finite element modeling of plastic anisotropy induced by texture and strain-path change*, in: International Journal of Plasticity, Volume 19, 647–674.

Lou, X., Li, M., Boger, R., Agnew, S. & Wagoner, R. (2007): *Hardening evolution of AZ31B Mg sheet*, in: International Journal of Plasticity, Volume 23, 1, 44–86.

M. Boucher, P. Cayla, J. P. C. (1995): *Experimental studies of yield surfaces of aluminium alloy and low carbon steel under complex biaxial loadings*, in: European Journal of Mechanics - A/Solids, Volume 14, 1, 1–17.

Mandel, J. (1971): *Plasticite classique et viscoplasticitite*, CISM 1971.

Marin, J. & Sauer, J. A. (1953): *Plastic stress-strain relations under radial and non-radial combined stress loading*, in: Journal of the Franklin Institute, Volume 256, 2, 119 – 128.

Mekonen, M. N., Steglich, D., Bohlen, J., Letzig, D. & Mosler, J. (2012): *Mechanical characterization and constitutive modeling of Mg alloy sheets*, in: Materials Science and Engineering: A, Volume 540, 174–186.

Miehe, C. & Rosato, D. (2007): *Fast texture updates in fcc polycrystal plasticity based on a linear active-set-estimate of the lattice spin*, in: Journal of the Mechanics and Physics of Solids, Volume 55, 12, 2687 – 2716.

Miehe, C., Schotte, J. & Lambrecht, M. (2002): *Homogenization of inelastic solid materials at finite strains based on incremental minimization principles. Application to the texture analysis of polycrystals*, in: Journal of the Mechanics and Physics of Solids, Volume 50, 10, 2123 – 2167.

Mosler, J. (2007): *On the numerical modeling of localized material failure at finite strains by means of variational mesh adaption and cohesive elements*, Institut für Mechanik, Ruhr Universität Bochum 2007.

Mosler, J. (2010): *Variationally consistent modeling of finite strain plasticity theory with non-linear kinematic hardening*, in: Computer Methods in Applied Mechanics and Engineering, Volume 199, 2753–2764.

Mosler, J. & Bruhns, O. (2009): *Towards variational constitutive updates for non-associative plasticity models at finite strain: Models based on a volumetric-deviatoric split*, in: International Journal of Solids and Structures, Volume 46, 1676–1684.

Mosler, J. & Bruhns, O. (2010): *On the implementation of rate-independent standard dissipative solids at finite strain – Variational constitutive updates*, in: Computer Methods in Applied Mechanics and Engineering, Volume 199, 417–429.

Nebebe, M. (2011): *Experimental and Numerical Investigation of Mg Alloy Sheet Forming* 2011, Dissertation, Christian-Albrechts-Universität zu Kiel.

Noman, M., Clausmeyer, T., Barthel, C., Svendsen, B., Huetink, J. & Riel, M. (2010): *Experimental characterization and modeling of the hardening behaviour of the sheet steel LH800*, in: Materials Science and Engineering A, Volume 527, 2515–2526.

Ogden, R. (1997): *Non-Linear Elastic Deformations*, Dover Publications 1997.

Ortiz, M. & Stainier, L. (1999): *The variational formulation of viscoplastic constitutive updates*, in: Computer Methods in Applied Mechanics and Engineering, Volume 171, 419–444.

PEETERS, B., KALIDINDI, S., TEODOSIU, C., HOUTTE, P. & AERNOUDT, E. (2002): *A theoretical investigation of the influence of dislocation sheets on evolution of yield surfaces in single-phase B.C.C. polycrystals*, in: Journal of the Mechanics and Physics of Solids, Volume 50, 783–807.

PHILLIPS, A. & JUH-LING, T. (1972): *The effect of loading path on the yield surface at elevated temperatures*, in: International Journal of Solids and Structures, Volume 8, 4, 463 – 474.

PIETRYGA, M. P., VLADIMIROV, I. N. & REESE, S. (2012): *A finite deformation model for evolving flow anisotropy with distortional hardening including experimental validation*, in: Mechanics of Materials, Volume 44, 0, 163 – 173.

PLESEK, J., FEIGENBAUM, H. & DAFALIAS, Y. (2010): *Convexity of yield surface with directional distortional hardening rules*, in: Journal of Engineering Mechanics, Volume 136, 4.

PLUNKETT, B., LEBENSOHN, R., CAZACU, O. & BARLAT, F. (2006): *Anisotropic yield function of hexagonal materials taking into account texture development and anisotropic hardening*, in: Acta Materialia, Volume 54, 4159–4169.

PROUST, G., TOME, C., JAIN, A. & AGNEW, S. (2009): *Modeling the effect of twinning and detwinning during strain-path changes of magnesium alloy AZ31*, in: International Journal of Plasticity, Volume 25, 5, 861–880.

REES, D. W. A. (1987): *Applications of classical plasticity theory to non-radial loading paths*, in: Proceedings of the Royal Society A, Volume 410, 443–475.

ROBERTS, C. (1960): *The deformation of Magnesium, in Magnesium and Its Alloys*, John Wiley & Sons Ltd 1960.

ROCKAFELLAR, R. T. (1970): *Convex Analysis*, Princeton University Press 1970.

ROTERS, F., EISENLOHR, P., HANTCHERLI, L., TJAHJANTO, D. D. & BIELER, T. R. R. D. (2010): *Overview of constitutive laws, kinematics, homogenization and multiscale methods in crystal plasticity finite-element modeling: Theory, experiments, applications*, in: Acta Materiala, Volume 58, 1152–1211.

SCILAB DOCUMENTATION (2011): *Scilab: The free software for numerical computation*, Digiteo, Paris, France, URL `http://www.scilab.org`.

Shi, B. & Mosler, J. (2012): *On the macroscopic description of yield surface evolution by means of distortional hardening models: Application to magnesium*, in: International Journal of Plasticity, Accepted.

Simo, J. & Hughes, T. (1998): *Computational Inelasticity*, Volume 7 of *Interdisciplinary Applied Mathematics*, Springer-Verlag New York, Inc 1998.

Simo, J. C. (1998): *Numerical analysis of classical plasticity*, Volume IV of *Handbook for numerical analysis*, Elsevier Amsterdam 1998.

Steglich, D., Brocks, W., Bohlen, J. & Barlat, F. (2011): *Modelling direction-dependent hardening in magnesium sheet forming simulations*, in: International Journal of Material Forming, Volume 4, 2, 243–253.

Vladimirov, I. N., Pietryga, M. P. & Reese, S. (2010): *Anisotropic finite elastoplasticity with nonlinear kinematic and isotropic hardening and application to sheet metal forming*, in: International Journal of Plasticity, Volume 26, 5, 659 – 687.

Wang, J., Hoagland, R., Hirth, J., Capolungo, L., Beyerlein, I. & Tome, C. (2009): *Nucleation of a* $\bar{1}012$ *twin in hexagonal close-packed crystals*, in: Scripta Materialia, Volume 61, 9, 903–906.

Wang, J., Levkovitch, V., Reusch, F., Svendsen, B., Huetink, J. & Riel, M. (2008): *On the modeling of hardening in metals during non-proportional loading*, in: International Journal of Plasticity, Volume 24, 1039–1070.

Wang, J., Levkovitch, V. & Svendsen, B. (2006): *Modeling and simulation of directional hardening in metals during non-proportional loading*, in: Journal of Materials Processing Technology, Volume 177, 430–432.

Xiao, H., Bruhns, O. & Meyers, A. (2000): *A consistent finite elastoplasticity theory combining additive and multiplicative decomposition of the stretching and the deformation gradient*, in: International Journal of Plasticity, Volume 16, 2, 143 – 177.

Xu, Z. (1994): *The Determination of Shear StressStrain Curve Using Torsion Test and an Experimental Investigation of Aluminum Tested Under Torsion at Room and Elevated Temperatures in the Large Strain Range* 1994, Dissertation, University of Iowa.

Yoo, M. (1981): *Slip, twinning, and fracture in hexagonal close-packed metals*, in: Metallurgical and Materials Transactions A, Volume 12, 3, 409–418.